

1 Production and Interaction of X rays Radiation Measurement Quantities and Units

Roger H. Johnson

Biomedical Engineering, Marquette University

1.1	Introduction	3
1.2	Production of X rays	3
1.2.1	Bremsstrahlung and Characteristic Radiation	3
1.2.2	Electron-Impact X-ray Sources	8
1.2.2.1	Electrical Circuits for X-ray Tubes	8
1.2.2.2	Cathodes and Anodes	14
1.2.2.3	Sources for Diagnostic Radiology	18
1.2.2.4	X-ray Tube Ratings	20
1.2.2.5	X-ray Tube Spectra	22
1.2.2.6	Beam Filtration	29
1.2.2.7	Sources for Mammography	31
1.2.2.8	Specialized Sources for Research	33
1.2.3	Synchrotron X-ray Sources	35
1.2.3.1	Storage Rings	35
1.2.3.2	Insertion Devices	43
1.2.3.3	Applications of Synchrotron Sources	45
1.2.4	Plasma X-ray Sources	47
1.2.4.1	Gas Plasma Sources	49
1.2.4.2	Laser-produced Plasma Sources	49
1.2.4.3	Application of Plasma Sources	52
1.2.5	X-ray Lasers and Free Electron Lasers	56
1.3	Interaction of X rays with Matter	59
1.3.1	Indirect versus Direct Ionization	61
1.3.2	Scattering	62
1.3.2.1	Elastic Scattering	63
1.3.2.2	Inelastic Compton Scattering	66
1.3.3	Absorption	68
1.3.3.1	Photoelectric Absorption	68
1.3.3.2	Pair Production	70
1.3.3.3	Photodisintegration	70

1.3.4	Attenuation Cross Sections and the Linear Attenuation Coefficient	70
1.3.5	Interaction Of X rays with Detector Materials	74
1.3.6	Object, Subject and Image Contrast	75
1.4	Quantities and Units	77
1.4.1	Fundamental Constants, Quantities and Units	78
1.4.2	Particle Fluence and Flux	80
1.4.3	Energy Fluence and Flux	80
1.4.4	Exposure: the Roentgen	81
1.4.5	Absorbed Dose: The Gray the Rad and the Kerma	81
1.4.6	Dose Equivalent: Linear Energy Transfer, The Quality Factor, the Sievert and the Rem	82
1.5	References	83

1.1 Introduction

This chapter deals with the production of X rays and their mechanisms of interaction with materials. The emphasis is placed on X rays useful for diagnostic imaging, that is in the energy range between 10 and 140 keV. X-ray interactions are discussed primarily from the standpoint of imaging, as opposed to diffraction or spectroscopy. Brief coverage of important developments not yet clinically utilized, such as synchrotron and plasma X-ray sources, is also included. Because these sources produce radiation over a wide spectral range, including intense soft X rays useful for biological X-ray microscopy, microtomography and spectroscopy, production and interaction of low-energy X rays are discussed, though in considerably less depth. Though electron-impact sources are still used to produce most X rays used in clinical applications and for biomedical research, the unique properties of some of the newer devices, most notably laser-produced plasma and synchrotron X-ray sources, have made possible discoveries which never would have been made in their absence. As these sources become ever cheaper and more efficient, they are certain to have an important impact in basic research, and possibly in clinical practice as well.

1.2 Production of X rays

This section describes the physics involved in and a few of the devices used for the production of X rays. Most types of artificially-produced ionizing photon beams arise from one of two basic mechanisms: Bremsstrahlung generation or characteristic emission. A description of these mechanisms will be followed by sections on the three most important classes of devices used to produce X rays for biomedical imaging: electron-impact X-ray tubes, synchrotrons and laser-produced plasma X-ray sources. Less common and recently proposed X-ray sources like special-purpose microfocal tubes, z-pinch plasmas, and X-ray lasers will be discussed in less depth.

1.2.1 Bremsstrahlung and Characteristic Radiation

When high-energy electrons interact with matter, their kinetic energy is lost to heat and radiative processes. Though nearly all the incident electron energy is converted to heat, the radiative processes are significant enough to be the source of most X rays used for imaging. The necessary parts of an X-ray source of the type most commonly employed in the clinic are a cathode (source of electrons) and an anode, housed in an evacuated enclosure to facil-

itate the passage of electrons between them, and a high-voltage generator to supply the potential difference between the cathode and anode which imparts to the electrons their kinetic energy. X rays were in fact discovered when Roentgen observed evidence of Bremsstrahlung emission upon discharging high-voltage sparks in a low-pressure glass tube.

When energetic electrons, or other “swift” charged particles, interact with matter, there are four types of interaction which result eventually in the loss of all their kinetic energy¹:

- 1) Elastic collision with atomic electrons in the target. Significant only for very-low-energy electrons (< 100 eV), these interactions may be thought of as taking place with the target atom as a whole. The incident electron is deflected by the field of the atomic electrons, but the amount of energy transferred to the target atom is less than the lowest ionization potential.
- 2) Elastic collision with a target nucleus. This interaction, which has a relatively high probability of occurring, causes deflection of the incident electron, but is not accompanied by excitation of the target nucleus, nor by radiation, resulting only in the loss of a sufficient (small) amount of kinetic energy to conserve momentum between the interacting particles. The first two types of interaction do not produce energetic photons and will not be considered further.
- 3) Inelastic collision with bound atomic electrons in the target. Most of the incident electron kinetic energy is lost by this mechanism. Bound electrons may either be excited or ejected from the target atom (ionization). If the energy of a colliding incident electron exceeds their binding energy and inner-shell (K and L) electrons are ejected from target atoms, these vacancies are filled by downward cascades from outer orbitals as shown in Figure 1.1², an event accompanied by emission of characteristic photons which may contribute a significant though small fraction (10–25% for tungsten in the diagnostic energy range) of the flux available for imaging.
- 4) Inelastic collision with a target nucleus. If incident electrons pass close to a target nucleus but escape capture, they will be deflected in their path by the electric field of the nucleus and may lose energy either to nuclear excitation or, more commonly, to radiation as shown in Figure 1.2. It is this radiation, termed “Bremsstrahlung” (German for “braking radiation”), which constitutes the primary emission from clinical X-ray tubes. Although highly unlikely at low incident electron energies, and relatively rare at diagnostic energies, at extremely high energies (> 10 MeV) the likelihood of these inelastic nuclear collisions may surpass that of ionization. At all energies the ratio of these radiative to ionizational energy losses is greater for high Z than for low. In the diagnostic range, even for high- Z elements, it is less than 0.1. If an incident electron of kinetic energy T experiences a direct hit with a target atom nucleus, losing all its energy in a single interaction, a photon of energy $h\nu = T$ will be produced. Such photons are very rare, and possess the highest energy possible for electron-target interactions.

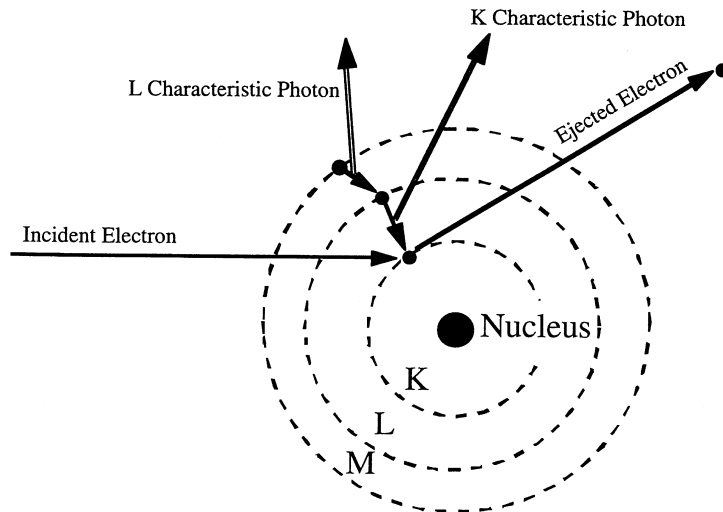


Figure 1.1. Fluorescent X-ray emission. An inner-shell electron is ejected and the downward cascade to fill the vacancy results in emission of photons of characteristic energies. (Adapted from Bushberg *et al.*, 1994².)

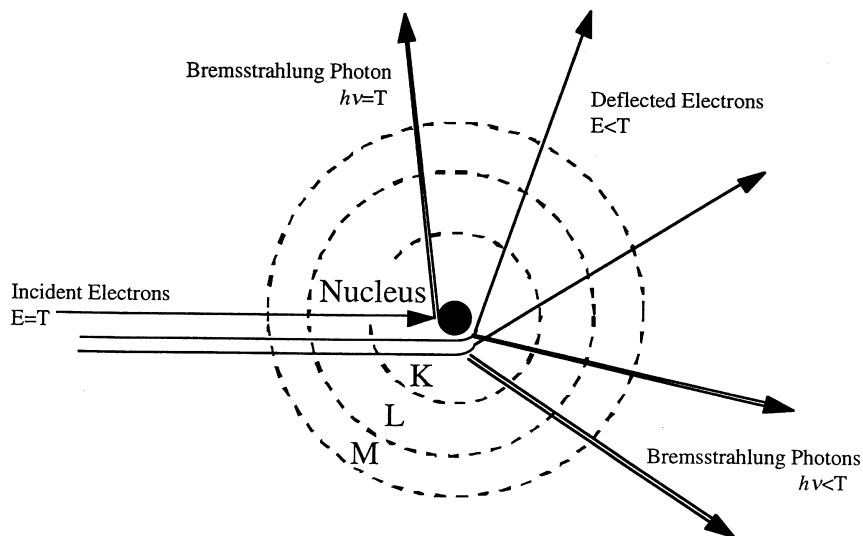


Figure 1.2. Bremsstrahlung emission. Incident electrons are accelerated in the nuclear field emitting energetic photons to conserve energy and momentum. (Adapted from Bushberg *et al.*, 1994².)

In a thick target, all of the kinetic energy of the incident electrons will eventually be lost by a combination of these four types of interaction. Each electron may undergo a large number of interactions before being stopped. After inelastic interactions involving atomic electrons, the ejected electrons may themselves have substantial kinetic energy. These δ rays are fast charged particles which will also be stopped by a combination of the four interactions above. A 100-keV electron may undergo 1000 such interactions before being stopped³.

From classical theory, if it is assumed that all target electrons are free electrons (justified in the case where the target electron's binding energy is negligible compared with the kinetic energy it receives), interaction with atomic electrons is reduced to the simple case of an elastic coulomb collision. For such collisions, the probability of transferring an energy Q to the target electron is inversely proportional to Q^2 , heavily favoring interactions resulting in small energy losses over large-loss interactions. In fact, about half the kinetic energy of incident electrons is lost in a large number of low-loss ionizational collisions and the other half to a much smaller number of higher-loss interactions in which δ rays or Bremsstrahlung are produced. Limitations of the classical theory for inelastic scattering of electrons by atomic electrons are detailed by Evans¹.

As derived by Evans from Bethe's original retardation law, for a non-relativistic electron of velocity V , rest mass $m_0 \approx 10^{-27}$ g, and kinetic energy $T = \frac{1}{2} m_0 V^2$ interacting with a target of atomic number Z , the energy loss per unit pathlength due to ionizational collisions is approximately given by¹:

$$\begin{aligned} \left(\frac{dT}{ds} \right)_{ion} &= 1.257 \times 10^{-6} \frac{e^4}{m_0 V^2} N Z \ln \frac{m_0 V^2}{I \sqrt{2}} \\ &= 6.280 \times 10^{-7} \frac{e^4}{T} N Z \ln \frac{T \sqrt{2}}{I} \text{ J/cm} \end{aligned} \quad (1.1)$$

where $e = 4.80 \times 10^{-10}$ esu is the charge on the electron, N is Avogadro's number (atoms/cm³) and I is the geometric mean of the ionization and excitation potentials of the target atom. I is a nebulous quantity, difficult to determine theoretically or experimentally, but it has been approximated by

$$I \approx kZ \quad (1.2)$$

where k is a constant decreasing from 18 eV for H to 10 eV for Pb¹. The inverse relationship between stopping power and electron energy is evident from Eq. (1.1). In the diagnostic energy range, while most of the radiation is produced by Bremsstrahlung, most of the incident electron energy is lost to ionizational collisions. A different form for the above equation for electron retardation by ionization and more complex relationships between I and Z are reviewed by Rao-Sahib and Wittry⁴, who also show that reasonable agreement with experiment is obtained when k is set to the popular value of 11.5 eV⁵.

For inelastic nuclear interactions, classical theory holds that radiation will be produced whenever charged particles are accelerated, and that the amplitude of the emitted electromagnetic radiation will be proportional to the acceleration undergone by the charge. The acceleration of a particle with charge ze and mass M by a nucleus of charge Ze is proportional to $\frac{Zze^2}{M}$.

Since intensity is proportional to the square of the product of the charge and the amplitude, the intensity of emitted radiation is proportional to $\frac{Z^2 z^4 e^6}{M^2}$. It

is seen that the Bremsstrahlung intensity varies as the square of the atomic number of the target, a prediction confirmed for thin (but not thick, see below) targets by experiment, and inversely as the square of the mass of the incident particle, explaining why electrons produce about one million times more Bremsstrahlung than protons or alpha particles of the same velocity.

Most of the quantum mechanical theory for Bremsstrahlung is posed in terms of, for example, loss of kinetic energy per unit pathlength of the incident radiation. Since it is practically impossible to know anything about pathlengths of electrons in solid targets, many experiments, which have been used to successfully validate quantum mechanical theoretical findings, have been carried out on extremely thin target foils in which, on average, one or zero interactions would take place, making the foil thickness a reasonable approximation for the pathlength traversed by emerging quanta. A plane wave representing the incident electron enters the nuclear field of a target atom and has a small probability of emitting a photon after being scattered. In the diagnostic energy range, for nuclei of charge Ze and incident electrons of kinetic energy T and total energy $T + m_0c^2$, the differential cross section for emission of a photon of energy between $h\nu$ and $h\nu + d(h\nu)$ is:

$$d\sigma_{\text{rad}} = \sigma_0 B Z^2 \frac{T + m_0c^2}{T} \frac{d(h\nu)}{h\nu} \text{ cm}^2/\text{nucleus} , \quad (1.3)$$

$$\text{where } \sigma_0 = \frac{1}{137} \left(\frac{e^2}{m_0c^2} \right)^2 = 5.80 \times 10^{-28} \text{ cm}^2/\text{nucleus} , \quad (1.4)$$

and B is a somewhat controversial coefficient which varies slowly with Z and T . Results originally due to the nonrelativistic quantum theoretical approach of Sommerfeld^{1,6} suggest that, over the diagnostic energy range, B decreases gradually from 10 to about 7 as the photon energy increases from zero to T . Compared to classical theory, which predicts a large number of low-loss interactions, quantum mechanical theory predicts a smaller number of large-loss events. Total energy-loss predictions are about equal, but the expected emitted photon spectrum differs markedly between the two models. Experiments confirm the correctness of the quantum mechanical approach.

1.2.2 Electron-Impact X-ray Sources

By far the most common type of X-ray source is the electron-impact X-ray tube. All clinical X-ray sources, including those used for standard radiography, CT scanning and mammography, are of this type. A typical high-flux X-ray tube for diagnostic radiology is shown in Figure 1.3⁷. Electrons emitted from a heated filament are accelerated through a large potential and made to impinge upon a small area of a solid metallic target or anode. The “technique” or “technique factors” employed in making an X-ray exposure refer to the voltage (kVp for “kilovolts, peak”) applied to the tube and the electron current (mA) passing through it. The kVp primarily influences the energy of photons in the beam, and therefore their penetrating capacity, while the mA is linearly related to the total photon energy (flux) in the beam. Most of the radiation produced in these tubes is the broadband Bremsstrahlung emitted when the electrons are slowed to rest in the anode material. If the electron accelerating voltage is high enough to impart to the electrons adequate energy to eject inner-shell electrons from atoms in the target, a small fraction of the emitted flux may consist of photons possessing energies characteristic of electron shell transitions. This section describes the circuits and hardware required for routine production of X rays by tubes, the design of tubes for clinical imaging, the spectra they emit and methods of shaping them, and specialized sources for mammography and research applications.

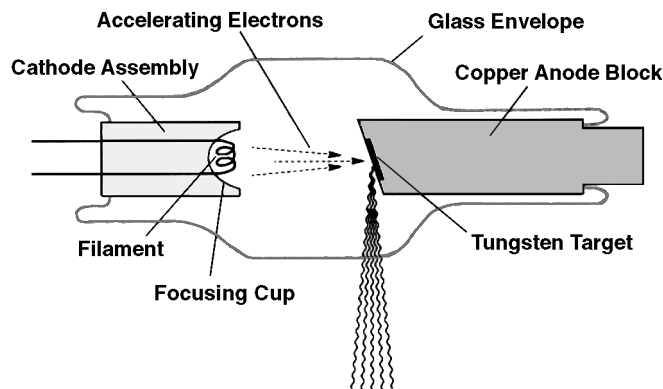


Figure 1.3. Schematic of a stationary-anode, clinical X-ray tube. (Reprinted with permission from Wolbarst, 1993⁷.)

1.2.2.1 Electrical Circuits for X-ray Tubes

All electron-impact X-ray tubes require a stable high voltage to be applied between the cathode, from which the electrons are emitted, and the positive anode upon which they impinge. The magnitude of this applied voltage determines the penetrating capacity of the X-ray beam produced by the tube. Since

there is an optimum applied voltage for any particular imaging task, it is important that the power supply provide a stable, constant direct current (DC) voltage. Here we briefly consider the circuit elements required to achieve this objective, and how they are combined in practical high-voltage generators for clinical X-ray sources.

Transformers are used to increase or decrease the magnitude of the available line voltage. In order to acquire enough energy to produce X rays useful for clinical imaging, electrons have to be accelerated through very high electric field gradients produced by applied potential differences of between 10 000 and 140 000 volts. Since the alternating current (AC) power supplied by electrical utilities to consumer hospitals is usually either 110 or 220 volts, a device is needed to step these voltages up many fold. Transformers in X-ray generators change the amplitude or voltage of an alternating current by the process of mutual electromagnetic induction⁸. In the simplest air core transformer, two adjacent, insulated coils of wire each set up in the other an induced electromotive force. The input coil is called the primary, and the output is referred to as the secondary. Alternating current flowing through the primary causes a magnetic field to be set up in its vicinity. The oscillating magnetic flux links with the secondary coil and induces an AC current (I) to flow through it. The voltage (V) in each coil is proportional to the number of turns (N), or windings:

$$\frac{V_p}{N_p} = \frac{V_s}{N_s}, \quad (1.5)$$

where the subscripts refer to the primary and secondary. Ignoring the slight loss of energy, the output and input powers are equal:

$$V_p I_p = V_s I_s. \quad (1.6)$$

If there were 500 turns on a 220-volt, 55-kilowatt primary, the output of a 250 000-turn secondary would be 110 000 volts at 500 milliamps. Step-up transformers have more turns on the secondary and increase the voltage at the output relative to the input, while step-down transformers are used to decrease the output voltage.

Real transformers are not perfectly efficient, and energy losses – due to resistance of the windings, eddy currents, and magnetic domain hysteresis – are ultimately manifested as heat. Proper design should keep these losses to less than five percent. Thicker copper windings, particularly on the high-current primary, minimize resistance losses. The efficiency of the simple insulated coils of the air core transformer can be improved by insertion of iron cores into the windings as in the open core transformer depicted in Figure 1.4⁸. Magnetization of the core markedly increases the intensity of the magnetic flux set up by the alternating current through the coil, but significant losses persist due to leakage at the ends of the cores. Leakage is much lower in closed core transformers, shown in Figure 1.5, since the magnetic flux

passes through a continuous core from one coil to the other. The most efficient and popular design is the shell-type transformer shown in Figure 1.6. Both heavily-insulated coils are wound around the same central pole in the core. The cores of closed core and shell-type transformers are made up of laminated steel layers. Insulation between the layers minimizes losses due to eddy currents induced by the AC in the windings.

An autotransformer is a special type of transformer used to regulate the voltage input to the primary of the high-voltage step-up transformer. In an X-ray tube, the autotransformer provides the ability to select the kVp applied to the tube. Although the same objective could be accomplished with a variable resistor, autotransformers are selected for kVp control of X-ray tubes, since energy losses are much less than those associated with resistors. As shown in Figure 1.7, an autotransformer consists of a single winding. The taps on the primary side span a fixed number of turns, usually somewhat less than the total. One of the taps on the secondary side is variable, allowing the output to span a selectable number of turns. The ratio of the autotransformer output to the input voltage is determined by the number of turns spanned at the output

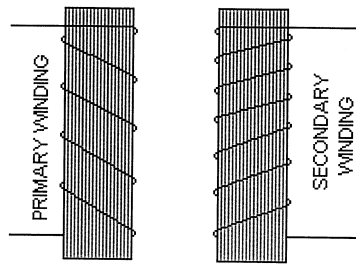


Figure 1.4. Open core transformer for X-ray generator. Iron cores within the windings improve efficiency of magnetic flux generation. (Adapted from Selman, 1994⁸.)

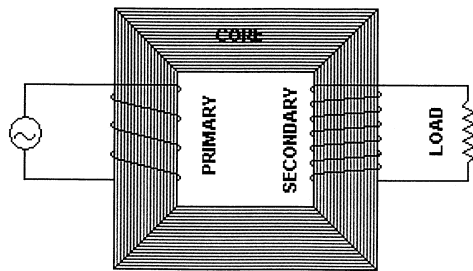


Figure 1.5. Closed core transformer. Leakage is reduced and efficiency improved by continuous conducting path between windings. (Adapted from Selman, 1994⁸.)

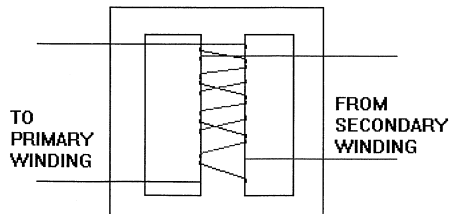


Figure 1.6. Shell-type transformer. Primary and secondary windings share the central member of the core for maximum efficiency. (Adapted from Selman, 1994⁸.)

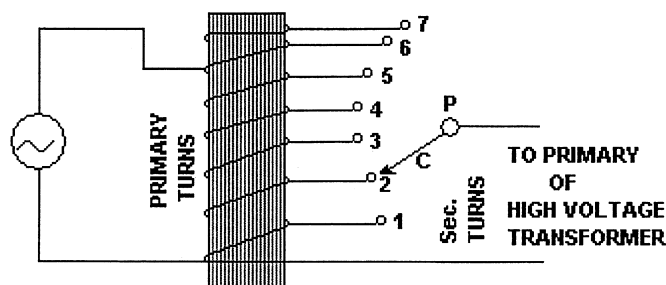


Figure 1.7. Schematic of autotransformer for kVp selection. (Adapted from Selman, 1994⁸.)

relative to the number of turns spanned at the input. Autotransformers are suitable for selection of output voltages which differ from the input voltage by less than an order of magnitude.

Rectifiers permit the flow of electrons through X-ray tubes in one direction only: from the cathode to the anode. If a high-voltage alternating current were applied to the cathode-anode system of an X-ray tube, current would only flow through the tube for that half of the AC cycle during which the cathode was negative relative to the anode. Rectification, defined as changing alternating to direct current, requires construction of a circuit through which current can only flow in one direction. Since the heated filament is an efficient source of electrons separated by vacuum from the anode, normally a very inefficient source of electrons, application of an alternating current to the tube would result in generation of a pulsating X-ray beam which would be on during only half of the cycle period. The tube would self-rectify. This is undesirable since not only is the tube only producing X rays half the time, but most of the time the potential applied to the tube will not be equal to the optimal kVp for the imaging task at hand. Further, a self-half-rectified tube will be able to withstand less heat loading than the optimal design because the anode can never be allowed to reach temperatures so high that they promote electron emission from the target material. Such electrons would flow to the filament during the half-cycle it was positively biased with respect to the “anode”, damaging the filament and shortening its life. Anode damage (melting, pitting and cracking) is minimized by bombarding the surface with the steadiest possible stream of electrons over the required exposure time: another motivation for stable, DC tube excitation.

An important design goal for the X-ray generator is to produce a stable constant voltage for application to the tube. Rectification may be accomplished by the use of solid state diodes, which have largely replaced the vacuum diode tubes of older-generation X-ray apparatus. Diodes permit the flow of current in only one direction. If a battery and load are connected in series with a p-n junction semiconductor diode, the electrons from the n-type half of the diode can only cross the “potential hill” at the junction when the negative battery terminal is connected to the n-type side (the diode is in forward bias):

If the connections are reversed (reverse bias), no current will flow. A large number of solid state diodes (about 150) need to be packaged in series to produce a single rectifier (still referred to as a “diode”) for an X-ray tube because a single semiconductor (doped silicon) diode element can only withstand a reverse bias of about 1000 volts or less before breakdown occurs by the avalanche or Zener effect ⁹.

For half-wave (“single-pulse”) rectification, a single diode in series between the transformer secondary and anode, or two diodes, one on the anode side and the other on the cathode side, will serve to allow passage of electrons through the diode, and hence the tube, only during the half cycle when the diode is forward biased. The tube will never be allowed to enter reverse bias, but X rays will only be generated over less than half of the AC cycle (Figure 1.8, top panel) ². Full-wave (two-pulse) rectification is achieved by arranging four diodes in a bridge circuit as shown in Figure 1.9⁷. During each AC half cycle, electrons will flow through two parallel diodes in the direction opposite to the arrow of the diode symbol. The tube will never enter reverse bias and current will flow through the tube during the entire cycle. While more efficient than half-wave rectification and sometimes used in practice, especially on older systems, a single-phase, full-wave-rectified waveform is not optimal for application to the X-ray tube since the kVp will still differ from the optimal value during a significant portion of the cycle (Figure 1.8, second panel).

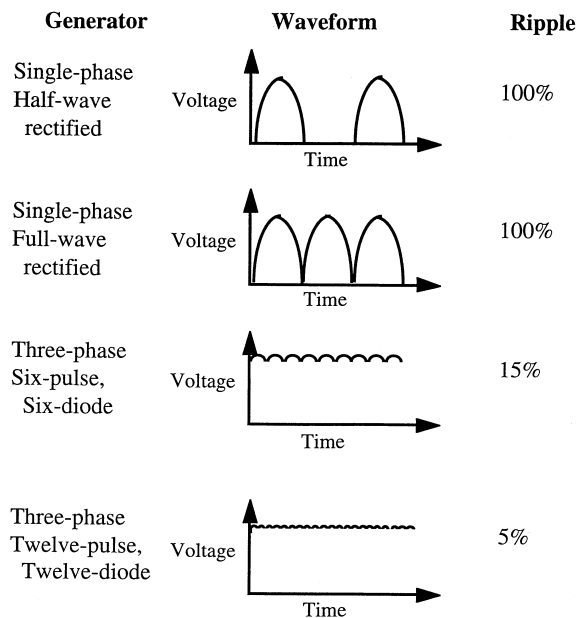


Figure 1.8. Waveforms of the potential applied across the cathode-anode gap by various types of X-ray generator. (Adapted from Bushberg *et al.*, 1994².)

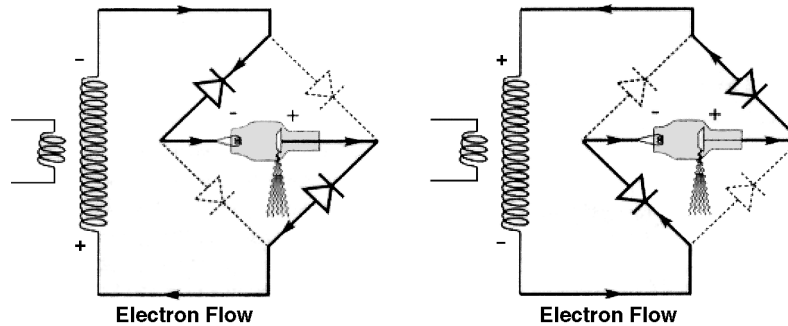


Figure 1.9. The four-diode bridge circuit for full-wave rectification. (Reprinted with permission from Wolbarst, 1993⁷.)

A three-phase generator serves to maintain the potential across the tube at a more constant value than a single-phase unit. The power supply to a three-phase generator consists of three, single-phase power supplies which are 120 degrees out of phase with each other. Three transformers are required to step up the voltage. The three primaries are connected in a “delta” or triangular configuration; the secondaries may be configured either as a delta or a star (or “wye”) as shown in Figure 1.10 and 1.11^{7,8}. The “six-pulse, six-diode” configuration of Figure 1.10 supplies six pulses to the tube every 1/60th second. A slight modification provides “12-pulse, 12-diode” excitation with the circuit of Figure 1.11. The waveforms corresponding to these circuits are shown in the third and fourth panels of Figure 1.8.

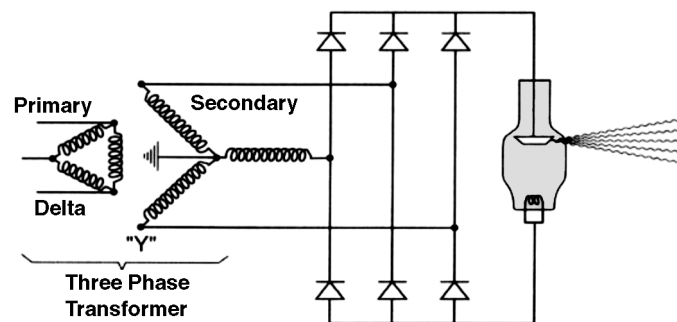


Figure 1.10. The delta, wye, three-phase transformer for six-pulse, six-diode high-voltage excitation. (Reprinted with permission from Wolbarst, 1993⁷.)

Medium- and high-frequency X-ray generators represent the state of the art in X-ray tube electronics. These devices incorporate circuits which full-wave rectify, then smooth the (single- or three-phase) line voltage using capacitive filtering. An inverter “chops” the nearly-constant DC voltage at between 5

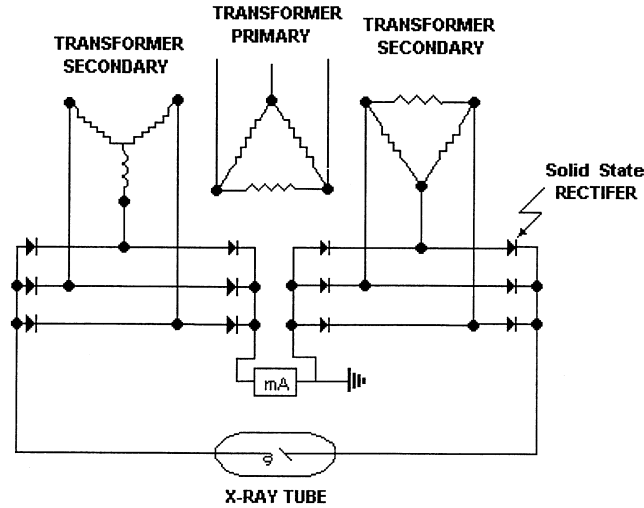


Figure 1.11. Simplified schematic of the generator circuit for twelve-pulse, twelve-diode tube excitation. (Adapted from Selman, 1994⁸.)

and 100 kHz, producing a high-frequency, low-voltage AC waveform which is easily step-up transformed and stabilized. This high-frequency, high-voltage AC is full-wave rectified and smoothed a second time, providing a nearly-constant potential to the tube. In addition, transformer efficiency improves with AC frequency, permitting smaller, lighter generator designs. High-frequency generators (20 or 100 kHz) are frequently employed for mammography due to dose reductions of approximately 25%⁸.

Voltage ripple, expressed as a percent, is defined as:

$$\% \text{Ripple} = \left[\frac{V_{\max} - V_{\min}}{V_{\max}} \right] \times 100. \quad (1.7)$$

Half-wave and full-wave rectification both produce waveforms with 100% ripple; three-phase, six-pulse and three-phase, twelve-pulse generators exhibit about 15% and 5% ripple, respectively; and medium- and high-frequency generators produce about the same voltage ripple as the best three-phase units: 5% or less.

1.2.2.2 Cathodes and Anodes

The electrons accelerated to produce X rays in the tube are emitted from a filament, similar to that in a light bulb. The filament is usually a fine, coiled tungsten wire. A low-voltage (6–12 volts) current (3–5 amps) is passed through the filament, heating it, lowering the work function of the metal, and facilitating the release of electrons from the wire's surface by thermionic

emission. At white heat, electrons may be literally “boiled off” the surface of the wire. The filament current is supplied by a low-voltage circuit. A rheostat (variable resistor), saturable reactor, or high-frequency filament control circuit allows the current flowing through the filament, and therefore the tube current (mA) to be varied. Small increases in temperature can lower the work function of the filament material significantly and cause large increases in tube current. Older equipment usually had an ammeter in series with the filament circuit by which the filament current could be monitored. Modern X-ray tubes are equipped with a high-frequency filament controller or a space charge compensator which uses a feedback mechanism during exposure to match the filament current with the chosen mA (tube current). A small change in filament current causes a large change in the tube mA and therefore the X-ray flux emitted from the tube. The filament controller corrects for temporal fluctuations in the supply line voltage so that changes of $\pm 10\%$ in line voltage result in only fractional percent changes in filament current. Both ends of the filament wire are connected to the low-voltage filament circuit, and one of them is also connected to the negative terminal of the high-voltage power supply across the tube.

The filament may be contained in a “cathode block” which includes a cup-shaped surface, facing the anode, negatively biased with respect to the filament. This focusing cup repels the emitted electrons and serves to confine them to a more tightly-focused beam. In the absence of an applied potential between the cathode and the anode, electrons emitted from the filament cluster in its vicinity. Their mutual repulsion limits the emission of additional electrons from the wire, and actually forces some of the electrons back into the filament. At equilibrium, a “space charge” or cloud of electrons, forms at the filament tip. When a high voltage is applied to the tube, making the anode positive with respect to the filament, electrons are drawn from the space charge and accelerated toward the anode. The excited volume at the anode surface in which the electrons are stopped is called the focal spot. Bremsstrahlung and possibly characteristic X rays are emitted in all directions from the focal spot. Some tubes are provided with two filaments: a larger coil of coarser wire for short, high-mA exposures (to minimize image degradation due to patient motion, for example), and a shorter, finer coil for longer exposures used for exams in which perception of fine image detail is important and motion is less of a problem. The smaller filament produces a smaller focal spot lessening image degradation due to penumbral blurring.

The essential requirements of the anode, or tube target, are that it emit X rays efficiently in response to electron bombardment and that it withstand without damage the high thermal loads imposed by the rapid deposition of large amounts of energy. The first requirement favors a high-Z material; the second, high melting point, good thermal conductivity, and toughness. A denser target possesses the additional, lesser, advantage that electrons are stopped in a smaller excitation volume from which the X rays are emitted. A number of candidate anode materials and their important physical properties are shown in Table 1.1. Most of them are not commonly used in conventional

tubes for clinical imaging but may be employed in the special purpose research and microfocal instrumentation described in Sections 1.2.2.8 and 1.2.4.2. Tungsten (W), with its very high melting point and reasonable thermal conductivity and density provides a near-ideal combination of properties for use as an anode material. Tungsten is the choice for almost all X-ray tube anodes. (Its high melting point also explains its utilization as the filament material.) A tungsten-rhenium alloy which is tougher, and therefore resists cracking and tearing in response to thermal stresses set up by steep thermal gradients, is employed in some tubes.

Table 1.1.

Target Material	Atomic Number	Atomic Weight	Thermal Conductivity (W/cm·K)	MP (C)	Density
Be	4	9	2.18–1.68	1273	1.85
Al	13	27	2.36–2.40	660	2.70
Ti	22	48	0.224–0.207	1660	4.54
Cr	24	52	0.965–0.921	1857	7.18
Fe	26	56	0.865–0.720	1535	7.87
Co	27	59	1.05–0.890	1495	8.90
Ni	28	59	0.941–0.827	1453	8.90
Cu	29	64	4.03–3.95	1083	8.96
Mo	42	96	1.39–1.35	2617	10.22
Pd	46	106	0.716–0.730	1554	12.02
Ag	47	108	4.29–4.26	962	10.50
Sn	50	119	0.759–0.704 (Orientat.-depend.)	232	5.7–7.3
Ta	73	181	0.574–0.577	2996	16.65
W	74	184	1.77–1.63	3410	19.30
Pt	78	195	0.717–0.717	1772	21.45
Au	79	197	3.19–3.13	1064	18.88

The separation from the filament to the anode is generally on the order of a few centimeters. The polished surface of the anode which is bombarded with electrons is inclined at a slight angle, generally in the 7–20° range, with respect to a plane perpendicular to the filament-anode axis, as shown in Figure 1.12⁸. Due to the line-focus principle, the apparent focal spot “seen” by the film or detector is smaller than the bombarded area of the anode, a phe-

nomenon known as foreshortening. This allows the thermal load on the target to be distributed over a larger area for a given effective focal spot size. The width of the focal spot (in the plane perpendicular to the page in Figure 1.12) is the same as that of the excited volume on the target, but the apparent height of the focal spot (H_a), at the center of the field, is related to the real height of the bombarded area (H_b) by $H_a = H_b \sin \theta$, where θ is the angle of the anode surface with respect to the vertical. The apparent height of the focal spot toward the anode side of the tube is less than this value (as evident from Figure 1.12), providing higher spatial resolution, while the focal spot dimension toward the cathode side of the tube is larger.

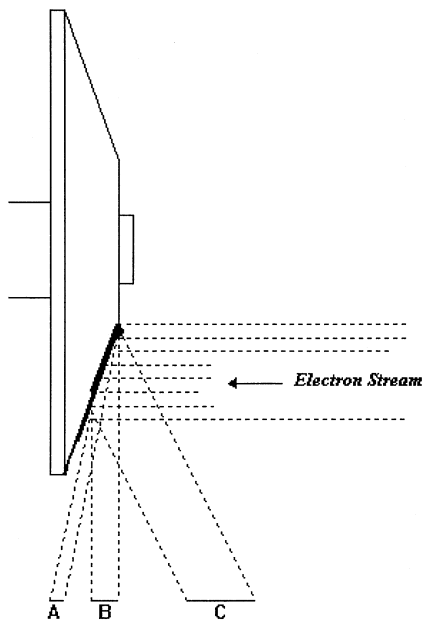


Figure 1.12. An angled anode distributes the thermal load over a larger area for a given focal spot size seen by the film. Foreshortening causes the effective focal spot height to vary over the film as shown. (Adapted from Selman, 1994⁸.)

An undesirable consequence of an angled anode is known as the “heel effect”. Even though the range of electrons in a tungsten target at diagnostic energies is on the order of microns, X rays emerging toward the anode side of the focal spot have to escape, on average, from deeper depths in the target, and undergo considerably more self absorption in the anode on their path toward the film, than rays on the filament side of the beam. This increased filtration preferentially removes lower-energy photons from the beam, causing the average and equivalent energies of the beam to be greater toward the anode side of the exposed field.

1.2.2.3 Sources for Diagnostic Radiology

In stationary anode tubes, the fixed anode assembly is often composed of a copper bulk material with a polished tungsten button embedded into the surface forming the actual target. The superior heat conduction properties of copper aid in dissipating the extreme thermal loads encountered during operation of the tube. In rotating anode tubes, a tungsten-rhenium-coated molybdenum anode disk is mounted on the shaft of a high-speed motor. During exposures, the anode rotates and the energetic electrons impinge upon an angled, annular strip around the anode called the focal track. This increases the bombarded target area by several hundred fold compared to stationary anode devices, and provides dramatically increased heat loading capacity. Molybdenum, with its lower thermal conductivity, prevents transmission of excessive heat to the motor bearings. Rotating anodes are generally either three or five inches in diameter, and rotate at speeds between 3 000 and 10 000 rpm. Larger diameters and higher rotation speeds are associated with higher-heat-load equipment like helical CT scanners which have adequate heat loading capacity to provide continuous, multi-second exposures. While general-purpose stationary anode tubes have focal spots in the 2–4 mm range, rotating anode, dual filament tubes may have focal spots between 0.3 and 2 mm.

A complete circuit diagram of a generator for a full-wave rectified X-ray tube is shown in Figure 1.13⁸. The primary, or low-voltage circuit comprises all the components upstream of the high-voltage, step-up transformer. The kVp meter across the primary circuit is calibrated at the factory to establish the precise relationship between the AC voltage at the secondary of the autotransformer and the DC potential across the tube. In general, the center of the secondary of the step-up transformer is grounded: a large, positive potential is applied to the anode, while a negative potential of equal magnitude is applied to the cathode. A milliammeter in series with the secondary circuit indicates the tube current.

In operation, for a given filament current and no applied tube potential, a space charge of magnitude proportional to the filament current will form on the filament side of the cathode-anode gap. As the kVp across the tube is increased from zero, at low kVp more and more electrons will be drawn from the space charge and accelerated toward the anode, causing a rapid increase in the tube current as shown in Figure 1.14². Above a threshold kVp, all electrons emitted from the filament will immediately be accelerated toward the anode: The space charge will have been entirely depleted, and the tube current will have reached the maximum value achievable with that particular filament current. In the low-kVp regime, the tube current and therefore the emitted X-ray flux is said to be space-charge-limited. The tube current depends on the rate at which the applied potential can pull electrons out of the space charge. After the space charge is depleted, tube output is “emission limited”, meaning that the filament temperature imposes the limit on the rate of electron release. In the emission-limited regime, where X-ray tubes should be operated, tube current can be controlled independently from accelerating

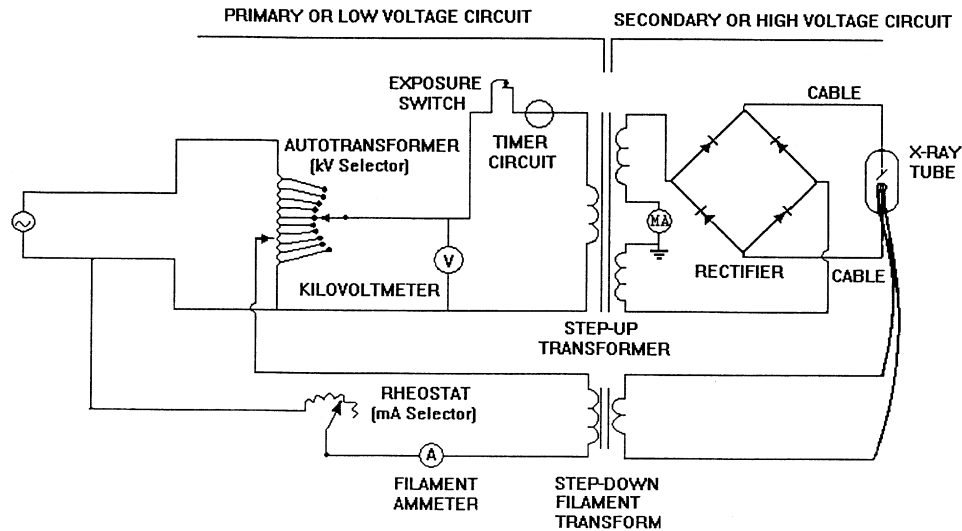


Figure 1.13. Circuit diagram of a generator for a full-wave rectified X-ray tube. (Adapted from Selman, 1994⁸.)

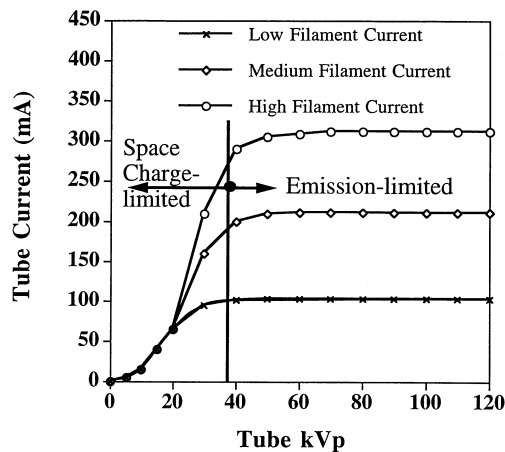


Figure 1.14. Tube current as a function of kVp for various filament temperatures. Operation in the emission-limited output regime permits independent control of kVp and mA. (Adapted from Bushberg *et al.*, 1994².)

potential by varying the filament temperature. The space charge compensator automatically controls the filament temperature to allow the kVp to be raised while the selected mA is maintained.

The field-emission X-ray source is a specialized type of electron impact source in which the filament is not heated. Field emission is an alternative to thermionic emission which usually (in electron microscopes) exploits the fact that a single crystal of tungsten or other metal, when correctly oriented with respect to the applied field, has a much lower work function than rolled or drawn material, allowing electrons to tunnel through the potential barrier at

the surface under the influence of a strong electric field in the absence of heating. The technology was originally reduced to routine practice in electron microscopy^{10,11} because the very high current densities at the cathode (10^3 – 10^7 A/cm² compared to 10 A/cm² for thermally-assisted tungsten) allowed the formation of nm-order electron probes orders of magnitude brighter than available in conventional instruments.

Use of the field-emission principle in microfocal X-ray tubes was advocated in 1957 by Pattee¹² and possibly earlier by others¹³. Subsequently, use of field emission sources for diagnostic radiology has been suggested¹⁴, though they have never come into routine use. In the larger-focal-spot, high-flux design proposed for clinical use, the anode was a tungsten cone with axis coincident with the beam axis. An array of sharp needle assemblies surrounding the cone served as the cathode. Though unclear from the literature, it is likely that polycrystalline cathode needles were used, increasing the average work function at the surface due to random grain orientation and compromising the available beam current. Pulsing the target briefly to voltages as high as 350 kV resulted in the emission of a high-current stream of electrons from the needle tips which produced a flash of X rays. A sequence of pulses at 1000 Hz was used to obtain the exposures required clinically. The advantages of the design included the circular symmetry of the focal spot which avoided the deleterious effects on image quality and exposure uniformity due to the heel effect, the source size was independent of tube current, the spatial resolution at the image plane could be improved by a factor of two or more, and the tubes could be very compact. The primary disadvantages were the difficulty in obtaining adequate flux for imaging the torso and the very high vacuum ($\sim 10^{-9}$ torr) required to avoid contamination of the cathode surface. Even a few atoms on the crystal surface can raise the work function dramatically, seriously reducing the available flux.

1.2.2.4 X-ray Tube Ratings

X-ray tubes are generally rated by manufacturers as to the permissible power loading of the focal spot, the heat storage characteristics and cooling rate of the anode, and the cooling rate of the housing. These ratings are supplied as charts, which must be specific for each tube and combination of operating conditions: generator type, focal spot size and anode rotation speed. For example, a stationary-anode tube is far more susceptible to thermal damage from excessive power loading than is a rotating-anode tube, which dissipates heat over a larger surface area on the target. Similarly, three-phase units tolerate heat considerably better than single-phase tubes. Variations in focal spot size and anode rotation speed are also important considerations.

Power loading limitations determine the maximum exposure time that can be tolerated by the anode without damage for a single exposure at a particular combination of tube voltage and current. A typical single-exposure rating chart is shown in Figure 1.15. Either kVp or mA is plotted vs. exposure time with each of the several curves corresponding to a discrete mA or kVp

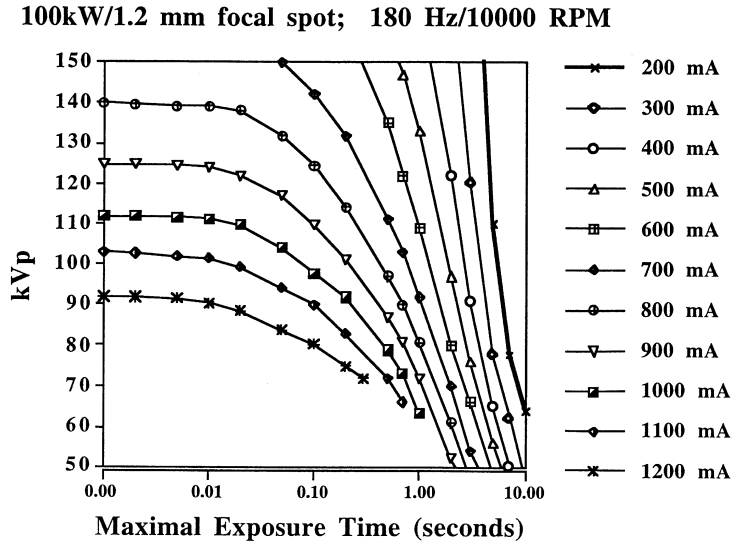


Figure 1.15. Rating charts for an X-ray tube under various operating conditions. (Adapted from Bushberg *et al.*, 1994².)

value, respectively. The safe operating regions are below and to the left of the curves. For a given exposure time, the product of kVp and mA on each of the several curves will always be approximately constant and equal to the tube's power rating in kW.

Heating and cooling of the anode and tube housing is quantified in heat units (HU). This convention evolved as a convenient way to calculate energy deposition into the device from the parameters readily available to the operator: kVp, mA and exposure time. For a single-phase, full-wave rectified unit:

$$1 \text{ HU} = 1 \text{ kVp} \times 1 \text{ mA} \times 1 \text{ second} \approx 0.75 \text{ J}, \quad (1.8)$$

since the average voltage is about 75% of the nominal setting³. For three-phase generators (nearly constant voltage):

$$1 \text{ kVp} \times 1 \text{ mA} \times 1 \text{ second} = 1 \text{ J} \approx 1.35 \text{ HU}. \quad (1.9)$$

A typical chart depicting anode thermal characteristics is shown in the left panel of Figure 1.16³. For the rising curves, if a tube is operated continuously (fluoroscopic mode) for the length of time on the x axis at the heat input rate associated with the curve, the number of heat units on the y axis will have been deposited in the anode. The curves are nonlinear because as the anode temperature rises heat escapes faster. At longer times the curves tend to level out as the rate of heat dissipation almost equals the deposition rate. The descending curve quantifies the cooling rate after operation is discontinued and

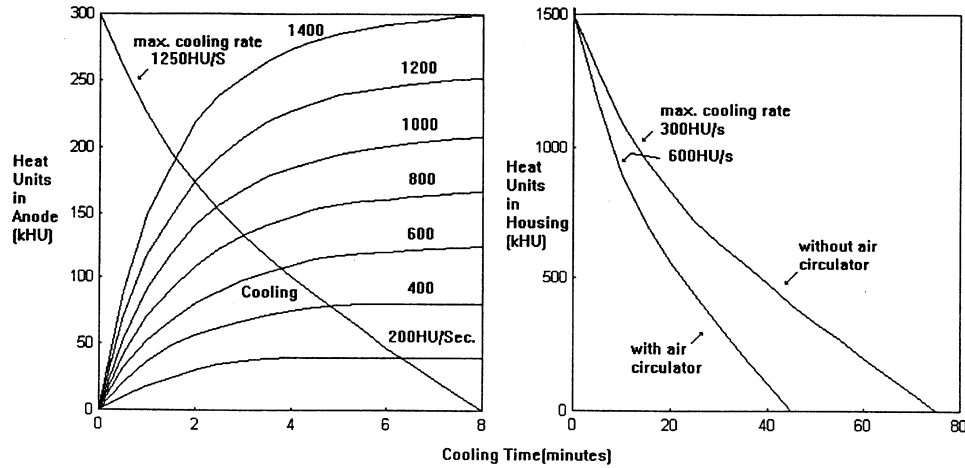


Figure 1.16. Left panel shows anode heating characteristics for various heat input rates versus operation duration and the time required for cooling. Right panel shows housing cooling curves with and without air circulation. (Adapted from Johns and Cunningham, 1983³.)

is useful for determining the waiting time required before another continuous exposure can be initiated. The right panel in Figure 1.16 shows a housing cooling curve. The advantage of active cooling of the housing is evident.

1.2.2.5 X-ray Tube Spectra

In day-to-day clinical practice, it is generally not possible to accurately characterize or measure the spectrum of photon energies present in the X-ray beam. For research applications, for example to develop quantitative, multi-spectral imaging techniques and verify their performance, it is highly desirable to know the X-ray spectrum accurately. Attempts have therefore been made to measure and calculate it as discussed below. For routine purposes, however, it generally suffices to know the values of a small number of parameters which affect the number of photons emitted from the tube and govern the shape of the spectrum of photon energies.

The spectral distribution of the emitted photons is primarily influenced by the kVp, the target material, and by beam filtration. The potential applied to the tube governs the maximum energy of photons in the beam: higher kVp produces higher-energy radiation. The energies at which characteristic emissions occur are a function of the binding energies of anode atomic electrons causing higher-*Z* targets to produce higher-energy characteristic peaks in the emitted spectrum. Inherent filtration (attenuation by the glass envelope of the tube and any other material layers through which the beam must pass) and added filtration preferentially remove low-energy photons from the beam (mostly by photoelectric absorption, as described in Section 1.3.3.1), shifting the average energy of the beam to higher values.

The important characteristics of the shape of the emitted spectrum are embodied in the “quality” of the beam, as measured by the half-value layer. “Harder” beams have “higher quality”, which means that they contain a higher proportion of high-energy photons, possess higher average and equivalent energies, and can therefore penetrate greater material thicknesses. “Lower quality” beams are beams which contain relatively more “soft”, or low-energy photons. The half-value layer, or HVL, is defined as the thickness of any material required to reduce the exposure rate of an X-ray beam to half its incident value^{3,8,15}. Since X-ray attenuation is exponential (as discussed in Section 1.3):

$$\frac{I}{I_0} = \frac{1}{2} = e^{-\mu \cdot \text{HVL}} \quad (1.10)$$

$$\ln\left(\frac{1}{2}\right) = -\mu \cdot \text{HVL} \quad (1.11)$$

$$\text{HVL} = \frac{0.693}{\mu} \quad (1.12)$$

where μ is defined as the linear attenuation coefficient of the material used to attenuate the beam. Definitions of HVL found in the literature are often ambiguous as to whether the quantity being halved is exposure rate or intensity as Eq. (1.10) would imply^{2,16–21}. For monoenergetic beams, defining HVL in terms of intensity or exposure would be equivalent, but for polyenergetic beams this is not the case because exposure is defined in terms of liberated charge per mass of air (see Section 1.4.4). Because the mass energy absorption coefficient of air exhibits a strong inverse energy dependence, the HVL of a soft polychromatic beam would be found to be thinner using exposure measurements than using intensity measurements. Energy-integrating detectors suitable for intensity measurements do not lend themselves to routine use in radiology, primarily due to count rate limitations. Since exposure is nearly always the quantity measured in practice it seems reasonable to define HVL in these terms, in spite of the apparent conflict with Eq. (1.10) and the very definition of the linear attenuation coefficient (both of which apply strictly for monoenergetic beams).

For a polyenergetic beam such as those employed in diagnostic imaging, attenuation of the beam by any material will preferentially remove lower-energy photons from the beam. The emergent beam will therefore be “hardened” or shifted to higher energies. If it is desired to determine the second HVL of the beam, defined as the thickness of the material to again halve the exposure, it will be necessary to insert more attenuating material to stop the higher-energy photons: the second HVL will be thicker than the first. It is possible to approximately reconstruct the spectrum by analysis of attenuation data as described by Delgado and Ortiz²² and references 1–16 therein.

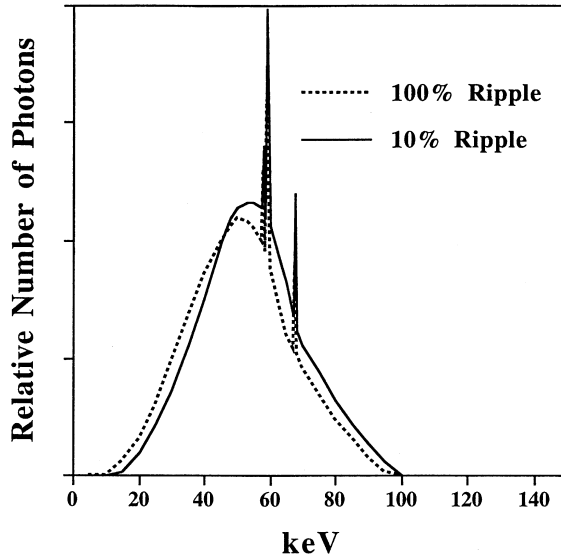


Figure 1.17. Effect of tube potential waveform on output spectrum. (Adapted from Bushberg *et al.*, 1994².)

The voltage waveform applied to the tube can also have an effect on beam quality. Any drop of the applied voltage due to ripple will result in a reduction of the maximum photon energy in the beam, causing a spectral shift toward lower energies as shown in Figure 1.17, and reducing beam intensity and penetrating power². In general this will result in higher dose to the patient and greater heat loading of the anode.

The “equivalent energy” of the beam is defined as the energy of a monochromatic beam which would produce the same results in terms of its penetrating capacity³. A broadband X-ray beam having an equivalent energy $h\nu$ has the same HVL as a monochromatic beam of energy $h\nu$. After measuring the HVL in a practical situation, one can calculate the linear attenuation coefficient according to $\mu = 0.693/\text{HVL}$, then refer to a table of linear attenuation coefficients as a function of energy for the material used in the HVL determination to find the equivalent energy of the beam.

Intensity, with units of energy per unit time per unit area (e. g. keV/sec · cm²), is a measure of the energy in the beam. The beam intensity varies¹⁶ linearly with the product of the tube current and exposure time (mAs) and with (kVp)². As described earlier, classical theory predicts that the efficiency of Bremsstrahlung production should vary as the square of the target atomic number, a relationship which holds reasonably accurately for intensity emitted from thin targets¹. But quantum mechanics predicts, and most texts state^{2,3,18}, that for thick targets the intensity variation with Z is linear:

$$\text{Intensity} \propto \text{mAs} \times \text{kVp}^2 \times Z_{\text{anode}} \quad (1.13)$$

Rao-Sahib and Wittry measured the X-ray intensity produced at discrete kVp settings corresponding to characteristic emission lines using a curved crystal, wavelength-dispersive spectrometer⁴. They investigated 23 elements from $Z = 6$ to $Z = 92$ using polished flat targets in an X-ray microprobe with a take-off angle of 53° . The experimental results did not confirm a linear variation with Z , but indicated that intensity depended on Z^n , where n varied from 1.38 for aluminum ($Z = 13$) to 1.19 for gold ($Z = 79$). In many cases quantum mechanical theory serves to provide correction factors or supplemental terms to the classical results, inclusion of which often provides reasonable agreement with experiment, especially for non-relativistic electrons.

In research settings, when it is required to have precise knowledge of the X-ray spectrum, a histogram of photon energies can be obtained using a solid-state, energy-dispersive X-ray detector such as a high-purity germanium (HPGe) or a lithium-drifted silicon (Si:Li) crystal interfaced to a multichannel analyzer¹⁵. If the count rate is low enough, these detectors can register (detect and count) individual photons and determine their energies to sub-keV accuracy by pulse height analysis. In practice, the count rates (photon fluence) from clinical X-ray tubes are much too high for this type of detector and, if nothing were done to reduce them, pulse pile-up would result. Multiple low-energy depositions in the crystal might be erroneously summed to yield spurious high-energy counts and inaccurate spectral measurement. To remedy this, either a pinhole aperture may be placed in front of the detector or the detector positioned at a great distance from the source²³. In the former case, the spectral intensity would have to be normalized (scaled up) using a separate measurement, perhaps with an ionization chamber, since the true energy fluence at the detector would not be known; in the latter, air absorption becomes a factor. Detector systems of this type normally require cooling of the crystal to cryogenic temperatures, are rather expensive, and are not readily available to many imaging researchers. Less expensive, room-temperature detectors based on silicon photodiodes have been used to characterize diagnostic X-ray spectra²⁴, but the inferior energy resolution of these devices and the necessity of correcting the data for photoelectron escape and scattered counts make these methods of spectral measurement unreliable.

Most direct measurements of X-ray spectra have been obtained for studies of electron-probe X-ray microanalysis, but the results can be compared to the same theories relevant for diagnostic X-ray tubes. Green and Cosslett used a crystal wavelength-dispersive spectrometer in conjunction with a flow proportional counter to measure the X-ray spectrum from a germanium target and to estimate the efficiencies of characteristic X-ray production from ten elemental targets spanning the periodic table from carbon to gold^{25,26}. X rays were detected at a 45° takeoff angle from polished flat solid targets mounted in a special-purpose microfocal X-ray tube. For all elements the efficiencies ranged between 10^{-6} and 10^{-3} characteristic X rays per steradian per incident electron, depending primarily upon the ratio of the incident electron energy to the relevant shell ionization energy. At a fixed kVp, the characteristic production efficiency was found to be a rapidly decreasing function of Z .

These experimental results showed good agreement with their theoretical prediction of the efficiencies for K, L and M shell characteristic X-ray production, accounting for ionization by both electron bombardment and photoelectric absorption of the Bremsstrahlung (see Section 1.3)²⁷. The higher fraction of characteristic radiation produced by low- Z (compared to the ubiquitous tungsten) targets explains their suitability for studies benefitting from quasimonochromatic, low-energy x-radiation.

Because of the difficulties associated with accurate spectral measurements, a number of investigators have attempted to derive analytical methods to predict the spectral output of X-ray sources. The earliest analytical result for the intensity emitted from a thick target may be due to Kulenkampff and Kramers^{28,29}:

$$I_v = kZ(E_0 - hv), \quad (1.14)$$

where I_v is the emitted intensity of photons of energy hv , k is a constant, Z is the atomic number of the target, and E_0 is the energy of the incident electrons. If I , E and hv are in keV and the energy interval unit is 1 keV, then the constant k is equal to⁴ 2.2×10^{-6} . The units of Kramers's result as presented are:

$$\frac{\text{keV}}{\text{electron} \cdot 4\pi \text{ steradians} \cdot \text{keV interval}}.$$

Conversion using:

$$\frac{I_b \times 6.2422 \times 10^{18} \frac{\text{electrons}}{\text{sec}} \times \frac{1 - \cos \alpha}{2}}{\text{keV} / \text{photon}},$$

where I_b is the tube current in amps, yields the photon flux per keV interval onto a circular detector subtending a cone of half-angle α .

Kramers's equation gives the triangular intensity distribution predicted by quantum mechanics and provides reasonably accurate, if fortuitously so, estimates of X-ray intensity production in thick targets. Fortuitously, some have claimed, because two simplifying assumptions in Kramers's approach may have cancelled each other out⁶: He assumed that the coefficient B in the equation for the differential radiative cross section of the target nucleus (Eq. 1.3) is constant, when in fact it is a slowly decreasing function of energy, and he neglected self-absorption in the target. Assuming B to be constant would cause the predicted spectrum to be too hard, but neglecting the beam-hardening effect of self-filtration in the anode compensated in part for this error.

Soole⁶, Birch and Marshall³⁰, and Tucker, Barnes and Chakraborty³¹ all used similar approaches to derive analytical expressions for the spectra emitted from thick metallic targets bombarded by electrons of constant

kinetic energy. Tucker, *et al.* have shown that the number of photons with energy between $h\nu$ and $h\nu + d h\nu$ produced per incident electron (before self-filtration by the target material) can be derived from Eq. (1.3) to be:

$$N(h\nu)d h\nu = \frac{\sigma_0 Z^2}{A} \frac{d h\nu}{h\nu} \int_{h\nu}^{T_0} \frac{B(T + m_0 c^2)}{T} \left(\frac{1}{\rho} \frac{dT}{dx} \right)^{-1} dT, \quad (1.15)$$

where the symbols have the same meaning as in Eq. (1.3), and ρ and A are the target density and atomic mass. Taking attenuation by the target material into account, this becomes:

$$N(h\nu)d h\nu = \frac{\sigma_0 Z^2}{A} \frac{d h\nu}{h\nu} \int_{h\nu}^{T_0} \frac{B(T + m_0 c^2)}{T} F(h\nu, T) \left(\frac{1}{\rho} \frac{dT}{dx} \right)^{-1} dT, \quad (1.16)$$

where

$$F(h\nu, T) = \exp \left[\frac{-\mu_{\text{target}}(h\nu) (T_0^2 - T^2)}{\rho c \sin \theta} \right] \quad (1.17)$$

gives the attenuation due to filtration by the anode according to the Thomson-Whiddington relation¹. The depth, x , in the anode at which X rays are produced, and the distance, d , through which the exiting beam must penetrate are related by $d = x/\sin \theta$, where θ is the anode angle, and the depth at which electrons with initial energy T_0 have residual energy T is given by:

$$x = \frac{T_0^2 - T^2}{\rho c}, \quad (1.18)$$

where c is the Thomson-Whiddington (T-W) “constant”. Variability between the results for calculated Bremsstrahlung spectra obtained by various researchers is due in part to the values, shown in Table 1.2, assumed for the T-W constant, which increases slowly with electron energy. Soole used values derived from the works of Green and Cosslett²⁷ and Tothill, while Birch and Marshall and Tucker, *et al.* used values derived from Bichsel and the empirical relationship of Katz and Penfold³⁰.

Because of multiple scattering in the target (large number of small energy losses), the depth to which electrons penetrate in the anode will be considerably smaller than their pathlength. A number of practical difficulties, including straggling, make it difficult to experimentally determine the range of electrons in metals. Katz and Penfold gave an early review of the electron energy-range data and proposed a formula for the range (R_0) of electrons with incident energies (E in MeV) between .01 and 3.0 MeV¹:

$$R_0 \left(\frac{\text{mg}}{\text{cm}^2} \right) = 412 E^{(1.265 - 0.0954 \ln E)}. \quad (1.19)$$

Table 1.2.

Incident Electron Energy (keV)	T-W constant ($10^5 \text{keV}^2 \text{m}^2/\text{kg}$) Soole	Birch and Marshall
20	.29	–
25	–	.39
50	.44	.54
75	–	.625
100	.54	.70
150	.57	.84
200	.59	1.0
250	.61	–

This relationship yields shallower depths of penetration than Eq. (1.18) above. For example, for 100-keV electrons in tungsten, the Katz-Penfold equation gives a range of 6.9 microns, while the T-W equation using Birch and Marshall's value for the constant predicts that electrons will have lost all their energy at a depth of 7.4 microns, and Soole's assumed value of the constant yields 9.6 microns.

An important contribution of Tucker's group was to parameterize B as³¹:

$$B = \begin{cases} [A_0 + A_1 T_0] \left[1 + B_1 \left(\frac{h\nu}{T} \right) + B_2 \left(\frac{h\nu}{T} \right)^2 + B_3 \left(\frac{h\nu}{T} \right)^3 + B_4 \left(\frac{h\nu}{T} \right)^4 \right] & , \quad h\nu \leq T \\ 0 & , \quad h\nu > T \end{cases} \quad (1.20)$$

where $h\nu$ is X-ray photon energy, T_0 is the incident electron energy, T is the electron energy, and the coefficients A and B are parameters determined by least-squares fitting of the model's results to a large number of spectra determined experimentally by another group³². The coefficients A determine radiation output and were found to be $A_0 = 3.685 \times 10^{-2}$ photons/electron and $A_1 = 2.9 \times 10^{-5}$ photons/(electron \cdot keV). The coefficients B govern the spectral shape and were -5.049 , 10.847 , -10.516 and 3.842 .

For spectral modeling purposes, the characteristic contribution can simply be superimposed on the Bremsstrahlung component. The intensity of production of characteristic radiation has been found by many investigators to follow the relationship^{26,33}:

$$I_K = C \left(\frac{T_0}{E_K} - 1 \right)^{1.63} \quad (1.21)$$

where C is a constant, T_0 is the incident electron energy, and E_k is the K-shell binding energy. Most experiments have placed the value of the exponent within the range 1.0–1.7, depending upon the value of C . For tungsten, a value between 1.63 and 1.65 is often used. C , and therefore efficiency of characteristic X-ray production for a given T_0 , increases rapidly with decreasing target atomic number. Because of this, attempts to produce quasimonochromatic beams from electron-bombarded targets for biomedical applications have often employed copper, aluminum and silver anodes. For fixed ratios of T_0/E_k (>1), C increases with Z . Characteristic X-ray production initially increases with depth into the target, then decreases as the electrons lose energy. Tucker modeled the production efficiency with depth as a parabolic function which reaches zero at the depth where the average electron energy equals the K-shell binding energy³¹:

$$N(hv_i) = A_k \left(\frac{T_0}{E_k} - 1 \right)^{n_k} f(hv_i) \int_0^R P\left(\frac{x}{R}\right) \exp\left(\frac{-\mu(hv_i)x}{\sin\theta}\right) dx, \quad (1.22)$$

where $N(hv_i)$ is the number of $h\nu_i$ characteristic X rays per incident electron emerging from the target, A_k and n_k are parameters adjusted to fit model results to experimental data, $f(hv_i)$ is the fractional emission for the various characteristic X rays (K_{α_1} , K_{α_2} , K_{β} , etc.), R is the distance at which the average electron kinetic energy equals the binding energy, and x is depth within the target. The parabolic production efficiency function used was:

$$P\left(\frac{x}{R}\right) = \begin{cases} \left(\frac{3}{2}\right) \left[1 - \left(\frac{x}{R}\right)^2\right] & , x \leq R \\ 0 & , x > R \end{cases} \quad (1.23)$$

For 90% tungsten/10% rhenium targets, very good fits to the data were obtained with $A_k = 1.349 \times 10^{-3}$ photons/electron and $n_k = 1.648$.

In general, probably because of the large numbers of adjustable parameters (in particular the parameterization of B), Tucker's results seem to provide the best fit to experimental data, while Kramers's result produces a spectrum of the same shape shifted about 5 keV toward lower energies and lacking the characteristic contribution. Birch and Marshall's publication shows a similar comparison to Kramers's model (though Tucker's implementation of Birch and Marshall produced a badly-skewed spectrum). Considering its extreme simplicity, the accuracy of Kramers's result remains remarkable.

1.2.2.6 Beam Filtration

The X-ray spectrum produced in the anode has the triangular energy distribution predicted by Kramers's rule. There is a preponderance of low-energy photons and very few photons with energies close to T_0 . In general the beam must pass through several layers of material before emerging from the X-ray tube: the target material itself, the glass envelope surrounding the tube and/

or a vacuum window, usually composed of aluminum or beryllium. In addition it may pass through thin layers of oil and plastic. These unavoidable attenuating layers are referred to as inherent filtration, and serve to remove almost all the X rays below about 10 or 15 keV from the beam. Inherent filtration is usually specified in terms of equivalent millimeters of aluminum. Clinical X-ray tubes will typically have several millimeters inherent aluminum filtration (with a minimum imposed by regulations designed to reduce patient dose), while special purpose microfocal tubes may have a few hundred microns of beryllium ($Z = 4$) or less. As the tube ages and the anode and filament materials vaporize in the imperfect vacuum, the inherent filtration increases due to deposition on the output window. For most purposes, even further filtration of the beam is warranted, since low-energy photons have a reduced likelihood of reaching the image receptor and contributing to the image signal but do increase the dose to the patient. The most common practice is to add additional aluminum filtration. Some manufacturers provide the choice of using either a thin copper or aluminum filter.

For research purposes in which narrow-band or quasimonochromatic radiation is useful, it is possible to employ anode/filter material combinations which enhance the production and transmission to the specimen of a selected energy band of radiation. Figure 1.18 shows the K-absorption edges of elements which occur between about 15 and 52 keV³⁴. Since the fluorescent X rays are emitted with energy equal to the difference in binding energy between the two shells involved (usually the K and L shells), they will have

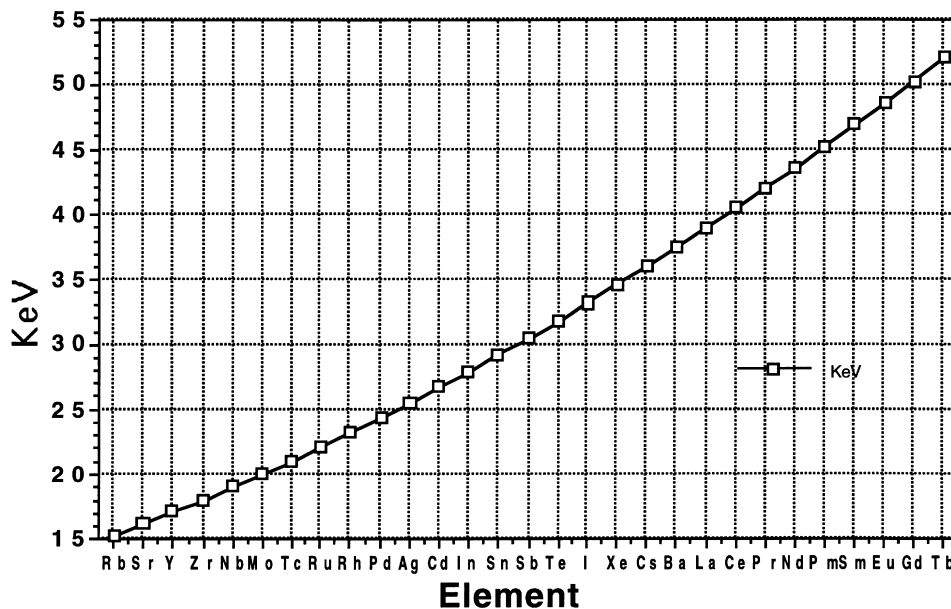


Figure 1.18. Energies of K absorption edges. (Data from Weast³⁴.)

an energy slightly below the K-edge and the target material itself will be relatively transparent to its own characteristic radiation. For example³⁴, a platinum target, with its K-edge at about 78.4 keV, emits K_{α_1} and K_{α_2} fluorescent X rays at about 66.8 and 65.1 keV, respectively, with a $K_{\alpha_2}/K_{\alpha_1}$ emission probability ratio of 0.583. Pt itself could be used as a filter to provide transmission of the radiation between 65.1 and 78.4 keV, while providing increased filtration of lower-energy photons. Enhanced removal of flux just below the characteristic emissions could be achieved by use of an ytterbium filter (K-edge at 61.3 keV), and narrow-band illumination achieved with the combination of either ytterbium and tungsten (K-edge = 69.5 keV) or ytterbium and tantalum (K-edge = 67.4 keV). A serious problem with absorption filtering to tailor the spectrum is that flux is severely reduced, particularly if filters with K-edges below the band of interest (like the ytterbium in this example) are used since, with increasing energy, absorption decreases exponentially below a K-edge, makes a step function up at the edge, then decreases exponentially again. Ytterbium would still absorb quite strongly between 65 and 67 keV.

Another application of beam filters is to equalize the exposure at the image receptor. Equalization or compensation filters present varied thicknesses over the image field to compensate for large variations in body thickness, such as occur between the neck and shoulders or the lungs and mediastinum for chest imaging, or for varied ray path lengths across the field². Tapered wedge filters or hollowed-out trough filters are used for beam equalization in these applications. There is currently research underway to develop equalization methods for mammography where large density variations and the requirements to image the more attenuating areas in the center and near the chest wall are in conflict with the desirability of visualizing the skin line, which tends to get overexposed. Bowtie filters are used in computed tomography to compensate for the ray path lengths at the periphery of the field being shorter than those in the center.

1.2.2.7 Sources for Mammography

Mammography is currently an area of intensive research for several reasons, including the challenging nature of the imaging task, the increased emphasis on women's health and early detection of cancer, the availability of funding, and the imposition of new regulations intended to improve the consistency of quality control nationwide. Being composed entirely of soft tissue – fat, glandular tissue and parenchyma – there is very little object contrast available for transmission X-ray imaging. The difficulty lies in maximizing image contrast while keeping dose to the acceptable, low level required of any screening procedure. In general, dose and contrast both decrease with increasing kVp.

Since subject contrast (see Section 1.3.6 for a discussion of object, subject and image contrast) in this instance is improved by use of low-energy X rays, mammography tubes are optimized to produce radiation in the 17- to 25-keV range. Though efforts are underway to produce monochromatic beams for breast imaging with electron impact tubes using graphite mosaic crystal

monochromators^{35,36} and the possibility of mammography using synchrotron^{37,38} and Compton backscattered (see Section 1.2.5) radiation is being investigated^{39,40}, it is currently impractical to obtain narrow-band radiation in the desired range for mammography. Breast imaging is therefore the most common application of beam filtering to tailor the spectrum from an electron-impact tube. A number of modeling studies have been carried out to determine the optimal spectrum for mammography^{41,42}. Most mammography tubes are operated between 22 and 30 kVp and employ molybdenum anodes and filters. Mo has the K-edge at 20.01 keV, K_{α_1} , K_{α_2} and K_{β_1} lines at 17.48, 17.37 and 19.61 keV, respectively, and $K_{\alpha_2}/K_{\alpha_1}$ and K_{β_1}/K_{α_1} emission probability ratios of 0.525 and 0.197. The production and transmission of radiation with energies between 17 and 20 keV is enhanced with a Mo-Mo anode-filter combination, which increases the photoelectric-to-Compton interaction ratio and improves image contrast for the soft tissues of the breast. Recently some mammography tubes have been provided with both molybdenum and rhodium anodes and filters. Rh has the K-edge at 23.26 keV and K_{α_1} , K_{α_2} and K_{β_1} lines at 20.22, 20.07 and 22.72 keV, respectively. Mo-Mo, Mo-Rh, and Rh-Rh target-filter combinations are possible. (One manufacturer also supplies an aluminum filter.) Studies have indicated that Mo-Rh and Rh-Rh combinations provide some dose reduction relative to Mo-Mo for all breasts at the expense of contrast in the case of small or fatty breasts, both effects due to the higher average energy of the rhodium-filtered beam⁴³. For thick or dense breasts, however, the dose reduction is not accompanied by contrast degradation, suggesting that perhaps both target-filter combinations have their place, depending on patient characteristics.

One requirement of a mammography tube is that it produce a small focal spot for full-breast studies (approximately 300 microns) and even smaller spots for spot magnification studies (about 100 microns). This is achieved by use of a single fine wire filament and a focusing cup which is activated (negatively biased with respect to the filament) for the small-spot mode. The anode is always of the rotating variety with either a molybdenum track or selectable molybdenum and rhodium tracks. The exit window must be thinner than in conventional tubes, and in modern equipment is made of beryllium instead of aluminum or glass, in order to transmit the low-energy radiation. The anode angle is usually smaller than in conventional tubes, which is acceptable because the smaller resulting focal spot is achieved without the problem of restricting the field size. The adverse consequences of the heel effect are minimized by positioning the filament nearer the patient's head than the target so the more intense side of the beam is toward the chest wall.

The Mammography Quality Standards Act (MQSA) of 1992 (interim guidelines currently in effect; final rule expected by 1998) attempts to improve the quality of mammographic imaging nationwide by regulating the facilities performing imaging studies⁴⁴. Among the requirements are annual surveys of the equipment by qualified medical physicists. The focal spot size may be measured by either of the two methods described in the Mammography Quality Control Manual of the American College of Radiology. The

older method involves characterizing the focal spot size using a fine slit to measure the line spread function of the system⁴⁵ if a preliminary star pattern measurement falls out of specification. The newer method characterizes the high-contrast spatial resolution of the system in line pairs per millimeter by use of a bar (line pair) pattern⁴⁶. A complete description of modern mammography equipment, including the tube and generator, and the performance characteristics to be satisfied can be found in the recommended specification by Jaffe *et al.*⁴⁷.

1.2.2.8 Specialized Sources for Research

Besides tubes for clinical use, a wide variety of electron-impact sources have been developed for research and other purposes⁴⁸. One of the most common reasons for this is that standard tubes are designed to produce optimal images from a single type of object: the human body. The attenuation characteristics of individuals in the population and of the various intact body tissues all fall within a relatively narrow range requiring X rays between about 20 and 140 keV. In the research setting it is common to study objects either much more attenuating (usually in nondestructive testing) or much less attenuating, as is usually the case in basic biological research, than the human body. These studies require more versatile instrumentation. For biological research the most common requirement is for low voltage. X-ray apparatus for low-voltage applications must have very thin aluminum or beryllium windows to transmit the low-energy photons. Another parameter of electron-impact sources which has been optimized for high-resolution imaging and chemical analysis applications is the focal spot size.

The extreme case is X-ray microscopy of thin or ultrathin soft tissue sections. Today, most of this type of research is carried out on synchrotrons or with laser-produced plasma X-ray sources, to be described briefly later, but in the 1930's through the 1960's there was a great deal of activity in X-ray microscopy using electron-impact instrumentation. The interest started with Uspenski in 1914⁴⁹ who was the first to appreciate the potential of point-projection magnification, and Ardenne in 1939⁵⁰, who may have been the first to construct a functional instrument for the purpose. In the 1950's, Cosslett and Nixon revitalized the field by producing highly-functional instruments and valuable new results⁵¹⁻⁵⁷. Several manufacturers produced commercial instruments in the 1950's and 1960's, but interest dwindled thereafter, and no dedicated versions are available today.

The two common ways to obtain high-resolution images of biological objects are contact microradiography and point-projection microscopy. For contact imaging, the specimen is placed in intimate contact with a film or photoresist for exposure. The size of the focal spot is not important, since resolution is limited by the film or resist. The developed image is then magnified in the light or electron microscope for viewing. Point-projection magnification is achieved by placing the specimen very close to the source and the detector some distance away. In this geometry, the focal spot size limits the

resolution. Most of the older X-ray microscopes employed sources of the semi-thin, transmission anode variety, which means that the electron beam was focused onto the vacuum side of a thin metal foil target (which either served to terminate the vacuum or was adhered to a beryllium window), through which the X-ray beam emerged into the specimen chamber, usually at atmospheric pressure.

Henke describes an instrument of this type built for contact imaging with large focal spots and very large (up to 1000 mA) tube currents⁵⁸. Excitation voltages and target foils were chosen to provide illumination suitable for chemically-specific imaging of biological constituents. For example the aluminum K-line provided 1.49-keV, the copper L-line 0.93-keV, the iron L-line 0.70-keV, the chromium L-line 0.57-keV, the titanium L-line 0.45-keV and the carbon K-line 0.28-keV radiation. Filters of the same material as the anode were used to attenuate the lower energy photons. Accelerating voltages between 0.3 and a few keV were used which necessitated keeping the target free from all carbon and tungsten contamination from the vacuum system and filament, otherwise the low-voltage electron beam would be prevented from reaching the target and exciting the fluorescent radiation. This was accomplished in part by an inverted design in which the large, coiled tungsten filament was positioned below the anode.

Cosslett and Nixon's instrument shared this inverted design feature, as did commercial versions by General Electric and Philips. Saunders used a Cosslett-Nixon projection X-ray microscope, which produced focal spots as small as 0.1 micron by the use of sophisticated electron optics⁵⁶, to produce beautiful micrographs of a wide variety of biological specimens⁵⁹⁻⁶². Bellman used a hot-cathode, solid-anode diffraction tube with thin beryllium windows to perform what he called microarteriography on 120- to 450-micron sections⁶³. The use of capillary optics to focus broadband X-ray beams to small spots has opened up still another method to improve the flux available in a given size spot⁶⁴⁻⁷⁷. Imaging and X-ray fluorescence analysis instruments employing either single, conical focusing capillaries or arrays thereof have started to be developed and applied to biomedical research.

A number of groups have modified scanning electron microscopes to produce micron-order focal spots for biological investigations⁷⁸⁻⁸⁴. Preferably the specimen chamber is removed and replaced with one having a hole in the roof to which the target foil is mounted on a beryllium window; alternatively, the target and specimen are both accommodated in the vacuum. The lens systems on these instruments are designed to focus the electron beam to tens of nanometers, and very low tube currents are obtained (fractions of a micro-amp) even with the largest apertures and lowest lens currents, necessitating exposure times of tens of seconds or even minutes.

There are two or three manufacturers that currently market microfocal (1- to 20-micron focal spots) X-ray sources, primarily to the nondestructive testing and microelectronics communities. In a few instances, these instruments, which incorporate sophisticated electron lenses and either solid or transmission-type anodes, have been employed for biomedical research⁸⁵⁻⁹¹. A system currently

in use for microtomography of pulmonary microvasculature employs a commercial solid-anode tube which operates over the 5–100 keV range with tens of microamps beam current⁹². The anode is cooled by circulating fluid, allowing operation at 300 watts. The tube is demountable with turbo and backing pumps continually replenishing the vacuum, allowing periodic polishing of the anode and rapid interchange of target materials, and simplifying filament replacement. The anode is a 6-mm diameter rod which can be rotated under vacuum to present fresh surface to the electron beam. Focal spots as small as three microns are available; the beam emerges through a 500-micron beryllium window.

1.2.3 Synchrotron X-ray Sources

For many imaging and spectroscopy applications in biomedical research, it would be desirable to have a source of X rays which provides far higher flux than conventional electron-impact tubes do. When narrow spectral bands of radiation provide the desired signal and information, attempts to filter or tailor the beam from broadband Bremsstrahlung sources using thin-foil filters generally result in reduction of the available flux to such low levels that data collection times become unacceptably long or the acquired photon statistics become unfavorable with respect to signal-to-noise. Because of the kVp^2 dependence of flux available from electron-impact tubes, they are not well-suited for generation of X rays with energies below about 5 keV bright enough to image even very small soft-tissue samples. Synchrotrons are currently the best available sources for fulfilling requirements of high flux and tunable monochromaticity over a spectral range which extends from the infrared to hard X rays. Synchrotron radiation is also highly polarized and collimated, pulsed, and partially coherent, which can be advantageous properties for certain applications. Though exorbitant in cost and inaccessible to the majority of biomedical researchers, synchrotrons fill an important niche in X-ray imaging and spectroscopy science, and have facilitated discoveries which never would have been possible in their absence.

A number of excellent reviews and comprehensive works devoted to the application of synchrotron radiation to biomedical research exist^{93–97}, as do introductory and advanced texts and papers in the field^{98–107}. This section discusses the salient features of synchrotrons as sources of radiation for biomedical research and summarizes some of the important applications and discoveries these sources have made possible.

1.2.3.1 Storage Rings

Synchrotron radiation is emitted when charged particles are accelerated. In particular, when positrons or electrons traveling at near relativistic velocities are curved in their trajectories, they emit radiation in a direction tangent to their paths as a result of the centripetal acceleration imposed by applied mag-

netic fields. (Storage rings can be used to accelerate either positrons or electrons. In this section “electron” is used to mean either positive or negative electrons.) By application of an rf potential, a synchrotron accelerates electrons around a circular path. The electrons are held to the fixed path by application of a time-varying magnetic field. First described in 1944 by Ivanenko and Pomeranchuk¹⁰³, who noted that betatron operation could be halted due to high energy losses by electrons to radiation, synchrotron radiation was first observed experimentally by Elder, Gurewitch, Langmuir and Pollock at GE’s Schenectady Research Laboratory, where a 70-MeV cyclic electron accelerator was in operation^{108,109}. This device, called an electro-synchrotron, gave the radiation its name. (Technically, a synchrotron accelerates charged particles to high energies for a short time span, whereas a storage ring maintains a beam of charged particles circulating for hours or days, but radiation emitted from storage rings has also come to be known as “synchrotron radiation”.)

From the 1940’s through most of the 1970’s, large synchrotrons were built for high-energy physics research, for example as electron-positron colliders, and scientists interested in exploiting the unique properties of the radiation produced were relegated to the role of “parasitic users”. A 1965 National Academy of Sciences report on uses of synchrotron radiation prompted Ednor Rowe and Fred Mills to convert the 240-MeV storage ring Tantalus, at the Synchrotron Radiation Center (SRC) at the University of Wisconsin in Madison, into the first dedicated synchrotron light source, coming on-line in 1968. By the late ‘70’s, the broad array of applications for synchrotron radiation had assumed sufficient importance to merit the design and construction of storage rings, like the 1-GeV Aladdin at the Wisconsin SRC, dedicated to beam production. Since then, important light sources including the Photon Factory in Tsukuba and Spring-8 in Nishi-Harima, Japan, the National Synchrotron Light Source (NSLS) at Brookhaven National Laboratory on Long Island, the European Synchrotron Radiation Facility (ESRF) in Grenoble, the Advanced Light Source in Berkeley and the Advanced Photon Source at Argonne, have come on-line and fostered rapid progress in synchrotron radiation science by thousands of facility and visiting scientists. Smaller, “compact synchrotron” sources, costing a few instead of hundreds of millions of dollars, are now being routinely delivered for X-ray lithography^{104,110–112}, and can also be used for imaging and other research.

As shown in Figure 1.19⁹⁹, a storage ring consists of an evacuated pipe through which the electrons are made to orbit by means of two basic types of magnet which comprise the “magnet lattice” of the ring. Focusing sextupole and quadrupole magnets act as lenses, confining the electrons to a tight pencil beam by application of a nonuniform magnetic field, whereas bending magnets usually deflect electrons in their trajectory by application of a uniform magnetic field perpendicular to the electrons’ trajectory. The storage ring consists of curved sections of pipe, around which the bending magnets are arranged, and straight sections, capable of accommodating insertion devices (wiggler and undulator in Figure 1.19, see Section 1.2.3.2), which connect the circular bending arcs. Beamlines are straight sections of evacuated pipe emer-

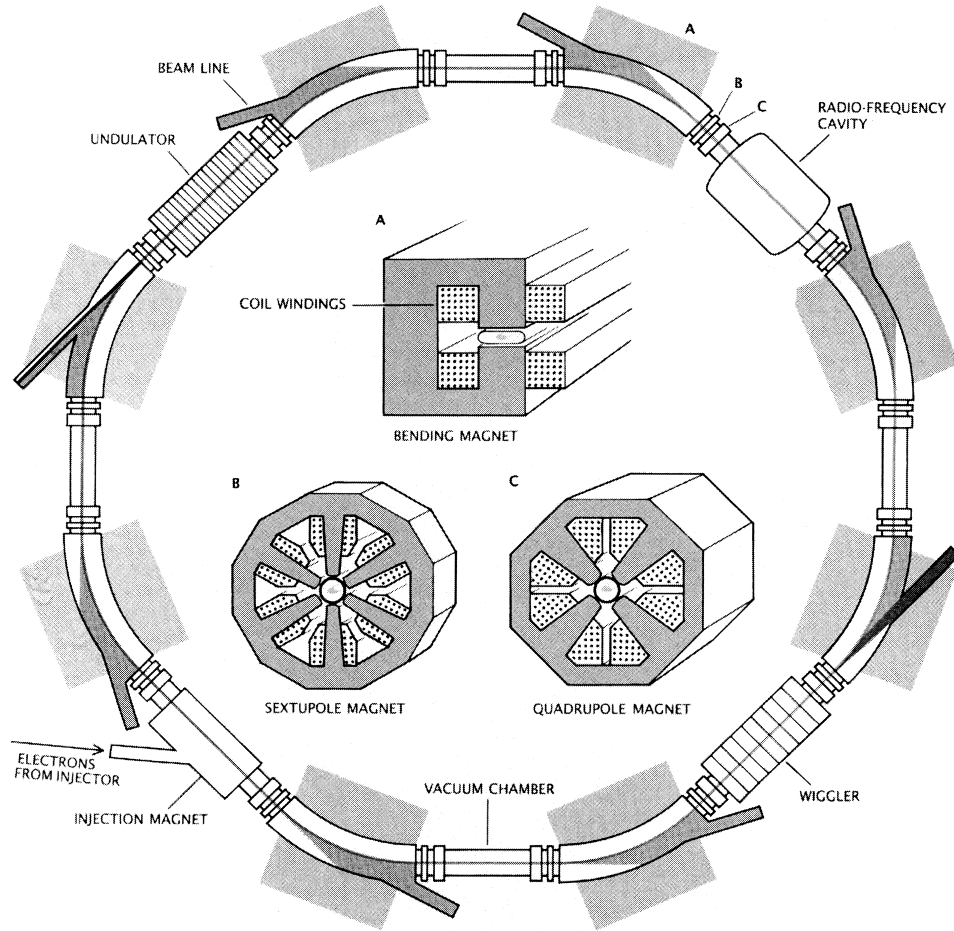


Figure 1.19. Schematic illustrating the important components of a synchrotron light source. (Reprinted with permission from Winick, 1987⁹⁹.)

ging tangentially from the storage ring, which serve as conduits to channel radiation from the electrons to experiment stations arranged around the ring. A large synchrotron with kilometer-order circumference can accommodate tens of beamlines. The beams exit through vacuum-tight, radiolucent windows and are generally incident upon a variety of optical elements which divert the radiation and tailor its properties for particular experiments. Crystal (focusing and non-focusing) monochromators, grazing-incidence and multilayer mirrors, diffraction gratings and zone plates are common examples of synchrotron radiation optical elements^{113–115}.

For the nonrelativistic case ($\beta = v/c \ll 1$, where v is particle velocity and c is the speed of light), the power P radiated by an accelerating particle of charge e was given by Larmor as^{104,116,117}:

$$P = \frac{2e^2}{3c^3} \left(\frac{dv}{dt} \right)^2 = \frac{2e^2}{3m^2 c^3} \left(\frac{dp}{dt} \right)^2, \quad (1.24)$$

where p is the charged particle's momentum. For the particular case of an electron traversing a circular orbit of radius R with constant velocity:

$$P = \frac{2e^2 v^4}{3c^3 R^2}. \quad (1.25)$$

Under these conditions, the radiation emission is in a dipole pattern, with the maximum intensity in a plane perpendicular to the orbit plane as shown in Figure 1.20⁹⁹, top panel.

In the relativistic case ($\beta \approx 1$), the radiated power is:

$$P = \frac{2e^2 c}{3R^2} \beta^4 \left(\frac{E}{mc^2} \right)^4. \quad (1.26)$$

The ratio of the total to the rest energy of the particle, E/mc^2 , is denoted by γ and, for an electron, is equal to $1957E$, where E is in GeV. It can be seen that the radiated power for a proton would be about 2000^4 , or 10^{13} , less than for an electron, which explains why electrons and positrons are used in storage rings, and protons are not. In the relativistic case, the radiation emission pattern is markedly peaked in the forward direction of electron motion (tangent to the orbital trajectory) as shown in Figure 1.20, second panel.

The energy lost by an electron in the course of a single orbit is:

$$\Delta E = \frac{4\pi e^2 \beta^3 \gamma^4}{3R}, \quad (1.27)$$

which, in practical units, amounts to:

$$\Delta E = \frac{88.47E^4}{R}, \text{ and } P = \frac{88.47E^4 I}{R} = 26.54BE^3 I, \text{ since } R = \frac{3.33E}{B}, \quad (1.28)$$

where ΔE is in keV, E is the accelerator energy in GeV, R is the storage ring radius in meters, P is the radiated power in kilowatts, I is the beam current in amps, and B is the field strength in Tesla ($1 T = 10^4$ Gauss). Considering modest ring parameters like 1 GeV, 500 mA, and 1 T, the enormity of the power radiated from synchrotrons becomes evident (the Spring-8 is an 8-GeV facility). Appropriate adjustments to the foregoing equation provide the power available per unit horizontal angle. The energy lost to radiation has to be replaced if the particles are to be kept in orbit, which is the function of rf cavities inserted into the storage ring (Figure 1.19).

The instantaneous power radiated per unit wavelength λ , and per unit (vertical angle ψ) radian is:

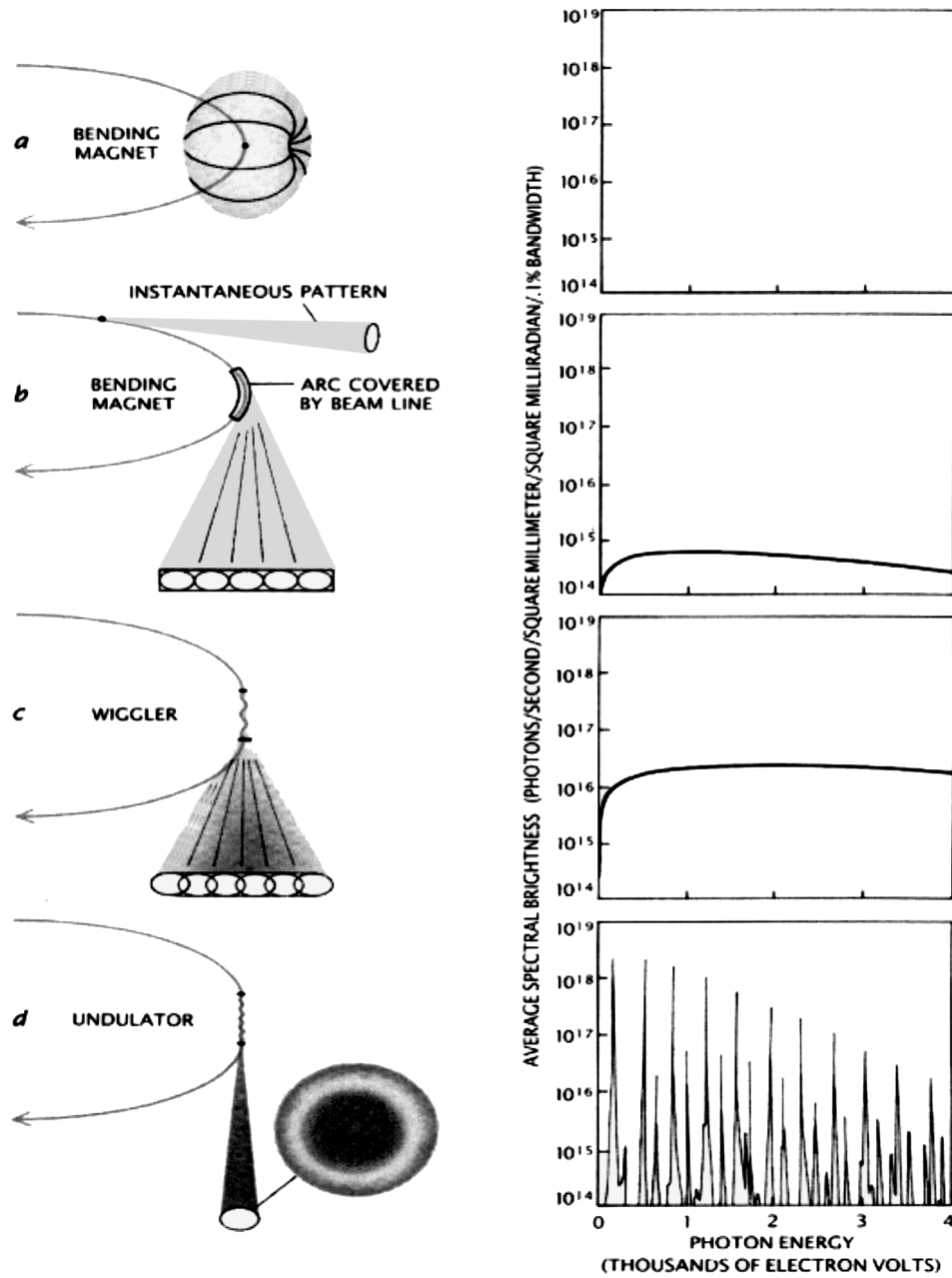


Figure 1.20. Emission envelopes and spectra for various synchrotron components. (Reprinted with permission from Winick, 1987⁹⁹.)

$$P(\lambda, \psi, t) = (2.72 \times 10^{-9}) \frac{e^2 c}{R^3} \left(\frac{\lambda_c}{\lambda} \right)^4 \gamma^8 [1 + (\gamma\psi)^2]^2 \left[K_{2/3}^2(\xi) + \frac{(\gamma\psi)^2}{1 + (\gamma\psi)^2} K_{1/3}^2(\xi) \right] \frac{J}{\text{sec} \cdot \text{rad} \cdot \text{cm}}, \quad (1.29)$$

where $\xi = \left(\frac{\lambda_c}{2\lambda} \right) [1 + (\gamma\psi)^2]^{\frac{3}{2}}$, $K_{1/3}$ and $K_{2/3}$ are modified Bessel functions of the second kind, and λ_c is the critical wavelength:

$$\lambda_c = \frac{4\pi R}{3\gamma^3}, \quad (1.30)$$

or the critical energy is:

$$\varepsilon_c = \frac{3\hbar c \gamma^3}{2R}. \quad (1.31)$$

In practical units:

$$\lambda_c = \frac{5.59 R}{E^3} = \frac{18.64}{BE^2} \text{ and } \varepsilon_c = \frac{2.218 E^3}{R} = 0.67 E^2 B, \quad (1.32)$$

where λ_c is in Ångstroms and ε_c is in keV. Half the total power is radiated at energies above, and half at energies below, the critical energy. In a typical first-generation 1-GeV storage ring with 1-T bending magnets, the critical energy is 0.665 keV. High-field insertion devices, such as wigglers described later, are used to raise the critical energy to considerably higher levels. Since the critical energy varies with γ^3 , storage rings operating at higher accelerating energies (up to 8 GeV) also produce much higher-energy radiation, even from bending magnets: well into the diagnostic energy range (10 to 100+ keV).

Integrated over all emission angles, the radiated power spectral distribution is:

$$P(\lambda, t) = (9.87 \times 10^{-9}) \frac{e^2 c}{R^3} \left(\frac{\lambda_c}{\lambda} \right)^3 \gamma^7 \int_{\lambda_c/\lambda}^{\infty} K_{2/3}(\xi) d\xi \frac{J}{\text{sec} \cdot \text{cm}}, \quad (1.33)$$

while integrated over all energies (wavelengths), the radiated power angular distribution is:

$$P(\psi, t) = (4.375 \times 10^{-8}) \frac{e^2 c}{R^2} \gamma^5 [1 + (\gamma\psi)^2]^{-\frac{5}{2}} \left[1 + \frac{5}{7} \frac{(\gamma\psi)^2}{1 + (\gamma\psi)^2} \right] \frac{J}{\text{sec} \cdot \text{rad}}. \quad (1.34)$$

Winick¹¹⁶ reproduces a number of useful equations for distribution functions originally derived by Green¹¹⁸. Particularly handy for calculating the available flux in a given spectral band are the notations:

$$G_0(y) = \int_y^\infty K_{5/2}(\xi) d\xi, \quad (1.35)$$

$$G_i(y) = y^i G_0(y), \quad (1.36)$$

and the equation:

$$N_k(\lambda) = 1.256 \times 10^{10} k \gamma G_i(y) \frac{\text{photons}}{(k\gamma) \cdot \text{sec} \cdot \text{mA} \cdot (\text{mrad}\theta)}, \quad \text{for all } \psi, \quad (1.37)$$

$$\text{where } y = \frac{\lambda_c}{\lambda} = \frac{E}{E_c},$$

which gives the flux, per second, per mA, per mrad horizontal angle, integrated over vertical angular emission range ψ and within the fractional bandwidth $k = \Delta\lambda/\lambda$. For example, using these equations and the appropriate table of Bessel functions and integrals, the flux available in a 10% bandwidth at the critical wavelength can be shown to be^{104,116}:

$$N_{0.1}(\lambda_c) = 1.601 \times 10^{12} E \frac{\text{photons}}{\text{sec} \cdot \text{mA} \cdot (\text{mrad}\theta)}, \quad \text{for all } \psi. \quad (1.38)$$

For photon energies corresponding to wavelengths above and below λ_c , the flux, integrated over the vertical angular emission range ψ , can be approximated by:

$$N(\lambda) \approx (9.35 \times 10^{16}) I \left(\frac{R}{\lambda_c} \right)^{3/2} \left(\frac{\Delta\lambda}{\lambda} \right) \frac{\text{photons}}{\text{sec} \cdot \text{mrad}\theta}, \quad \text{for } \lambda \gg \lambda_c, \quad (1.39)$$

$$\text{and by: } N(\lambda) \approx (3.08 \times 10^{16}) I E \left(\frac{\lambda_c}{\lambda} \right)^{1/2} e^{-\lambda_c/\lambda} \left(\frac{\Delta\lambda}{\lambda} \right) \frac{\text{photons}}{\text{sec} \cdot \text{mrad}\theta}, \quad \text{for } \lambda \ll \lambda_c, \quad (1.40)$$

where I is the beam current in amps, R is the ring radius in meters, and E is the beam energy in GeV. The flux peaks at a wavelength about three times λ_c , falls off very rapidly at energies above the critical energy due to the factor $e^{-\lambda_c/\lambda}$, and falls off more slowly at lower energies.

For energies close to the critical energy, the vertical emission angle ψ varies with γ^{-1} and, for accelerating energies in excess of 1 GeV, is less than about 1 mrad. While this remarkable collimation accounts for the extremely high available fluxes, it can cause practical problems with alignment of experimental components, particularly if the beam is unstable and moves around. Sophisticated beam monitoring equipment is therefore essential for synchro-

tron radiation experiments, as is flexibility in experiment station positioning. Beam monitors can be incorporated into closed-loop systems which perturb the electron orbit to keep the beam position stable. At energies other than the critical energy:

$$\psi = \frac{1}{\gamma} \sqrt{\frac{\lambda}{\lambda_c}}, \text{ for } \lambda \gg \lambda_c, \quad (1.41)$$

$$\text{and } \psi = \frac{1}{\gamma^2} \sqrt{\frac{\lambda}{\lambda_c}}, \text{ for } \lambda \ll \lambda_c. \quad (1.42)$$

In general, synchrotron radiation is polarized, with the electric vector parallel to the acceleration vector. In the electron's instantaneous direction of motion, polarization is complete, with the electric vector in the orbital plane. The degree to which the radiation is polarized depends on the emission angle and wavelength: polarization decreases as these increase. Polarization is also decreased due to incoherent betatron oscillations of the many electrons producing the radiation at any instant.

Synchrotron radiation is emitted in very short, high-frequency pulses because electrons are injected into and accelerated by rf cavities around the ring in bunches or buckets¹¹⁶. The frequency of radiation emission pulses depends on the orbital frequency of the electrons and the rf frequency, which must be an integral multiple, or harmonic, of the orbital frequency. Typical rf frequencies are in the 50- to 500-MHz range. For example, if the orbital frequency were 1 MHz, an rf frequency of 300 MHz would represent the 300-th harmonic of the orbital frequency, and a maximum of 300 bunches of electrons could be accelerated if all the buckets were full. The total beam current is directly related to the number of filled buckets. Often, only a few buckets are full: only one in the case of collider experiments, in which case the beam current is very low. The duration of each radiation pulse is usually between a few and a few hundred nanoseconds, but may be in the picosecond range. The pulsed nature of the radiation emission is beneficial for some experiments and detrimental to others.

While the radiation intensity produced by synchrotron sources surpasses that of almost all point sources of X rays, their brightness advantage is far greater still due to the low emittance, or angular divergence, of the beam. Low emittance of the electron beam is a requirement for optimal undulator performance. Beam emittance is a tradeoff between betatron oscillations caused when electrons recoil as a result of emitting radiation in direction transverse to their motion, and the damping action of rf cavities which impart momentum to the electrons only in their direction of motion. The emittance of the electron beam can be controlled by varying the field strength of the focusing quadrupole magnets of the storage ring. For transmission imaging of small objects and for X-ray diffraction the extremely high brightness of synchrotron X-ray beams is an important advantage of these sources. On the other hand, the extremely low beam divergence, particularly in the vertical direction, can be a drawback for transmission imaging and tomography of

larger specimens. For such applications, either the beam must be spread in the vertical direction or in both directions by the use of optics such as curved crystals, or the specimen may be scanned vertically through the beam with the transmitted intensity recorded as a succession of linear projections which are then combined in software to form a two-dimensional image. It is difficult to achieve uniform illumination intensity using beam-spreading optics, which also impose a significant flux penalty.

1.2.3.2 Insertion Devices

The properties of the radiation emitted from storage rings (bending-magnet radiation) can be improved for many biomedical applications by the use of insertion devices. These are electromagnetic devices inserted into the straight sections of the storage ring. There are three types of insertion device commonly used to produce radiation beams with the desired qualities: wavelength shifters, wigglers and undulators. All three types impart to the orbiting electrons or positrons additional motions, or deflections from their circular path. These deflections are produced by the periodic magnetic structure of the device: A periodic, linear array of alternating north-south pairs of magnets are arranged outside the evacuated tube of the storage ring causing the orbital electrons to oscillate in their paths. The accelerations accompanying these perturbations imposed on the circular particle trajectory cause more electromagnetic radiation to be given off. Figure 1.21 shows the brightness emitted by various X-ray sources, including tubes, bending magnets, wigglers and undulators⁹⁹. Vertical magnetic fields cause electron oscillations in the horizontal (orbital) plane. Most insertion devices are of the vertical-field type, since the horizontal acceptance aperture of the beam is larger than the vertical¹¹⁹. The three types of insertion device differ in terms of the spectrum and

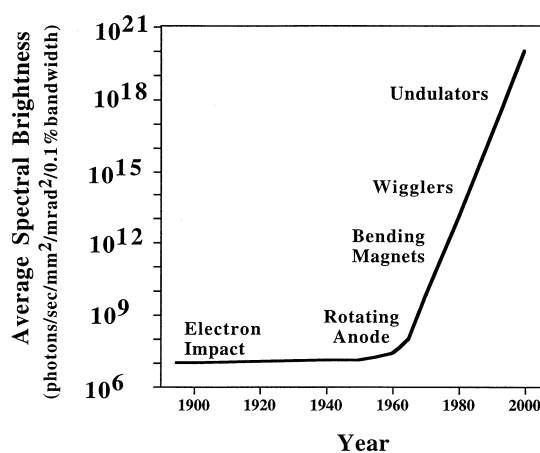


Figure 1.21. Brightness of synchrotrons bending magnets and insertion devices compared to electron-impact sources. (Adapted from Winick, 1987⁹⁹.)

intensity of the radiation they produce. Ideally, all three types of insertion device are designed in such a way that the trajectories of electrons emerging from the device are unaffected: They are the same as they would have been in the absence of the insertion device, and the particles continue on along their approximately circular orbit in the storage ring. The three types of device exert their various effects on the emitted spectrum according to the strength of the imposed magnetic fields and the number of poles or pairs of magnets.

The simplest type of insertion device, the wavelength shifter, has three poles: a strong central pole and entrance and exit poles with half the field strength and reverse polarity of the central pole. (A wavelength shifter is, in fact, just the simplest possible wiggler.) The sum of the fields in the longitudinal orbital direction is zero, with the peripheral poles serving to compensate for the deflection of the strong central pole, allowing the net electron trajectory to remain unaffected. The spectrum produced by a wavelength shifter is qualitatively very similar to that of a bending magnet with a field strength equal to the central pole. Since the field of a wavelength shifter can be made much higher than that of large-radius bending magnets, the main effect of a wavelength shifter is to up-shift the emitted energy spectrum.

Wigglers and undulators are the most common insertion devices. Wigglers^{119–122} have a relatively smaller number of relatively higher-field poles compared to undulators, and therefore cause a smaller number of larger deflections in the electrons' trajectories. The spectrum emitted by a wiggler or undulator depends on the amount of deflection and on the ratio of the deflection angle α to the radiation cone opening angle $1/\gamma$, as shown in Figure 1.22¹⁰⁴. This ratio is called the deflection parameter, $k = \alpha\gamma$. In a wiggler, the deflection angle is large compared to the radiation emission angle, and the emitted spectrum is similar to that from a bending magnet of equivalent field strength, but with much higher flux as shown in Figure 1.20, third panel. Higher wiggler field strengths may be used to extend the range of available

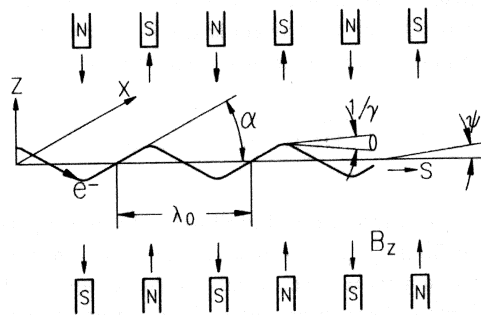


Figure 1.22. Electron trajectory through a multipole magnet. Definitions of the deflection angle α and the radiation emission cone opening angle $1/\gamma$. (Reprinted with permission from Wehner¹⁰⁴.)

photon energies into the tens of keV. The factor by which the flux provided by a wiggler is increased relative to a (large-radius) bending magnet of comparable field strength is proportional to the number of poles in the wiggler. Undulators generally provide high-flux radiation in the UV or soft-X-ray spectral region^{123–126}. An undulator produces a large number of small oscillations in the electrons' trajectories. The deflection angle is small compared to the emission angle (or of the same order), and the flux gain compared to bending magnets is proportional to the square of the number of poles. Undulator radiation from multiple electrons can constructively or destructively interfere, producing an energy spectrum characterized by a large number of narrow-band peaks as shown in Figure 1.20, bottom panel. The gap between the poles may be varied to tune the spectral peaks to the desired energy.

1.2.3.3 Applications of Synchrotron Sources

Synchrotron X-ray sources have been exploited for a broad range of applications in biomedical research including X-ray microscopy^{125,127–147}, microtomography^{148–162}, protein crystallography^{94,95,163–171}, extended X-ray absorption fine structure analysis (EXAFS)^{95,172}, holography^{173–178}, angiography^{168,179–200} and mammography^{35,37,38,201}. The tunable monochromaticity and high flux available were the motivations to utilize synchrotron radiation for almost all of these applications. Coherence and polarizability of the radiation were essential for others.

High flux at low energy is particularly important for X-ray microscopy of thin specimens, one of the earliest applications of synchrotron radiation to biomedical research^{127–129,202–206}. X-ray microscopy in the “water window” presents attractive possibilities for studies of biological specimens with nanometer resolution. In this spectral region, between the oxygen K-edge at about 23 Å and the carbon K-edge at 44 Å, water, which makes up the bulk of cellular matter, is almost transparent and nucleic acids and proteins absorb strongly. This offers the opportunity to image unstained, wet tissues at atmospheric pressure with a radiation which, though lethal, should cause less radiation damage than electron microscopy in the overlapping portion of the resolution regimes of the techniques^{204–206}.

X-ray microscopy can be performed using four basic modes or imaging geometries: contact, scanning, imaging and holographic²⁰⁷. Early studies utilized contact microscopy, in which the specimen is placed in intimate contact with the detector, usually a high-resolution X-ray photoresist of the type used in X-ray lithography^{133,175,202,207–216}. The chemical structure of the resist is altered by absorption of x radiation transmitted through the specimen. After exposure the specimen is removed from the surface and the resist is chemically developed, yielding a relief map in which the height is either proportional to (positive resist) or inversely proportional to (negative resist) X-ray exposure. The theoretical resolution of the resist, usually polymethylmethacrylate (PMMA) or a copolymer thereof, is on the order of ten nanometers for soft X rays, and resolution as high as thirty nanometers has been obtained.

Until recently, the relief map in the developed resist had to be replicated by deposition of a metal or polymer film. After dissolving away the resist, the replica was viewed in the scanning or transmission electron microscope. The necessity to produce a replica contributed to the tedious nature of this technique. With the advent of scanned-probe microscopes in the 1980's, an improved, direct method for viewing the developed resist became available²¹⁷.

Scanning X-ray microscopy is another possibility using synchrotron radiation^{127,131,218–223}. In this geometry, the beam is focused to a small pencil or point, using a zone plate or reflective optical element (usually augmented by an aperture upstream from the sample), the specimen is scanned through the X-ray beam in a raster or boustrophedonic manner, and the image acquired point-by-point by a single-element detector. The diameter of the beam at the specimen and the accuracy of the scanning mechanism determine the spatial resolution, which may be on the order of nanometers, the highest obtained by any mode of X-ray imaging. Though the apparatus is rather expensive and the possibility of “flash” or realtime imaging is precluded by long imaging times, scanning has been the most productive mode of synchrotron X-ray microscopy due to the high spatial resolution and relatively modest optical requirements.

Imaging microscopy utilizes a condenser zone plate to simultaneously illuminate the entire area of the thin specimen to be imaged and a zone plate objective to form the transmitted image on the detector. Although the state of the art is advancing, it remains challenging to fabricate the zone plates which limit the performance of this method^{142,144,224–227}. The resolution attainable is roughly equal to the width of the outermost annular ring, generally limited to several tens of nanometers.

X-ray holography has long been proposed as a possible method to obtain ultra-high-resolution, three-dimensional information from biological objects^{173–178,228–230}, but has remained an elusive goal. This is in part due to the lack of adequate technology to present the image formed by the recombined reference and sample beams to the human viewer in an acceptable or even useful way. Until practical X-ray lasers in the appropriate wavelength range are developed (see Section 1.2.5), coherent beams from undulators present the best candidate sources for holographic application.

Synchrotron X-ray microtomography has been applied or suggested for application to a number of biological investigations^{148–150,152,154,158,160,162,231–236}. Compared to microscopy of thin sections, microtomography of real specimens provides more modest spatial resolution in the tens of microns range, though the possibility of higher spatial resolution has been demonstrated on test objects²³⁷. The most impressive biological results to date have been obtained on cancellous bone¹⁶¹. One of the problems with synchrotrons as sources for 3D microtomography is the almost planar nature of the beam, necessitating vertical translation of the specimen through the beam and confining volumetric imaging to the stacking of serially-reconstructed slices in software. There has recently been an interesting demonstration of the feasi-

bility of phase contrast²³⁸ synchrotron X-ray tomography^{160,162,239} which exploits the larger differential in “phase retardation cross sections” (vs. attenuation cross sections) of various healthy and malignant soft tissues and the partial coherence of synchrotron radiation.

In the 1980's, there was a flurry of activity in synchrotron coronary angiography, which was even advocated as a mass-screening technique^{179–184, 186–188,190,191,240}. It was the markedly-improved signal-to-noise ratio, relative to broad-band illumination, at a given (preferably low) dose afforded by the tunable monochromatic beam applied to iodine-enhanced subtraction angiography that prompted these efforts. It is unlikely that a screening method requiring such elaborate instrumentation as synchrotron sources will ever become economically viable, but some recent studies have shown excellent potential for similar, much higher resolution, techniques in a basic-research context^{198,199}. With the current emphasis on women's health issues in general and breast cancer detection in particular, it has been suggested that synchrotron X-ray sources be applied to mammography^{37,38,201}. Again, it seems unlikely that synchrotron mammography will become accessible to the general population, but characterization of the X-ray absorption properties of benign and diseased breast tissues of various types and precancerous and malignant stages could be a valuable contribution to the practice of X-ray mammographic cancer screening.

1.2.4 Plasma X-ray Sources

Plasmas, which have been referred to as the fourth state of matter, are described by the physics of highly-ionized matter. While a plasma is a collection of electrons, ions, neutral atoms and molecules which, taken as a whole, is electrically neutral, the degree of ionization is very high¹¹⁵. The interparticle spacing within a plasma is relatively high, and the particles' motion is dominated by interactions of their electric and magnetic fields. High-temperature plasmas can emit both Bremsstrahlung and characteristic line radiation. Typically, the radiation is emitted in short bursts, ranging from microseconds for some glow-discharge plasmas to femtoseconds for modern laser-produced sources. Plasmas are characterized by the temperature, density, and oscillation frequency of their electrons, which dominate in the X-ray emission processes. A diagram showing the ranges of these parameters for various plasmas is shown in Figure 1.23¹¹⁵. The parameter ranges characteristic of pinch and laser plasmas useful for X-ray production fall in the upper right corner of the diagram.

There are a number of methods to produce plasmas energetic enough to emit hard and soft X rays, including focusing an electron or ion beam onto a plasma^{241,242}, producing a micropinch of high-Z electrode material by vacuum spark discharge²⁴³, imploding thin wire arrays by passage of tremendous electrical currents²⁴⁴, tokamaks^{245,246}, and focusing an intense optical laser

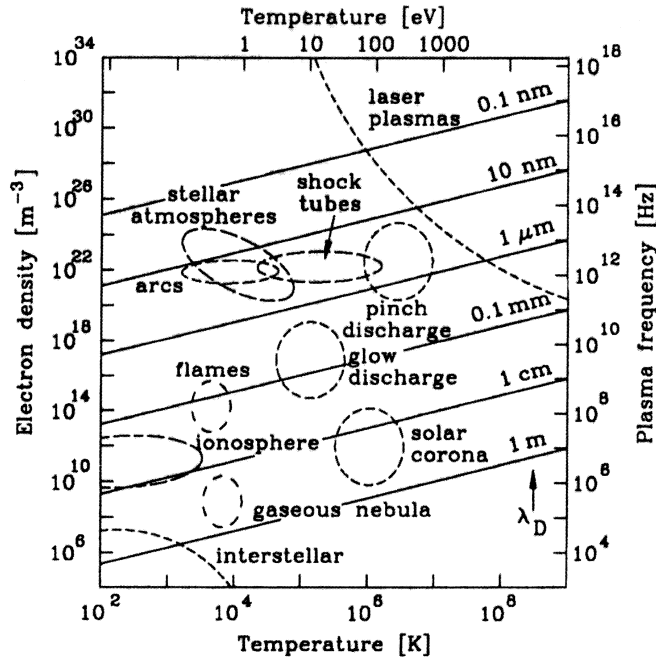


Figure 1.23. Electron density, temperature and oscillation frequency for various types of plasma. (Reprinted with permission from Michette and Buckley¹¹⁵.)

pulse onto a solid or liquid target. Z-pinch and laser-produced plasmas (LPP's) are the most popular for laboratory production of X rays for imaging, spectroscopy and lithography.

This section briefly describes gas and laser-produced plasma X-ray sources. Both types have found increasing application in microscopy and imaging in recent years, and the laser-produced variety seems to hold realistic promise for offering a viable, high-flux, compact alternative to the electron-impact X-ray source for clinical use^{247,248}. While electron-impact sources have evolved to a highly-mature technological state in which their properties and emission spectra are quite well understood, this is not true of plasma sources. Efforts to understand the basic physics describing the emission processes, to improve the efficiency of energy conversion and reliability, and to characterize the time course and spectral content of the complex emissions, especially from laser-produced plasmas, constitute an area of intensely feverish research in the 1990's. This introduction is intended to convey the basic principles on which these devices operate, to present a few of the imaging applications to which the sources have been applied, and to serve as a gateway into the vast literature documenting the work and progress in the field. Detailed discussion, derivations and equations relevant to the physics of plasma X-ray sources are available in a number of sources^{115,249-264}.

1.2.4.1 Gas Plasma Sources

In a gas jet plasma or Z-pinch source, a high current is rapidly passed through a cylindrical annular gas jet, for example by discharging a bank of capacitors^{265–268}. Typically, atoms of an inert gas such as argon, krypton or xenon are stripped into a highly-ionized charge state. Nitrogen has also served as the working gas²⁶⁹. The high self-magnetic fields generated by the current confine the plasma and compress it “into a pinch”, causing implosion of the cylinder and producing the high electron temperatures required for emission of a burst of X rays. Typically, a few hundred joules of X-ray energy are emitted in a 50- to several-hundred-nanosecond FWHM pulse^{265, 266}, though the Proto-II diode system at Sandia has been reported to produce many kilojoules of radiation²⁶⁷ and even more energetic plasmas undergoing development at Sandia threaten to rival the National Ignition Facility²⁴⁴. Several tens of millijoules per square cm may be available at the specimen surface.

The spectrum consists of characteristic lines superimposed on a white, Bremsstrahlung background, usually spanning the VUV to soft-X-ray range (20 to several hundred angstrom wavelengths), but possibly extending down into the sub-angstrom range²⁶⁷. If the wavelengths above 44 Å are not desired, they may be attenuated, for example by a thin aluminum layer at the specimen or by another gas puffed into the beamline. For water-window microscopy, carbon dioxide or nitrogen used as the working gas produce intense emission lines in the 33- to 41-Å and 24- to 29-Å ranges, respectively. It is possible to use one “discharge gas”, such as argon or helium, optimized for initiation of plasma discharge by the high current, and a separate “emitting gas”, such as nitrogen or carbon dioxide, optimized with respect to its spectral emission properties²⁷⁰. In X-ray microscopes which use zone plate objectives, $\Delta\lambda/\lambda$ must be very small for efficient focusing, and narrow spectral lines are isolated from the continuum with condenser zone plate/monochromator combinations^{269,271–273}. A commercial z-pinch source was manufactured in the 1980's, and incorporated into several X-ray microscopes for biological research^{211,212}.

1.2.4.2 Laser-produced Plasma Sources

When an optical laser beam is focused onto the surface of a solid target, plasma formation can occur if the breakdown threshold is exceeded. The breakdown threshold, defined as the lowest optical power density required to ionize atoms in the target medium and produce a plasma, varies for different targets, but is easily exceeded with many modern lasers. If the focused beam intensity is in excess of 10^{16} W/cm², formation of a highly-ionized, solid-density plasma results. Rapid recombination and other processes in the high-temperature plasma give rise to emissions spanning the spectrum from visible to hard X-ray. High-intensity irradiation of target atoms ionizes them by multiphoton excitation: Many photons are absorbed simultaneously allowing photons of energy much lower than electrons' binding energy to strip elec-

trons from their atomic orbits. Irradiation of a target atom with intense laser light causes it to develop a time-dependent dipole moment and produce emission of photons at odd multiples of the laser light frequency²⁷⁴. This generation of odd harmonics of the incident frequency is called optical harmonic generation. Shortening the pulse length and increasing the intensity has made possible the observation of harmonics up to the 109th for 811-nm irradiation and the 143rd for 1053-nm laser light²⁵¹. These harmonic emissions and other line emissions resulting from electron transitions (bound-bound transitions in ions) are superimposed on the continuum emission from radiative recombination (free-bound transitions of electrons and ions) and Bremsstrahlung (free-free transitions of electrons)²⁵². The total conversion efficiency of light to X-ray energy is less than 1% at 10^{16} W/cm², but could exceed 10%²⁵² at intensities over 10^{18} W/cm². For low-Z targets like carbon, mylar tape, or liquid droplets the plasma consists mostly of hydrogen-like and helium-like ions giving a relatively small continuum background and strong K-shell emission in the water window^{275–277}. For medium-Z targets, the continuum contribution is increased overlaid with a denser line spectrum from L-shell emission from neon-like and other ions. High-Z targets produce the largest continuum.

Since the invention of the laser in 1960, optical power output has increased by twelve orders of magnitude²⁷⁸. Q-switching in the 1960's followed by mode locking around 1970 increased the available power to about 10^6 and 10^9 watts, respectively, providing intensities (also called power densities or focused irradiance) of 10^{12} and 10^{16} watts/cm². But well into the 1980's, rather large and very expensive laser systems, like the VULCAN and SPRITE at Rutherford Appleton Labs^{275,279–284}, the GDL at Rochester's Laboratory for Laser Energetics²⁸⁵, or the NOVA at Lawrence Livermore^{286,287}, were required to obtain the very high intensities in what were relatively large focal spots (100 to 300 microns compared to the 40 to 100 microns which are commonplace today) required for production of adequate X-ray flux for single-shot imaging. The invention of chirped-pulse amplification in the late 1980's made feasible relatively-inexpensive (\$100 000 to \$160 000), compact, bench-top terawatt (10^{12} watt; “t³”, or “t-cubed”, for table-top terawatt²⁷⁸) lasers, capable of delivering a joule per pulse in sub-picosecond pulses and providing intensities^{249,251} of 10^{18} to 10^{19} W/cm².

Chirped-pulse amplification achieves this high irradiance in compact devices by shortening the pulse length after amplification, avoiding the non-linear optical responses (Kerr effect) which degrade the beam in almost all high-gain, broadband materials at powers in the terawatt range²⁵¹. An ultra-short (femtosecond), low-power (nanojoule) pulse is first chirped, or lengthened by factors as large as 10^4 , by one optical grating, amplified by factors between 10^6 and 10^{11} while in the dispersed, low-power state, then condensed to its original duration again, or reconstructed, by a second optical grating. A chirped pulse possesses a time-dependent frequency because the pulse stretcher has a frequency-dependent phase function. The pulse compressor must then possess the conjugate phase function to perfectly reconstruct the

pulse. Probably the most popular amplification systems are Nd:glass^{288,289} and Ti:sapphire^{262–264,290–294}. A Ti:sapphire system can produce pulses under 10 femtoseconds in duration.

There are several advantages to high-power, short pulse systems: hydrodynamic motion in a plasma is almost negligible for a 100 fs pulse; very high energy densities can be achieved; the electric field due to the light pulse is many times stronger than the Coulomb field binding even the innermost electrons of high-Z elements; and very high oscillatory energies (also called quiver or ponderomotive energy) are achieved by the stripped free electrons. These attributes of short pulses from t-cubed lasers make them attractive for plasma generation in LPP X-ray sources. The high energy densities result in high output X-ray flux which scales as laser intensity raised to powers between 1.9 and 2.8, depending on the target material²⁹⁵. The highly-ionizing nature of the irradiation broadens the array of suitable target materials and enhances plasma electron temperature and X-ray output. The high quiver energies of the free electrons is accompanied by the emission of harder X rays. This is because the quiver energy is rapidly thermalized after short-pulse irradiation, producing quasi-Maxwellian plasmas with many hot electrons which emit high-energy X rays (and electrons): MeV X rays are emitted²⁵¹ from plasmas generated by irradiation with 10^{18} W/cm². Intensities in the 10^{14} to 10^{17} watts/cm² range are associated with high-brightness, soft-X-ray sources (low fluxes of hard X rays are also produced at these intensities), whereas intensities approaching the petawatt range, on the order of 10^{17} to 10^{20} watts/cm² are required to produce hard X-ray beams with flux high enough to be useful for clinical imaging. The properties of the plasma and of the X-ray emission can be controlled in large measure by the intensity, polarization, and wavelength of the incident laser pulse and by choice of target material^{254–257,278,296}. It has also been demonstrated that X-ray emission from solid targets can be enhanced by use of a relatively long, less-intense prepulse before the high-intensity main pulse (e.g. 30- to 200-ps, 10^{13} to 10^{14} W/cm² prepulse followed by 1-ps main pulse)^{254,255,297–300}. In this case, the main laser pulse is interacting not with a solid but with a pre-plasma. The prepulse may be either of the same, or a different wavelength than the main pulse.

A slight variant on the LPP X-ray source theme, which apparently has the potential to produce even brighter beams of coherent, multi-keV radiation, is being proposed and investigated by Rhodes and colleagues^{301–303}. “Hollow atoms”, of xenon, for example, are produced when clusters of atoms from a pulsed supersonic gas jet are exposed to 300-fs pulses of UV laser light at 10^{18} W/cm². The quiver energy of stripped, outer-shell electrons is transferred through energetic collisions to inner-shell electrons, ejecting them from the atom. The orbit-filling cascade results in intense X-ray emission. One proposed use for the radiation is Fourier transform holographic microimaging of biological specimens¹⁷⁸.

The radiation in the 1- to 10-keV range from LPP’s, though in general incoherent, can be orders of magnitude brighter than that available from synchrotron sources²⁷⁸. The source size, though larger than the best microfocal elec-

tron-impact tubes and larger than synchrotron beams at the source, is typically on the order of 40 to 100 microns, allowing for high-magnification imaging. Each pulse from an LPP is much longer than an individual pulse from a synchrotron; the repetition rate of LPP's is far lower than that of synchrotrons²⁵¹, ranging from about 10^{-3} to 10^3 Hz. Thus, the peak power of LPP X-ray sources is higher than synchrotrons and much higher than conventional tubes, but the average power is much lower. Efforts are underway to increase the repetition rate of chirped-pulse amplified lasers, which is often only a few Hz or less, since imaging of thick objects, and certainly clinical imaging, currently would take hundreds or thousands of pulses^{247,248}. For 100-fs pulses at a typical repetition rate of 10 Hz, a continuous imaging time of minutes would result in a true exposure time of less than a nanosecond. For this reason, the best argument for LPP X-ray imaging that can be made at present is for small specimens which can be imaged in a single shot.

1.2.4.3 Applications of Plasma Sources

Intensive research on short-pulse LPP's is underway, partly because of their potential as X-ray sources and as the gain medium for X-ray lasers, but mostly because of their potential use for indirect approaches to inertial confinement fusion^{251,252,286,298}. LPP's as X-ray sources have been used for time-resolved absorption experiments and X-ray diffraction, for X-ray lithography at the 13- to 14-nm wavelength for which high-efficiency multilayer reflective optics are available^{265,304-316}, and for X-ray microscopy^{132,143,211,212,217,266,275,289,304,317-330}. Compared to synchrotron sources, LPP X-ray sources have the advantages of low cost, not requiring an ultra-high vacuum, emitting very high brightness beams in short bursts, high spatial stability and reproducibility, and small source size (smaller than z-pinch and plasma focus sources).

The simplest arrangement for X-ray imaging with plasma sources is shown in Figure 1.24³³¹. A short focal-length lens focuses the laser beam through a vacuum window onto a solid (or tape, or droplet) target mounted in the imaging chamber. X rays are emitted into 2π , passing through the vacuum to the specimen and film. The minimum source-to-specimen distance, which is decreased in the interest of increasing the flux on the sample, is limited by physical constraints to at least a few millimeters³²¹. Another problem with the arrangement, and with LPP sources in general, is the production of debris, including "hot rocks" up to several microns in size, which can be ablated from the target surface. This leads to fouling of the specimen chamber as well as contamination of the image. Often, silicon nitride windows (Si_3N_4) are placed in front of the specimen to protect it from debris and allow it to be kept at atmospheric pressure. An environmental sample cell for resist-based imaging is shown in Figure 1.25³³².

Normal-incidence, reflective optical systems have been proposed and implemented to shield the specimen from debris and to increase the flux on the specimen/detector assembly. Examples are the multilayer spherical mirror

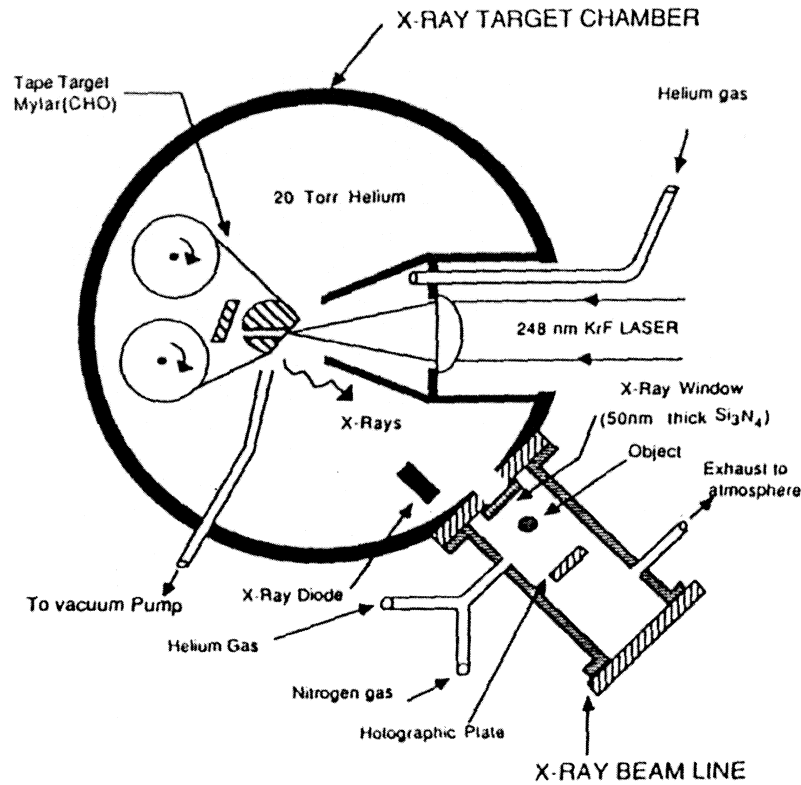


Figure 1.24. X-ray microscope based on a laser-produced plasma source. (Reprinted with permission from Turcu *et al.*, *J. Appl. Phys.* 73, 8081 (1993)³³¹. Copyright 1993 American Institute of Physics.)

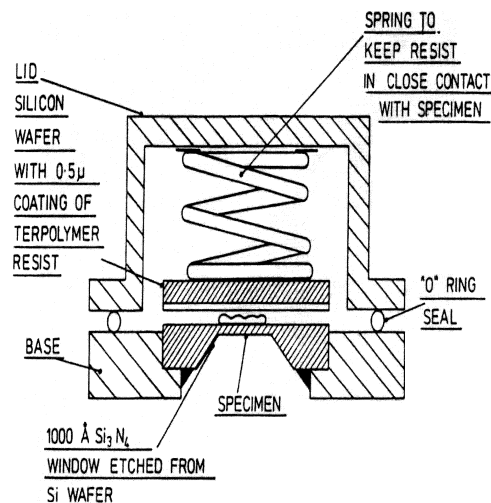


Figure 1.25. An environmental sample cell for resist-based X-ray microscopy using a laser-produced plasma source. (Reprinted with permission from Rosser *et al.*³³².)

and the Schwarzschild objective, used in conjunction with a thin, transmissive target, shown in Figure 1.26³²². Historically, the problem with optics has been low efficiency, though reflectivities as high as 60% have been reported for multilayer mirrors optimized for particular (multinanometer) spectral bands³³³. Any conceivable optical scheme is likely to suffer from debris deposition, and fast shutters or gas backing pressures are difficult to implement or only partial solutions. The most promising approaches to avoid debris contamination appear to be reducing its production by use of thin targets (e.g. mylar tape^{275,312,319,331}, or metal-doped glass targets³¹⁶) with the specimen and any optical components on the opposite side from the plasma, or using droplet (alcohol or water) targets produced by a vibrating ink-jet nozzle^{315,334} or commercial vibrating orifice droplet generator³³⁵. With droplet targets, the source size can be carefully controlled and exactly known, since it is equal to the droplet dimension for small droplets, and debris deposition is reduced by more than three orders of magnitude compared to thin tape targets.

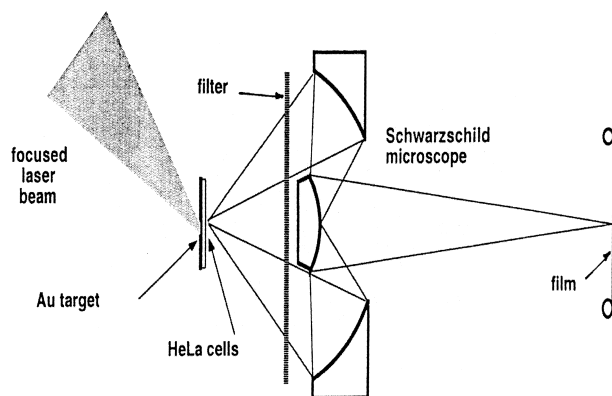


Figure 1.26. Laser-produced plasma based X-ray microscope incorporating Schwartzschild objective for magnification imaging. (Reprinted with permission from Richardson *et al.*³²².)

In 1979, researchers at Rochester's Laboratory for Laser Energetics reported on nanosecond biological X-ray diffraction using an LPP²⁸⁵. They showed diffraction patterns of cholesterol and rat spinal roots. Panessa used a pulsed-plasma source and resists to record contact micrographs of proteoglycans³³⁶ and myosin filaments³³⁷, while Feder *et al.* imaged red blood cells with a z-pinch source as early as 1982²⁶⁵. Widespread attention was focused on the potential for high-resolution X-ray imaging of biological specimens using plasma X-ray sources when Feder and colleagues published micrographs, obtained using a gas jet plasma and photoresist detector, of live human platelets on the cover of *Science* in 1985³¹⁷. Other groups were contemplating the possibility of biological imaging using LPP sources at about the same time^{279,280,318}.

In the 1980's, Michette imaged epidermal hairs, as well as flagellates and human fibroblasts, using very high-energy (30 to 80 joule) pulses from the VULCAN and SPRITE lasers focussed onto mylar tape targets²⁷⁵. More recently, his group has been involved in development of scanning X-ray microscopes using LPP sources. Either the specimen³¹⁹ or the source³²⁰ may be scanned. Scanning permits the use of a single-element silicon diode detector, but incurs other practical problems, particularly when the source is scanned. Rosser, *et al.*, used a 2-J laboratory Nd:glass-amplified laser beam focused onto gold targets to produce water-window radiation for imaging cultured fibroblasts and other objects³⁰⁴. A group at Stanford used an LPP source, consisting of an Nd:YAG focused onto a solid copper target, and the Schwarzschild arrangement of Figure 1.26 to obtain pictures of test patterns in 1989^{338,339}. Artyukov built a similar optical setup and used it with an Nd:glass laser and rhenium target to image mesh standards at micron-order resolution³⁴⁰. Hori-kawa used an Nd:YAG laser, iron-target LPP source, grazing incidence condenser, multilayer Schwarzschild objective, and scintillator/microchannel plate detector to image unstained myofibrils at sub-micron resolution^{329,341}.

Tomie and a team at the Electrotechnical Laboratory in Tsukuba showed detailed images (up to 40-nm resolution) of sea urchin and barnacle sperm, algae, and chinese hamster cells, recorded on resist using water-window LPP source radiation, mostly from yttrium targets^{217,321,330}. They state that the requirement for X-ray intensity increases as the fourth power of resolving power and that a few tens of millijoules per square centimeter are required when the resist detection efficiency is 10%. To approach the practical resolution limit of 30 nm imposed by the resist, a dose of 5×10^5 Gray is required, about 10^5 higher than the threshold for biological damage. If manifestation of morphological damage is to be avoided in the recorded image, the exposure time has to be less than 1 ns, a compelling argument for development of LPP sources. Solem has calculated that 30-ps exposures are required for 10-nm resolution³⁴², the theoretical resolution limit for X-ray photoresists^{205,343}.

Shinohara and Kinjo have imaged human chromosomes using very soft, second-harmonic (527-nm) radiation from gold targets irradiated with 300-ps, 26-joule pulses focused into 100-micron focal spots (10^{15} W/cm²)^{136,289,322,327,344-349}. They estimated that the flux at the specimen (2 cm from the source, protected by a SiN window) was about 1.4×10^{15} photons/cm², with photon energies of 250–1250 eV. This would translate to approximately 0.17 J/cm², in agreement with the exposure requirements calculated by others¹⁷⁵. Stead and colleagues investigated the effects of electron microscopy fixatives on biological materials using X-ray microscopy of plant epidermal hair cells³²⁶. The X-ray images, demonstrating 150-nm resolution on weakly-attenuating carbonaceous material, were acquired on photoresists using a Rutherford Appleton Nd:glass laser and thin-foil gold targets. Resists were read out with scanning and transmission electron and atomic force microscopes. This group had previously demonstrated 50-nm resolution on dense, particulate and diatom structures³⁵⁰.

Although still technically challenging to perform and scant on results, X-ray microscopy with LPP sources appears to hold promise for very high-resolution, one-shot imaging of biological objects. Whether this type of source will evolve to compete in the clinic with rotating-anode, electron-impact tubes^{247,248} depends upon whether the debris-deposition problem can be solved, either by the use of appropriate, efficient optics or innovative target materials and geometries, and whether the repetition rates (and thereby average power output) can be increased to the level required for sub-second total exposure times.

1.2.5 X-ray Lasers and Free Electron Lasers

Most lasers produce bright, coherent, visible or UV light by amplification occurring over multiple passes through a Fabry-Perot reflecting cavity or resonator containing the pumped gain medium³⁵¹. There currently exist no suitable, efficient mirrors for X-ray beams which can be used to produce multiple passes through the gain medium (energetic plasma)³⁵², but because of widespread interest in the desirable properties X-ray laser light would possess for a variety of applications including biological microscopy and holography, research on X-ray lasers has persisted. In fact, efforts to exploit, in a practical and cost-effective way, the various schemes proposed for the production of X-ray lasers have increased since the first demonstrations of X-ray lasing in 1985^{353,354}. Since no suitable X-ray mirrors exist (and even if they did they would likely be destroyed by energy deposition from optical and x-radiation of the proximal plasma gain medium), amplification must be achieved on a single pass of photons through the gain medium, usually a plasma formed by an intense optical laser focused onto a line along which lasing occurs. When gain is achieved in an energetic plasma, the lasing is said to occur by amplification of spontaneous emission or ASE. Until recently, X-ray lasers remained exotic and expensive propositions, primarily because of the requirement for extremely high-intensity visible lasers to produce the plasmas used to pump X-ray lasers. But with the emergence of chirped-pulse amplified^{249,355} and other less expensive optical lasers with intensities in the terawatt to petawatt range, and with the demonstration of X-ray lasing in capillary discharge plasmas^{356,357}, it appears that low-cost, “personal”³⁵⁸ X-ray lasers may soon become a reality³⁵⁹. Partly because of their complexity and partly because the shortest-wavelength lasing demonstrated to date is at the long-wavelength end of the spectrum useful for biological imaging research, a thorough discussion of X-ray lasers is beyond the scope of this chapter. The interested reader should consult other excellent sources^{206,282,283,303,352–354,358,360–386}.

Both of the successful approaches to lasing at X-ray wavelengths use high-power optical lasers to create the high-temperature plasmas required as pump sources. In their most-investigated incarnations, these two alternative methods use electron-collisional recombination pumping³⁵² (also called recombination pumping) with H-like or Li-like ions^{354,358,372,385,387–389}, and

electron-collisional excitation pumping (often called collisional pumping) with Ne-like or Ni-like ions^{353,368,378–382,386}. (Other pumping mechanisms, including photoionization, photoexcitation and charge transfer, have been proposed on theoretical grounds, but have not proven themselves experimentally³⁵².) Although a number of other laboratories are contributing to the rapid developments in the X-ray laser field, perhaps mainly because of their places of discovery these two approaches to X-ray lasing are often identified with groups at Princeton and Lawrence Livermore (LLNL), respectively.

In the recombination scheme, a laser-produced plasma containing highly-stripped ions is the gain medium. After a brief pulse of the optical laser, the plasma is cooled rapidly, undergoing rapid three-body combination and producing population density inversion, a necessary condition for gain. An important advantage of the recombination scheme is that it scales rapidly to shorter wavelengths with increasing plasma ion charge (and therefore target Z), though with decreasing axial extent of the plasma column in which lasing occurs. But it is difficult to obtain and maintain a long, uniform plasma column using recombination pumping. The Princeton group uses a strong magnetic field to confine the plasma column, which helps in this regard. The recombination X-ray laser should exhibit a much higher pumping efficiency than the collisionally-pumped laser, but saturated output has not been approached³⁹⁰. One of the earliest applications of X-ray lasers to biological microscopy involved recombination-type lasers using a 1 kJ CO₂ optical laser to produce lasing at 18 (carbon target) and 4 nm (lead target). The X-ray laser was used to image cervical cancer cells and other specimens on a resist detector³⁸⁸, and it is also proposed to perform biological microscopy at several hundred times magnification with a microscope employing a Schwarzschild objective and CCD-based detector³⁸⁹.

In the collisional excitation scheme for Ne-like selenium, gain is achieved mainly by collisionally exciting ions to the 3p level, setting up a population inversion between the 3p and 3s levels because of very rapid decay from the latter to the ground state. The Ni-like tantalum X-ray laser, which produced the first significant gain at wavelengths below the carbon K-edge, works in a similar way, with population inversion between the 4d and 4p levels. The collisional excitation scheme has the advantage that it is self-replenishing in the sense that the initial state from which pumping occurs and the ground state to which decay occurs after lasing are the same. Also, the lower state is relatively translucent to the laser wavelength allowing plasma column lengths of centimeters. The length of the plasma column over which lasing occurs is important because amplification has to occur in a single pass. The most important parameter with regard to laser output intensity is the gain length (GL), calculated as the product of the gain (cm⁻¹) and the plasma column length. Initial experience with collisional excitation lasers came out of the inertial confinement fusion facilities at LLNL, including the NOVA and Novette lasers. The first demonstrations³⁷⁸ of this scheme involved exploding thin selenium foils using intensities of 7×10^{13} W/cm² focused on 1.8-cm lengths of foil and producing GL of 8 at 206.4 and 209.8 Å, since raised to 16 and

15.2, respectively³⁵⁸. Nickel-like lasers, created by exploding thin tantalum, tungsten, or gold foils, are very similar in principle to their Neon-like, collisional excitation analogs but require less optical laser power at a given X-ray wavelength and have produced the shortest wavelength X-ray lasers to date: 35.6 Å for Ni-like Au³⁷⁸. An excellent summary of the gain lengths achieved at wavelengths between 35.6 and 326 Å is presented by Skinner³⁵⁸. A GL = 7 has been demonstrated for Ni-like tungsten at 43.18 Å, the first lasing inside the water window, and a GL = 8 for Ni-like tantalum at 44.83 Å, just above the carbon K-edge, at a wavelength ideal for biological X-ray holography³⁹¹. The highest possible output power (saturation) is achieved at GL's between about 15 and 20 which, for collisionally-excited lasers, requires about 1 kJ of driver laser energy at X-ray wavelengths around 20 nm, but over 10 kJ in the water window³⁹². It will be necessary to substantially reduce this power requirement, using pre-plasma-forming prepulses or other methods, if tabletop lasers are to be used successfully to drive high-output X-ray lasers.

Da Silva and the group and LLNL have used the NOVA-driven, Ni-like tantalum X-ray laser to image a variety of specimens, including rat sperm nuclei, at 44.83 Å^{379,380,382}. The optical system consisted of a near-normal-incidence spherical WC/C multilayer mirror condenser with 5% efficiency and narrow bandpass at 44.83 Å, a 500-annulus zone-plate with 450-Å outer-zone width as objective lens, and a microchannel plate (MCP) intensified detector. The MCP limited the spatial resolution to over 500 Å, but correlation with TEM and AFM images provided useful information about the chemical content of imaged volumes in the nucleus. These investigators suggest that cheaper, shorter-wavelength, higher-power X-ray lasers, coupled with improved, short-wavelength multilayer mirrors and improved zone plates and detectors, will bring X-ray laser microscopy into broader usage.

Another interesting, if exotic, tunable, high-flux X-ray source currently under investigation utilizes a phenomenon known as Compton backscattering^{39,40,201,393}. When an intense visible or infrared laser beam collides head-on with a near-relativistic electron beam photons interacting with free electrons change their energy and direction to conserve energy and momentum. The group at the Vanderbilt free electron laser (FEL)^{394,395} is proposing to turn the infrared laser light beam produced by the FEL wiggler back on the electron beam so that the two collide head on. Two-micron infrared photons backscattered from 43-MeV electrons in the FEL beam will have a maximum energy of 17.6 keV, in the range thought optimal for breast imaging. The Compton backscattered beam is to be diverted using graphite mosaic optics and focused and collimated with a Kumakhov optic⁷⁶, to produce a monochromatic, parallel beam accessible for clinical imaging. Another group at Duke is proposing a similar FEL-based approach to produce 12.2 MeV photons for gamma-ray spectroscopy and therapy³⁹⁶.

If a short-pulse, infrared laser beam is normally incident on an MeV electron beam, the Thomson scattering process produces what has been called the laser synchrotron X-ray source³⁹⁷. A group at Lawrence Berkeley Laboratory has produced 300 femtosecond pulses of 30 keV x-radiation using

terawatt laser pulses incident at 90° on a relativistic accelerator electron beam³⁹⁸. The energy of the highly-directional X-ray beam can be controlled by varying the energy of the electron and laser beams and the angle at which they interact. Although very low fluxes were produced in the first experiments, the researchers are optimistic that these can be increased to useful levels.

While electron-impact sources still produce most of the X-ray beams used in clinical and even research applications, it appears that new types of source will prove useful in the future, particularly when high average power is not a requirement and short, ultra-intense pulses can be used to advantage.

1.3 Interaction of X rays with Matter

Viewed from the broadest standpoint, electromagnetic waves interact with matter when their particles possess energies corresponding to energy-state differences in atoms or molecules of the medium. For example, if a radio wave has a frequency equal to the precession frequency of nuclear spins aligned in a strong magnetic field, it may couple to the spins and excite some of them from the lower-energy parallel to the antiparallel state, a phenomenon which forms the basis for the nuclear magnetic resonance (NMR) experiment. A microwave may interact with an electron in a strong magnetic field, inducing a change in energy states which can be exploited using electron spin resonance (ESR) methods.

For infrared, visible and UV radiation, one can express the total energy of a multiatomic molecule as³⁹⁹:

$$E = E_{\text{electronic}} + E_{\text{vibrational}} + E_{\text{rotational}}.$$

Rotational energies are about two orders of magnitude lower than vibrational, which are about two orders of magnitude lower than electronic. If a microwave photon has energy corresponding to the difference between rotational states of a molecule, it may excite the molecule to the higher-energy state. Thus, absorption of microwave radiation by a gas can give rise to rotational absorption spectra. A higher-energy infrared photon may induce changes between molecular vibrational states. Visible and UV radiation can excite outer electronic transitions. Molecular absorption spectra from these interactions can be very complex, since each electronic state may be associated with a number of vibrational and rotational states. In all cases in which interactions occur, frequencies in the beam of electromagnetic radiation can be said to resonate with particular energy-state transitions in the interaction medium. These resonance phenomena may give rise to discrete, measurable changes in the transmitted frequency spectrum if instrumentation of adequate sensitivity and energy resolution is available.

Similarly, higher energy photons in the soft- and diagnostic X-ray ranges may interact with and give up energy and momentum to atomic electrons in the absorbing medium. Very high-energy x and gamma rays can undergo interactions with bound electrons, nucleons, and the nuclear fields of absorber atoms. These interactions produce changes in the energy content of the beam, cause the emission of electrons or nucleons, or transiently excite atoms in the interaction medium. Detection of these energy changes, emitted subatomic particles, or photons forms the basis of a number of imaging and spectroscopic techniques from which insight into biological structure and function can be gained. For clarity, a brief summary of the various X-ray energy ranges, names they are often referred to by, and the interactions of most importance in each range are given in Table 1.3^{115,400}.

Table 1.3.

Energy Range (keV)	Common Names	Relevant Interactions
< 0.120	vacuum ultraviolet	absorption, elastic scatter
0.120–0.500	ultrasoft X rays, water-window X rays (.280–.560 keV)	photoelectric absorption coherent scatter
.100–20	soft X rays Grenz rays	photoelectric absorption coherent scatter
20–140	diagnostic X rays gamma rays	Compton scatter photoelectric absorption
120–300	orthovoltage X rays gamma rays	Compton scatter
300–1000	intermediate-energy X rays gamma rays	Compton scatter
>1000	megavoltage X rays therapeutic x and gamma rays	pair production photonuclear reactions Compton scatter

When related to X-ray beam propagation and interactions, the word “attenuation” refers to any process which causes a decrease in the number of photons passing through a unit area perpendicular to the beam’s propagation direction per unit time interval. Attenuation occurs by three primary mechanisms: geometry, scattering and absorption. The decrease due to simple geometry in photon flux from a point source is often called the inverse square law. The photon flux is inversely related to the square of the distance from the source at which the flux measurement is made:

$$\phi_2 = \frac{\phi_1 d_1^2}{d_2^2},$$

where d_1 and d_2 are the distances from the source at which fluxes ϕ_1 and ϕ_2 are measured. For electron-impact and other Lambertian-emitting point sources of X rays, the flux intercepted by the sample may be dramatically increased by placing the sample close to the source. If a large-format detector is placed some (greater) distance away, a magnified image is produced, which improves the detector system's spatial resolution referred to object space. This can be an important advantage for digital detectors which generally have pixel sizes between about 10 microns (for the smallest-pixel CCD sensors) and 100 to 200 microns (for photostimulable phosphor plates and amorphous silicon detector panels). In practice, especially for tomographic applications, these advantages have to be traded off with the problems created by the large cone angle subtended by the specimen when it is imaged in close proximity to the source.

From the standpoint of their physical interactions with matter, there is no distinction between X rays and gamma rays of the same energy: they differ only in their site of origin. Gamma rays are of nuclear and X rays of extra-nuclear origin. X rays are produced by the acceleration of free electrons or other charged particles (Bremsstrahlung) or by bound electron transitions (characteristic radiation), while gamma rays are produced by nuclear transitions. In this section we consider the interaction of X rays with matter. The energy range of primary interest here is between about 10 and 150 keV since clinical diagnostic imaging utilizes photons of these energies. The descriptions of the interactions of diagnostic X rays which follow apply also to the attenuation of the gamma rays used for SPECT and PET imaging as described in Volume 1, Chapter 3.

Interactions of photons in the 100-eV to 10-keV range relevant to X-ray microscopy and holography will be described briefly, but is treated more fully in other texts^{114,115,401}. In these energy regimes, interaction may involve inner and outer orbital electrons. Interactions of higher-energy X rays with matter, which may include nuclear processes, are discussed in Volume 2, Chapter 1.

1.3.1 Indirect versus Direct Ionization

A radiation beam is an agent of energy transfer²⁰. When a beam encounters biological or other matter, it may interact with atoms in the medium and cause changes in the nature of the beam and of the material. Energy transfer processes may include total absorption and various types of scatter, all of which may be of interest for different types of biomedical imaging experiments. It is helpful to divide electromagnetic radiations into different categories. The infrared, visible and UV interactions discussed above were non-ionizing interactions, characteristic of relatively low-energy exchange events: Vibrational and rotational states could be influenced and outer orbital electrons could be excited to higher energy states, but separation of charge was not a possibility.

Ionizing radiations are energetic enough to entirely remove atomic electrons or protons from their atoms^{3,20}. In the case of x radiation, photons in the beam must possess energies higher than the binding energies of the ejected orbital electrons for ionization to occur. Directly ionizing radiation accomplishes the charge separation directly by interaction between the coulomb forces of the involved particles. Directly ionizing particles include electrons, protons, and other heavy charged particles. Indirectly ionizing radiations, including photons and neutrons, are uncharged particles which may partake in interactions which release energetic charged particles such as electrons and protons from atoms in the medium. Photons, which are the indirectly ionizing radiation of broadest interest in biomedical research, eject electrons, and neutrons eject protons, from atoms in the medium. Although the initial ejection of the charged particle occurs by direct interaction with the incident particle, these radiations are still called “indirectly ionizing” because the bulk of the ionization is due to subsequent interactions of the released, energetic charged particle.

The initial interaction with the X-ray photon may result in some scattered radiation and sets in motion a fast electron. This high-speed electron may cause electronic excitations and ionizations, and may break molecular bonds. If an electron interacts with a nucleus, it may produce additional Bremsstrahlung which, along with any scattered radiation, may contribute to additional indirectly ionizing events. So a complex series of interactions may take place before all the photon energy is lost to electronic motions.

The minimum energy required for ionization cannot be precisely fixed, because it differs from molecule to molecule. A photon may be capable of ionizing an atom when it is bound in one molecule, but not when it is bound in another. Some texts give the cutoff energy for ionizing radiation as 12.6 eV, since this is the ionization potential for hydrogen in water, an important constituent of biological tissue. In tissues, photons must have energy greater than about 10 eV to be capable of ionization.

1.3.2 Scattering

X photons can interact with atomic electrons by elastic or inelastic scattering. In the case of elastic scattering, no kinetic energy is given up by the photon to the attenuating medium, while inelastic scattering involves the loss of some of the incident photon's energy. As the name implies, scattered photons are not stopped or completely removed from the (broad) beam, but are caused to deviate from their original, straight-line path from the source, with no loss of energy for elastically scattered photons, or with diminished energy for inelastically scattered photons. Both types of scatter play a role in image formation because the direction and energy of scattered photons depends on the properties of the scattering material as well as the energies of the incident photons.

1.3.2.1 Elastic Scattering

When photons are elastically scattered, no momentum is transferred to the scattering medium and the wavelengths of the incident and scattered photons are equal. It was found shortly after their discovery that X rays could not be efficiently reflected from polished surfaces but instead were scattered in all directions. J.J. Thomson explained this as the result of the classical interaction of the incident electromagnetic wave with individual atomic electrons which, in his approach, can be regarded as free^{1,3,20,115}. In the classical presentation of elastic scattering, valid for photon energies large compared to atomic electrons' binding energies but small compared to $m_0c^2 = 511$ keV, individual atomic electrons are set to oscillating by the force of the sinusoidal electric field of the incident wave. The vibrating charge radiates at a frequency equal to that of the incident beam, causing no decrease in energy. This type of elastic scattering is called Thomson or classical scattering.

When the (diagnostic-energy: $\beta/c \ll 1$) photon wavelength is similar to the diameter of atoms in the attenuating medium, all atomic electrons, including tightly-bound inner-shell electrons, oscillate and reradiate in phase. This elastic scattering by atomic electrons as a group is sometimes referred to as Rayleigh scattering or coherent scattering, since it is a cooperative phenomenon. Since the distinctions between Thomson and Rayleigh scattering theory can be confusing and are of doubtful practical significance, it can be helpful to think of elastic scattering as being due to a coherent scattering process caused by atomic electrons as a group and characterized by a differential cross-section per unit angle given by^{3,20}:

$$\frac{d\sigma_{coh}}{d\Theta} = \frac{r_0^2}{2} (1 + \cos^2 \Theta) [F(x, Z)]^2 2\pi \sin \Theta, \quad (1.43)$$

where the momentum transfer variable $x = \frac{\sin \Theta / 2}{\lambda}$.

This equation gives the fraction of the incident energy scattered into the cone between angle Θ and $\Theta + d\Theta$ which subtends the solid angle:

$$d\Omega = 2\pi \sin \Theta d\Theta. \quad (1.44)$$

The expression:

$$\frac{d\sigma_0}{d\Omega} = \frac{r_0^2}{2} (1 + \cos^2 \Theta) \quad (1.45)$$

is called the Thomson coefficient and correctly predicts the fraction of energy scattered per electron per unit solid angle for photons of zero (negligible) energy. Quantum mechanical corrections to Thomson's derivations were required to accurately describe scattering at higher energies as described in the next section.

The atomic form factor $F(x, Z)$ in Eq. (1.43) approaches zero for large angles θ and Z for small θ and falls off dramatically as x (proportional to photon energy) increases⁴⁰². These two effects imply that coherent elastic scattering is significant for low energy X-ray interactions with high- Z elements. The relative contributions of coherent and Compton (incoherent) scatter and photoelectric absorption to attenuation in carbon and gold are shown in Figure 1.27¹¹⁵. For body tissues in the diagnostic energy range, coherent scattering accounts for less than 5% of total scatter^{3,402}. In addition, the angular distribution is markedly peaked in the forward direction, with half the coherently-scattered photons being contained in cone angles of 38°, 29°, 23°, 19°, 15°, 12° and 9° for 10-, 20-, 30-, 40-, 60-, 80- and 100-keV photons, respectively. Total coherent cross sections σ_{coh} are obtained by integrating Eq. (1.43) from 0 to 180 degrees and are tabulated for each element as functions of energy^{402,403}. The smooth angular distribution of elastically-scattered radiation given by Eq. (1.43) is accurate for randomly ordered aggregates of atoms. If a narrow-energy-band photon beam interacts with an ordered array of atoms like a crystalline lattice (or grating) and the lattice spacing is of the order of the photon wavelength, positive reinforcement of the coherent scatter from crystal planes can occur, causing sharp peaks in the angular distribution of scattered radiation emission. This phenomenon, called Bragg scattering, forms the basis for X-ray crystallography. In the diagnostic energy range, coherent scattering plays a small role and can often be neglected. For energies below 1 keV, at which most X-ray microscopic imaging is performed, absorption dominates and coherent scattering plays an important role. At soft X-ray energies, the interaction with an atom is described by the complex amplitude¹¹⁵:

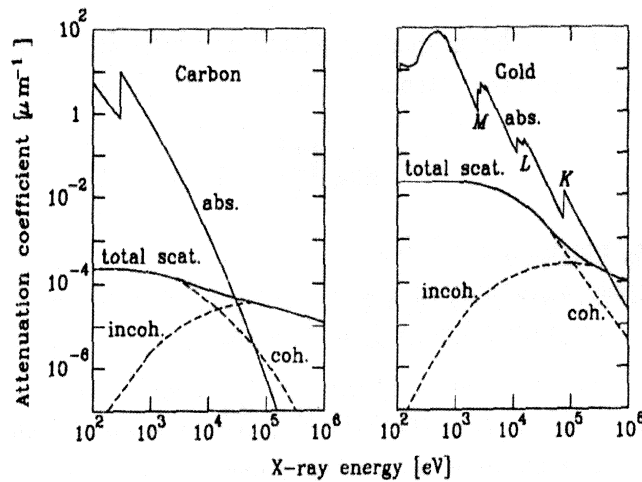


Figure 1.27. Scatter and absorption contributions to the linear attenuation coefficients of carbon and gold as functions of X-ray energy. (Reprinted with permission from Michette and Buckley¹¹⁵.)

$$A(\Theta, h\nu) = A_T(\Theta) [f_1(h\nu) + if_2(h\nu)], \quad (1.46)$$

where A_T is the amplitude given by the Thomson coefficient, Θ is the scattering angle and $f_1 + if_2$ is the complex number of electrons in the atom⁴⁰⁴. $f_1(h\nu)$ and $f_2(h\nu)$ are the atomic scattering factors which describe scattering and absorption, respectively, by the atom. They are independent of Θ at low energy. The scattering intensity for a single electron predicted by the Thomson coefficient of Eq. (1.45) must be multiplied by the square of the number of electrons involved to obtain the coherent scattering cross section for a multi-electron atom^{115,404}:

$$\frac{d\sigma_{coh}}{d\Omega} = \frac{r_0^2}{2} (1 + \cos^2 \Theta) |f_1 + if_2|^2, \quad (1.47)$$

which, integrated over all angles gives:

$$\sigma_{coh} = \frac{8\pi r_0^2}{3} |f_1 + if_2|^2. \quad (1.48)$$

The refractive index, a key parameter for soft X-ray microscopy, is given by:

$$n = 1 - \delta - i\beta = 1 - K(f_1 + if_2), \quad (1.49)$$

$$\text{where } \delta = \frac{r_0 \lambda^2}{2\pi} n_a f_1 \quad (1.50)$$

is the refractive index decrement,

$$\beta = \frac{r_0 \lambda^2}{2\pi} n_a f_2 \quad (1.51)$$

is the absorption index,

$$\text{and } K = \frac{n_a r_0 \lambda^2}{2\pi}, \quad (1.52)$$

in which $n_a = \frac{\rho N_0}{A}$, ρ is the density, N_0 Avogadro's number and A the atomic weight. After traveling a distance x through an attenuating medium, the incident wave amplitude A_0 is reduced to:

$$A = A_0 \exp\left(\frac{-2\pi\beta x}{\lambda}\right) \exp\left(\frac{i2\pi\delta x}{\lambda}\right), \quad (1.53)$$

and the intensity is given by:

$$I = |A|^2 = I_0 \exp\left(\frac{-4\pi\beta x}{\lambda}\right). \quad (1.54)$$

The phase change is seen to be $2\pi\delta x/\lambda$ and the attenuation is $e^{-\mu x}$ where the attenuation coefficient

$$\mu = \frac{4\pi\beta}{\lambda} = 2n_a r_0 \lambda f_2. \quad (1.55)$$

f_1 and f_2 are thus associated with the phase shift and absorption components of the refractive index, respectively. While the phase of visible light waves is retarded by interaction with a material, that of X-ray waves is usually advanced relative to the incident wave. The tabulated optical constants of Henke⁴⁰⁵ and others are usually obtained by absorption measurements of f_2 using thin foils, followed by calculation of f_1 from the Kramers-Kronig relationships^{115,404}. It is noted that the ratio f_1/f_2 increases rapidly with X-ray energy which forms the basis of the argument for recent experiments using relatively hard X-ray phase imaging for soft tissues^{160,162,238,239}.

1.3.2.2 Inelastic Compton Scattering

Compton scattering, which dominates among the competing attenuation mechanisms at higher diagnostic energies, involves the transfer of kinetic energy from incident photons to atomic electrons with which they collide^{1,3,15,20,115}. For the chance of a Compton interaction to be high, the incident photon energy must be large compared to the binding energy of the electron involved, and inelastic scattering usually involves outer-shell, loosely-bound atomic electrons. These electrons are ejected from the atom: Compton scattering is an ionizing event which contributes to exposure and dose.

When the photon energy is not negligible compared to m_0c^2 its momentum can no longer be neglected and the momentum it loses after being deviated through non-zero scattering angles must be conserved by transfer to the ejected Compton electron. Considering the involved electron to be at rest and free (reasonable at the photon energies for which inelastic scattering is important), a Compton interaction is analogous to a collision between a (lighter) queue ball and a (heavier) billiard ball. The plane of the interaction (containing the balls' centers) is defined by the plane containing the photon's incident and scattered trajectories. Since there is no momentum out of this plane, the path of the fast electron must also lie in this plane, and the interaction can be pictured as shown in Figure 1.28³. The energies of the incident photon, scattered photon and receding electron are represented by $h\nu$, $h\nu'$ and E respectively. The scattering angle for the photon and recoil angle for the electron are Θ and Φ , both with respect to the incident photon trajectory.

Using relativistic expressions for kinetic energy and momentum and conservation of energy and momentum, it can be shown that the reduced energy of the scattered photon is given by:

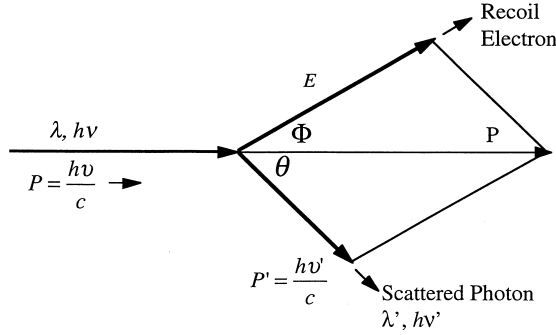


Figure 1.28. Compton scattering geometry. (Adapted from Johns and Cunningham³.)

$$h\nu' = h\nu \left[\frac{1}{1 + \alpha(1 - \cos\Theta)} \right], \quad (1.56)$$

and the kinetic energy of the recoil electron is:

$$E = h\nu \left[\frac{\alpha(1 - \cos\Theta)}{1 + \alpha(1 - \cos\Theta)} \right], \quad (1.57)$$

where dimensionless $\alpha = \frac{h\nu}{m_0c^2} = \frac{h\nu}{511\text{keV}}$, with $h\nu$ in keV, or, in terms of wavelength:

$$\lambda' = \lambda + \frac{h}{m_0c}(1 - \cos\Theta) = \lambda + 0.0243(1 - \cos\Theta). \quad (1.58)$$

The quantity $\frac{h}{m_0c}(1 - \cos\Theta)$ is known as the Compton shift and gives the increase in wavelength of the scattered photon¹. It is interesting to note that the Compton shift in wavelength at a particular scattering angle is independent of incident photon energy, but the Compton shift in terms of energy depends very strongly on energy. For example, at 90° for a 10-keV photon the Compton shift in energy is 0.2 keV (2%) whereas for a 10-MeV photon it is 9.51 MeV (>95%). True to the billiard-ball analogy, the above equations confirm that if the electron takes a direct hit, the photon will be backscattered through 180° imparting to the electron the maximum possible kinetic energy:

$$E_{\text{max}} = h\nu \left[\frac{2\alpha}{1 + 2\alpha} \right], \quad (1.59)$$

while if the photon barely ticks the electron the photon will be minimally deviated in its path, $\cos\Theta = 1$, the photon's energy after scattering will be almost equal to its incident energy, and the electron will be perturbed in a direction almost perpendicular to the incident photon trajectory.

The probability of a Compton interaction was first calculated by Klein and Nishina in 1928^{1,406}. The Klein-Nishina equation, based on Dirac's relativistic theory, has been repeatedly shown to correctly predict experimental results by taking the recoil of the electron into account. The differential cross section for Compton scattering is given by the product of the Thomson coefficient, Eq. (1.45) above, and a correction term designated f_{KN} :

$$\frac{d\sigma_{Compton}}{d\Omega} = \frac{r_0^2}{2} (1 + \cos^2\Theta) (f_{KN}), \quad (1.60)$$

$$\text{where } f_{KN} = \left[\frac{1}{1 + \alpha(1 - \cos\Theta)} \right]^2 \left\{ 1 + \frac{\alpha^2(1 - \cos\Theta)^2}{[1 + \alpha(1 - \cos\Theta)](1 + \cos^2\Theta)} \right\}. \quad (1.61)$$

At diagnostic energies, the Compton scattering cross section is slightly less at a scattering angle Θ of 180° than at 0° , with a minimum at 90° , whereas for higher-energy photons scattering becomes increasingly peaked in the forward direction. The effect of incorporating f_{KN} into the equation for the Compton cross section is to decrease the amount of scatter predicted by Thomson's equation, particularly for high-energy photons and large scattering angles.

1.3.3 Absorption

As an alternative to scattering, a photon may be completely absorbed and removed from the beam, a process more likely than scattering at low energies as shown in Figure 1.27 and also at extremely high energies. Photons may be completely removed from the beam by photoelectric absorption for soft- and diagnostic X rays, or by pair production or photodisintegration at very high energies.

1.3.3.1 Photoelectric Absorption

The photoelectric effect, for the discovery of which Einstein received the Nobel Prize in physics in 1921, involves a collision of the incident photon with a bound atomic electron^{1,3,15,20}. The electron is ejected from the atom with kinetic energy equal to the difference between the photon's energy and the binding energy of the orbital electron:

$$KE_{PE} = h\nu - BE. \quad (1.62)$$

Electrons may be ejected from any shell, with the required energy decreasing rapidly from the K to the L to the M and to orbitals still more distant from the nucleus. Electrons ejected by low-energy photons are ejected in a direction approximately perpendicular to the incident photon trajectory and

increasingly toward the forward direction as photon energy is raised. The photoelectric cross section varies with the fourth power of the absorber's atomic number, linearly with absorber density and inversely with absorber atomic weight and, in general, inversely with the third power of photon energy:

$$\sigma_{PE} \propto \frac{\rho Z^4}{A(h\nu)^3}. \quad (1.63)$$

Photoelectric absorption is most likely at energies just higher than the various electron binding energies causing sharp discontinuities in the curve relating the photoelectric cross section to photon energy. These jumps in the photoelectric cross section are referred to as the K-, L- and M- edges and so forth, according to the shell from which the electron is ejected. Photoelectric absorption is most likely to involve an electron whose binding energy is just below the photon energy: Photons with sufficient energy are most likely to interact with K-shell electrons. The minimum kinetic energy required for a photoelectron to escape from the surface of a material is called the work function Φ_0 of the material³⁴ and is on the order of 2 to 6 eV.

After ejection of an inner-shell electron by the photoelectric effect, the absorber atom is left in an excited state. It can return to stability either by emission of characteristic radiation or by ejection of an Auger electron. Both characteristic radiation and Auger electron ejection occur as a consequence of the inner-shell vacancy being filled by an electron from an outer shell “falling in” to take the place of an ejected photoelectron. An Auger electron is an electron ejected from a shell more distant from the nucleus than that in which the vacancy occurred. The fluorescent yield, defined as the ratio of characteristic photons to Auger electrons emitted after photoelectric absorption, increases from a few percent in soft tissue to 95% in lead³. The energy of a characteristic photon is equal to the difference in binding energies (BE) between the inner shell from which the photoelectron was ejected and the outer shell from which the electron filling the vacancy originated:

$$h\nu_{\text{characteristic}} = BE_{\text{inner}} - BE_{\text{outer}}. \quad (1.64)$$

The kinetic energy of an Auger electron is equal to the difference in binding energies of the two shells involved decremented by the energy required to eject the Auger electron:

$$KE_{\text{Auger}} = BE_{\text{inner}} - (BE_{\text{outer}} + BE_{\text{Auger}}). \quad (1.65)$$

Since Auger electrons are usually ejected from the same shell as that from which the electron making the downward transition to fill a vacancy originated:

$$KE_{\text{Auger}} = BE_{\text{inner}} - 2BE_{\text{outer}}. \quad (1.66)$$

Due to their charge, Auger electrons are absorbed in surrounding tissues. Characteristic X rays caused by photoelectric absorption are few enough in number and low enough in energy that their contribution to transmitted X-ray images can be ignored.

1.3.3.2 Pair Production

Pair production, defined as the conversion of a photon to an electron-positron pair, may occur above a threshold of 1.02 MeV. A highly-energetic photon may interact with the strong field of the nucleus and be eliminated from the beam. In its place a positive and a negative electron appear. The magnitude of the threshold energy for pair production is determined by the energy equivalent of the mass of these two electrons. Above the threshold, the cross section for pair production increases rapidly with photon energy. Pair production does not occur in the diagnostic energy range, but is an important interaction mechanism in radiation therapy, discussed in Volume 2.

1.3.3.3 Photodisintegration

Photonuclear interactions involve the absorption of a photon by the nucleus followed by the ejection of a nucleon. Very high threshold photon energies (2.22 MeV for hydrogen, 18.7 MeV for carbon and 15.7 MeV for oxygen²⁰) are required to overcome the nuclear binding energies of protons and neutrons, and photodisintegration is not relevant in diagnostic applications of ionizing radiation.

1.3.4 Attenuation Cross Sections and the Linear Attenuation Coefficient

As alluded to earlier, attenuation involves all the processes causing a reduction in the number of photons in an X-ray beam as it traverses an interaction medium or absorber. In diagnostic and other imaging applications of ionizing radiation, ignoring the inverse square law (see the beginning of Section 1.3), the total attenuation cross section, σ_{tot} , includes contributions from all the involved processes described above: elastic and inelastic scattering and photoelectric absorption:

$$\sigma_{tot} = \sigma_{coh} + \sigma_{Compton} + \sigma_{PE}. \quad (1.67)$$

The cross sections σ are a measure of the likelihood that a particular interaction will occur for an individual target or atom in the absorber. Cross sections are tabulated⁴⁰³ with units of area (e.g. Barnes: 1 Barn = $10^{-24} \text{ cm}^2/\text{atom}$).

For a narrow monoenergetic beam of energy $h\nu$, the number of photons remaining in the beam after traversing a thickness x of absorber is given by^{1,3,15,20}:

$$N = N_0 e^{-\mu x} \quad (1.68)$$

where N_0 is the number of photons incident on the absorber and μ is defined as the linear attenuation coefficient of the absorber material at energy $h\nu$. In terms of intensity:

$$I = I_0 e^{-\mu x}. \quad (1.69)$$

The linear attenuation coefficient has units of reciprocal distance (e.g. cm^{-1}) and can be calculated as²⁰:

$$\mu = n_v \sigma_{tot} = n_m \rho \sigma_{tot}, \quad (1.70)$$

where n_v and n_m are the number of atoms per unit volume or per unit mass, respectively, in the attenuating medium of infinitesimal thickness dx , σ_{tot} is the total cross section, and ρ is the density of the medium (e.g. grams per cubic centimeter). The linear attenuation coefficient is a function of the incident photon energy and the atomic number and density of the absorber. A related quantity, the mass attenuation coefficient is defined as:

$$\frac{\mu}{\rho} = n_m \sigma_{tot} \quad (1.71)$$

and has units of area per unit mass (e.g. cm^2/gram). The mass attenuation coefficient is independent of absorber density. For dose and radiation damage considerations, it is often necessary to calculate the energy actually absorbed in the object using the energy absorption coefficient:

$$\mu_{ab} = \mu \left(\frac{E_{ab}}{h\nu} \right), \quad (1.72)$$

where E_{ab} is the average energy absorbed per interaction.

Eq.s 1.68 and 1.69 will only be valid for experiments involving monoenergetic photons where the measurement of transmitted intensity is made in the narrow beam geometry illustrated in Figure 1.29²⁰. As shown, this geometry can be achieved by placing the absorber close to the collimated radiation source and the small, single-element detector some distance away. This arrangement excludes most of the scattered radiation from the measurement, since, except for very small scattering angles, it will diverge from the narrow beam and escape detection. In practice, for broad-band Bremsstrahlung spectra, the transmitted intensity must be calculated as an integral over photon energy, $h\nu$:

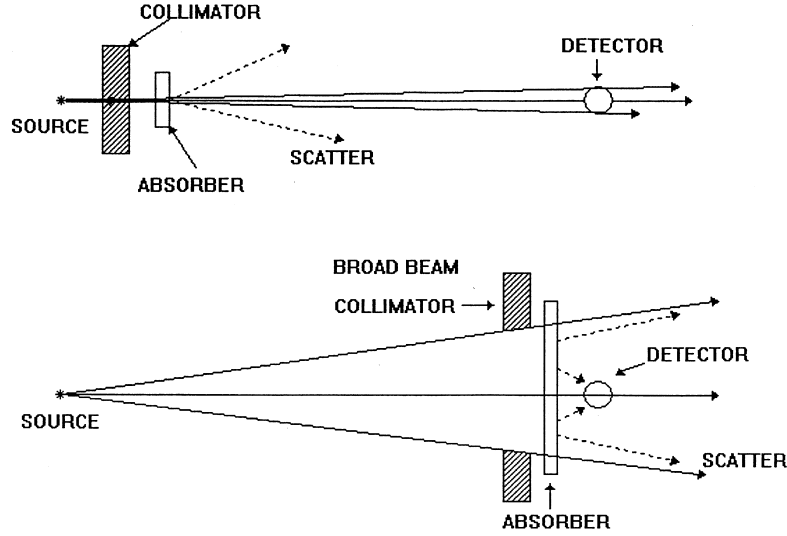


Figure 1.29. Narrow and broad beam geometry for measuring attenuation. (Adapted from Anderson²⁰.)

$$I = \int_0^{h\nu_{\max}} I_0(h\nu) e^{-\mu(h\nu)x} d h\nu. \quad (1.73)$$

For modeling and other purposes, it may be desirable to fit the tabulated cross-section data, since the energy increments are generally rather coarse (e.g. 5, 10 or 20 keV). This has often been done successfully using an equation of the form^{407,408}:

$$\mu(h\nu) = a_1 f_1(h\nu) + a_2 f_2(h\nu) = a_1 \frac{1}{(h\nu)^3} + a_2 f_{KN}(h\nu), \quad (1.74)$$

where a_1 and a_2 are functions of physical properties of the absorber and $f_{KN}(h\nu)$ is the appropriate form of the Klein-Nishina equation. The first term is associated with absorption due to the photoelectric effect and the second accounts for Compton scattering. The functions are given by:

$$a_1 = \frac{K_1 \rho Z^4}{A} \quad (1.75)$$

$$\text{and } a_2 = \frac{K_2 \rho Z}{A}, \quad (1.76)$$

where the K 's are constants, ρ is the material density, Z the atomic number and A the atomic weight of the absorber. The appropriate form of the Klein-Nishina formula is³:

$$f_{KN}(h\nu) = \frac{3}{4} \sigma_0 \left\{ \left(\frac{1+\alpha}{\alpha^2} \right) \left[\frac{2(1+\alpha)}{1+2\alpha} - \frac{\ln(1+2\alpha)}{\alpha} \right] + \frac{\ln(1+2\alpha)}{2\alpha} - \frac{1+3\alpha}{(1+2\alpha)^2} \right\}, \quad (1.77)$$

$$\text{where } \alpha = \frac{h\nu}{m_0 c^2} = \frac{h\nu}{511 \text{ keV}},$$

and the total cross section σ_0 (the Thomson classical scattering coefficient) is given by:

$$\sigma_0 = \frac{8}{3} \pi r_0^2 = 66.525 \times 10^{-26} \text{ cm}^2, \quad (1.78)$$

in which the classical electron radius is:

$$r_0 = \frac{ke^2}{m_0 c^2} = 2.81794 \times 10^{-13} \text{ cm},$$

and the constant

$$k = 8.9875 \times 10^{13} \frac{\text{Ncm}^2}{\text{C}^2} \text{ arises from Coulomb's law.}$$

For practical purposes the $3/4 \sigma_0$ of Eq. (1.77) can be lumped with K_2 in Eq. (1.76), and $f_{KN}(h\nu)$ taken as the expression within the braces. Eq. (1.74) can be fit to the tabulated data (using minimum least squared error or other appropriate criterion) over the energy ranges of interest by finding a set of coefficients K_1 and K_2 for each element of interest. In general it will be necessary to calculate different sets of K 's on each side of absorption edges spanned by the energy range at hand. Attenuation by compounds can be estimated according to the rule of mixtures^{3,409-411}:

$$\bar{Z} = \sqrt[m]{a_1 Z_1^m + a_2 Z_2^m + \dots + a_n Z_n^m + \dots}, \quad (1.79)$$

where \bar{Z} is the effective atomic number of a mixture of materials of atomic number Z_1 to Z_n and a_1 to a_n are the fractional numbers of electrons per gram of the various materials.

1.3.5 Interaction of X rays with Detector Materials

A very important class of interactions of X rays with matter involves their absorption and conversion in imaging and other X-ray detectors. Often, it is the electrons liberated by photoelectric and Compton interactions in the active detector material which ultimately produce the signal which is sensed. Alternatively, visible light emitted when an atom excited by one of these mechanisms returns to stability may be detected by an electronic detector or form latent image centers in the silver bromide grains of a film emulsion. In order to detect X rays efficiently and minimize the required exposure to the patient, a detector material should be dense and of high atomic number to maximize the number of interactions described by the foregoing equations. There is almost always a tradeoff between detector thickness and spatial resolution: A thick detector will stop and convert more X rays, but scatter of X rays and possibly other quanta within the detector itself degrades the spatial resolution of the acquired image, obscuring fine detail.

Recent developments promise to yield electronic detector arrays capable of detecting X rays directly; that is, converting X-ray energy directly to a measurable quantity such as voltage or charge using very dense, novel solid state materials such as CdZnTe and HgCdTe^{412,413}. Another approach uses amorphous selenium for direct X-ray detection^{414,415}. But most available detectors, including photostimulable phosphor plates⁴¹⁶⁻⁴²⁸ and the new amorphous silicon arrays which theoretically could eventually also be used in a direct mode⁴²⁹⁻⁴³³, first convert the X rays to visible light which is then detected, either by film or by electronic imaging detectors including photomultiplier tubes (PMT's), charge-coupled devices (CCD's) and tube-based cameras such as Vidicons and Plumbicons⁴³⁴⁻⁴⁴⁰. There are two primary reasons for this. The first is that most X-ray sensitive materials are too penetrable (either their mass density is too low or they have to be fabricated thin in order to preserve spatial resolution) to stop X rays efficiently. The second reason, which applies to CCD's and most silicon-based solid state devices, is that the active sensing material is not radiation hard: With continued exposure key properties like dark noise and charge transfer efficiency are degraded to unacceptable levels⁴⁴¹⁻⁴⁴³.

The scintillating materials used to convert the transmitted X-ray pattern to light in the visible spectrum fall into two major categories: granular phosphors⁴⁴⁴⁻⁴⁵⁵ and solid crystals^{456,457}. It is interesting to note that the first scintillation detector was used by Roentgen in his discovery of X rays when he observed the glowing of a barium platinocyanide-covered paper screen in a darkened room while experimenting with electrical discharges in a partially-evacuated tube^{33,458-461}. Historically, the most common type of imaging X-ray detector has been the film-screen system. Thin granular phosphor screens (between about fifty and two hundred microns thick) on one or both sides of the film absorb X rays and convert them with some relatively low efficiency (between about five and twenty percent) to light, generally in the green portion of the visible spectrum to which silver bromide film emulsion is most sen-

sitive. The phosphor particles, usually with densities between five and eleven grams per cubic centimeter and diameters in the five- to twenty-micron range, are held together by a plastic binder matrix. A reflective front-side coating increases the light emitted in the direction of the film. Besides conversion efficiency, the main problem is that light scatters laterally within the screen material, degrading the spatial resolution of the image at the film plane. Opacifiers are often added to the binder matrix to decrease this spreading of light at the cost of reduced efficiency, but the spatial resolution is generally no better than the screen thickness.

The advantage of solid crystalline scintillators like cesium iodide (CsI) is that the material can be grown in sheets of close-packed single-crystal columns up to several hundred microns thick. Absorption efficiency is therefore as good or better than that of the thickest phosphor screens. Light emitted as a result of X-ray absorption in a columnar crystal does not spread appreciably laterally into adjacent crystals due to the refractive index mismatch at the boundary, but is channeled down the crystal to the film or other detector stage. Spatial resolution is therefore limited by the diameter of the individual crystal columns. The problems with crystal scintillators include their expense and susceptibility to hygroscopic or other degradation. Their conversion efficiency is also somewhat lower than the more efficient granular phosphors.

Early detectors for computed tomography (CT scanners) were based on ionization of pressurized gases such as xenon^{462–464}. These detectors were very linear and stable, and some scanner manufacturers still employ them, but they are rather inefficient due to the low density of the gas. Cadmium tungstate scintillators coupled to photodiodes have found broad application in CT scanners; others such as bismuth germanate, CsI and sodium iodide have been tried; and a number of novel scintillators, including ceramic materials, have been developed for the purpose⁴⁶⁵. Problems with monocrystalline materials include afterglow, low mechanical strength, hysteresis (response depends on irradiation history), and hygroscopic attack. Promotion of transparency of ceramic materials can be problematic.

1.3.6 Object, Subject and Image Contrast

While there is no universally-accepted set of terms to describe the contrast at the various stages of the imaging procedure, it is important at least to recognize the factors involved at each stage, facilitating clarity of explanation and understanding. If one considers an object or small inclusion, represented by subscript 1, to be imaged against a background designated by subscript 0, the object contrast may be defined in terms of their linear attenuation coefficients as:

$$C_{\text{object}} = \frac{|\mu_1 - \mu_0|}{\mu_0}. \quad (1.80)$$

This quantity embodies the physical differences in density and atomic number available to potentially allow discrimination of the object from the background in a displayed image. Object contrast is sometimes called intrinsic or patient contrast. Subject contrast may be defined as:

$$C_{subject} = \frac{|\Phi_1 - \Phi_0|}{\Phi_0}, \quad (1.81)$$

where Φ is the photon fluence emerging from the patient after passing through the inclusion and the background. Since detectors' responses are usually linear with energy, it might be more appropriate to define subject contrast as:

$$C_{subject} = \frac{|\Psi_1 - \Psi_0|}{\Psi_0}, \quad (1.82)$$

where Ψ is the energy fluence emerging on the detector side of the patient. In fact, though the results are not exactly the same, it makes little difference if photon fluence, energy fluence or exposure are used in the calculation of subject contrast³. Image contrast has to do with the sum total result of the whole system: density differences in the patient, X-ray spectrum utilized, efficiency and response characteristics of the detector and any other components used to present the image to the observer, etc. It may be defined as:

$$C_{image} = \frac{|I_1 - I_0|}{I_0}, \quad (1.83)$$

where I indicates the flux of visible light energy presented to the observer's eye.

Object contrast is due to intrinsic differences in the imaged patient's tissues, and can only be improved by the addition of some contrast-enhancing agent, such as iodine injected into the vascular compartment. Subject contrast is affected by the X-ray spectrum used to produce the image. In general, the differences between attenuation coefficients of various tissues and materials are larger at low energies than at high, so low-energy beams will produce higher subject contrast. The low-energy limits are set by the penetrating capacity of X rays. In addition, illumination preferentially accentuating energies just above an absorption edge in one of the tissues of interest can produce enhanced subject contrast. The most important determinant of conspicuity of features or discontinuities in the patient is image contrast. The contrast-producing characteristics of the detector system can be influenced to a larger degree than is usually the case for contrast agents or technique selection. Films and film-screen systems are available with a wide variety of contrast characteristics, and the development process can also be tailored to increase or decrease image contrast. The offset (dark level) and gain of electronic detectors can be adjusted to emphasize contrast over particular ranges of

intensity (subject contrast). Window width and level of electronic display devices are usually under realtime control of the operator and have made a large impact in improving the quality of the images presented to the observer by, on the one extreme, accentuating very small differences in the detected X-ray intensity or, on the other, allowing simultaneous display of a very wide dynamic range at comfortable levels of illumination.

1.4 Quantities and Units

The purpose of this section is to present some of the fundamental concepts involved in the measurement and quantification of radiation intensity, exposure and dose and to summarize, in tabular form, the units used in this book. Discussion of some special units adopted historically for use in the radiation science community but now being phased out of use is included, though the standard units will be used throughout this book.

Not long after their discovery, evidence started to mount of the potentially harmful effects that X and gamma rays could have on living organisms⁴⁶⁶, though debate over the root cause of these effects continued into the 1920's. The formation of an international radiation protection committee was discussed at the first meeting of the International Congress of Radiology in 1925, and the International Committee on X-ray and Radium Protection (ICRP) was formed in 1928 during the Congress's second meeting in Stockholm⁴⁶⁷. Since 1931 the ICRP has issued a series of reports in which they made recommendations as to quantities and units to be used to describe radiation and related entities, apparatus and methods to make these measurements in the clinic, and requirements for adequate shielding for personnel and patients. Another body whose purpose it is to compile reports and formulate recommendations regarding the measurement of ionizing radiation and standardization of the units used to describe the measured quantities is the International Commission on Radiation Units (ICRU)^{468–470}. The ICRU has issued a number of reports over the years, which specialized in the definition and dissemination of units to be used in the radiological sciences and in radiation protection. The Commission defined some units specific to radiological quantities. Today, all involved bodies are advocating adoption of the units of the Systeme International (SI units), recommended by the Comite International des Poids et Mesures (CIPM). In 1975, the General Conference on Weights and Measures (CGPM) accepted two SI units, the gray and the becquerel, specific to the radiological sciences³.

1.4.1 Fundamental Constants, Quantities and Units

The fundamental units of mass, length, time and current, from which most other units are derived, are, of course, the kilogram, the meter, the second and the ampere. A number of standard physical and electrical units and quantities are defined in Table 1.4 (adapted from Johns and Cunningham³ and Smith⁹).

Table 1.4.

Quantity	Symbol	Meaning	SI Unit/ abbreviation	Conversions or fundamental units
mass	m		kilogram / kg	
length	l		meter / m	
time	t		second / s	
current	I		ampere / A	
velocity	v	$v = l/t$	m/s	
acceleration	a	v/t	m/s^2	
force	F	ma	newton / N	$kg \cdot m/s^2$
energy	E	Fl	joule / J	$kg \cdot m^2/s^2$ 1 eV = $1.602 \times 10^{-19} J$
power	P	E/t	watt / W	J/s
frequency	f, ν	number/length or time	hertz / Hz	s^{-1}
charge	Q	It	coulomb / C	As
potential	V	E/Q	volt / V	J/C
capacitance	C	Q/V	farad / F	C/V
resistance	R	V/I	ohm / Ω	V/A
field strength	ϵ	force/ unit charge	*	V/m
magnetic flux density	B	force/ unit charge momentum	Tesla / T	1T = 10^4 Gauss Wb/m ²
magnetic flux	ϕ	integral of magnetic flux density	Weber / Wb	$T \cdot m^2$

A number of radiological units and quantities are defined in Table 1.5 (compiled from ICRU Report 51⁴⁷⁰, Johns and Cunningham³, and Attix⁴⁰⁰, and discussed in the following sections).

Table 1.5.

Quantity	Symbol	Meaning	SI Unit/ abbreviation	Fundamental units or Conversions
exposure	X	charge liberated per unit mass	C/kg	Q/m 1 Roentgen = 2.58×10^{-4} C/kg
energy imparted	ε	net energy absorbed in matter (see text)	*	J
absorbed dose	D	energy imparted per unit mass	gray / Gy	J/kg 1 Gy = 100 rad 1 Gy = 10^4 erg/g (kerma has same definition)
absorbed dose rate	\dot{D}	D/t	*	J/kg.s
quality factor	Q	weighting factor for varying biological effectiveness of radiation	*	
dose equivalent	H	QD	sievert / Sv	1 Sv = 100 rem
dose equivalent rate	\dot{H}			
activity	A	disintegrations/ second	becquerel / Bq	s^{-1} 1 Ci = 3.7×10^{10} Bq
fluence	Φ	particles/unit area	*	m^{-2}
fluence rate or flux density	ϕ	fluence/unit time	*	$m^{-2} \cdot s^{-1}$
energy fluence	Ψ	energy/unit area	*	J/m ²
intensity or energy flux	ψ	energy fluence/unit time	*	J/m ² s
linear energy transfer	LET	energy lost by particle per unit pathlength	*	J/m
lineal energy	y	energy imparted per mean chord length through volume	*	J/m

* No SI unit applies

1.4.2 Particle Fluence and Flux

We saw earlier that radiation beams are agents of energy transfer. There are a number of quantities used, either colloquially or in technical communication, to describe the passage or travel of energy through space or matter. Fluence, with units of number per unit area, refers to the number of quanta, particles or photons N passing through a unit area perpendicular to the beam:

$$\Phi = \frac{N}{A} \left(\frac{N}{m^2} \right). \quad (1.84)$$

Fluence rate (also called flux density), with units of number per unit area per unit time, is the fluence per unit time:

$$\phi = \frac{N}{A \cdot t} \left(\frac{N}{m^2 \cdot s} \right). \quad (1.85)$$

1.4.3 Energy Fluence and Flux

Energy fluence, with units of energy per unit area, describes the total energy of the particles traversing a unit area:

$$\Psi = \frac{NE}{A} \left(\frac{J}{m^2} \right). \quad (1.86)$$

For monoenergetic photons, for example, one can determine the total energy by multiplying the particle fluence by the energy of each photon. Energy-integrating detectors, such as solid state or crystal-based systems, may be used to estimate the energy fluence in practice, though this is not done routinely in the clinic. Mathematically, the total energy in a polychromatic beam incident on an area can be calculated from:

$$\Psi = \sum_{i=0}^{E_{\max}} n_i E_i, \quad (1.87)$$

where n_i is the number of particles with energy E_i , and the sum is over energies where i is incremented from zero up to the energy possessed by the most energetic particles in the beam (up to the value of kVp, for example). Energy flux, colloquially called intensity and equivalent to energy fluence rate, is the energy fluence per unit time:

$$\psi = \frac{NE}{A \cdot t} \left(\frac{J}{m^2 \cdot s} \right). \quad (1.88)$$

1.4.4 Exposure: the Roentgen

In general, it is practically difficult to measure intensity or fluence, and also not as useful (from a radiation protection standpoint, at any rate) as measuring a quantity more closely related to the potentially-harmful effects of ionizing radiation. Radiation damage from indirectly ionizing beams is not caused by the photons (or neutrons) directly, but by the fast electrons ejected from atoms in the absorbing medium. It is true that the initial interaction event is caused by the photons themselves, either in photoelectric or Compton interactions, but the number of these primary events is far smaller than that of the subsequent interactions of the ejected electrons with tissue atoms before they are brought to rest. Exposure is the quantity that was defined early on to quantify the potential of an X-ray beam to cause separation of charge in matter. The Roentgen is a unit of exposure originally defined as the amount of exposure required produce one electrostatic unit per cubic centimeter of air at standard temperature and pressure:

$$1 R = \frac{1 \text{ ESU}}{\text{cm}^3 \text{ of air at STP}} = \frac{1 \text{ ESU}}{0.001293 \text{ g air}}. \quad (1.89)$$

In the SI system, the unit of exposure is coulombs per kilogram with:

$$1 \text{ Roentgen} = 2.58 \times 10^{-4} \text{ coulomb/kg in air}. \quad (1.90)$$

1.4.5 Absorbed Dose: The Gray, the Rad and the Kerma

Biological effects depend on the amount of energy absorbed in tissue as a result of exposure to ionizing radiation, not on the ability of radiation to ionize air. The ICRU defines energy imparted to matter in a volume as⁴⁷⁰:

$$\varepsilon = R_{in} - R_{out} + \sum Q(J), \quad (1.91)$$

where R_{in} is the radiant energy incident on the volume which means the sum of the energies of all charged and uncharged particles that enter the volume, R_{out} is the radiant energy emerging from the volume, and $\sum Q$ is the sum of all changes of mass into energy or vice versa (e.g. annihilation of a positron or electron-positron formation in pair production) which occur in the volume. Radiant energy is defined as the energy of particles emitted, transferred or received out of or into the volume. Absorbed dose is then defined as:

$$D = \frac{\varepsilon}{m} \left(\frac{J}{kg} = Gy \right), \quad (1.92)$$

and absorbed dose rate by:

$$\dot{D} = \frac{D}{t} \left(\frac{\text{Gy}}{\text{s}} \right). \quad (1.93)$$

Quantification of absorbed dose has often been in terms of the older units, ergs/g and rads, but these are being phased out in favor of the gray. Kerma, with units of gray, J/kg, rad, or erg/g, is a previously-recommended term⁴⁷¹ denoting absorbed dose which still finds use, particularly in the radiation therapy field.

Since it requires 33.85 eV to produce one ion pair in air and each ion pair has a charge of 1.6×10^{-19} coulomb, 33.85 joules are absorbed from an exposure of 1 C/kg in air. Thus an exposure of 1 C/kg in air results in an absorbed dose of 33.85 Gray. In general, the absorbed dose may be calculated using:

$$\text{energy absorbed (Gray)} = \Psi \left(\frac{\text{J}}{\text{m}^2} \right) \frac{\mu_{ab}}{\rho} \left(\frac{\text{m}^2}{\text{kg}} \right), \quad (1.94)$$

where $\frac{\mu_{ab}}{\rho}$ is defined as the energy absorption coefficient³ or the mass energy absorption coefficient¹⁸. The energy absorption coefficient is defined as the product of the mass absorption coefficient and the fraction of photon energy absorbed in a particular medium per interaction:

$$\frac{\mu_{ab}}{\rho} = \frac{\mu}{\rho} \cdot \left(\frac{\bar{E}_{ab}}{h\nu} \right). \quad (1.95)$$

Tables are available giving the energy absorption coefficient as a function of photon energy⁴⁷².

1.4.6 Dose Equivalent: LET, Q, the Sievert and the Rem

Alpha particles and other charged species cause far more biological damage per quanta than do photons of the same energy. One reason for this is that they deposit their energy in the tissue over far shorter distances. Linear energy transfer (LET in J/m or, traditionally, in keV/micron) is a measure of the rate at which an ionizing particle deposits energy along its path in tissue. Alpha particles may deposit energy at rates up to 1000 times higher than electrons³. High-LET particles produce stronger biological effects than do low-LET species. The quality factor, Q , is introduced to take the varying “biological effectiveness”, or the potential of different types of radiation to cause adverse biological effects, into account. Q varies with LET, and is quantified for a particular radiation by comparing the dose of the radiation required to produce a particular biological effect with the dose of a reference radiation

required to elicit the same effect. The reference radiation may be medium-energy (e.g. 200-keV) X rays or ^{60}Co radiation^{18,473}. Dose equivalent, H , expresses the damaging effects of different radiations on a common scale by incorporating the quality factor:

$$H = DQ \text{ (Sv)}. \quad (1.96)$$

The Sievert is the SI unit for dose equivalent. An older unit still in common use is the rem. Quality factors for several types of radiation are listed in Table 1.6⁴⁷⁴. In the field of radiation biology, a similar modifying factor, the relative biological effectiveness or RBE, is used to compare the potential for damage of various types of radiation on a common scale.

Table 1.6.

Radiation	Q
X rays, gamma rays, beta particles	1
thermal neutrons	5
neutrons and protons	20
alpha-particles	20
heavy recoil nuclei	20

1.5 References

1. R. D. Evans. *The Atomic Nucleus*. (Robert Krieger, Malabar, Florida, 1955).
2. J. T. Bushberg, J. A. Seibert, E. M. Leidholdt, J. M. Boone. *The Essential Physics of Medical Imaging*. (Williams and Wilkins, Baltimore, 1994).
3. H. E. Johns, J. R. Cunningham. *The Physics of Radiology*. (Charles Thomas, Springfield, Illinois, 1983).
4. T. S. Rao-Sahib, D. B. Wittry, *J. Appl. Phys.* **45**, 5060 (1974).
5. J. A. Wheeler, R. Ladenburg, *Phys. Rev.* **60**, 754 (1941).
6. B. W. Soole, *J. Phys.* **B5**, 1583 (1972).
7. A. B. Wolbarst. *Physics of Radiology*. (Appleton and Lange, Norwalk, Connecticut, 1993).
8. J. Selman. *The Fundamentals of X-ray and Radium Physics*. (Charles Thomas, Springfield, Illinois, 8th edition, 1994).
9. R. J. Smith. *Electronics: Circuits and Devices*. (Wiley, New York, 3rd edition, 1987).
10. A. V. Crewe, D. N. Eggenberger, J. Wall, L. M. Welter, *Rev. Sci. Instrum.* **39**, 576 (1968).
11. J. I. Goldstein, et al., *Scanning Electron Microscopy and Microanalysis* (Plenum, New York, 1981).
12. H. H. Pattee, in *X-ray Microscopy and Microradiography*, V. E. Cosslett, et al., Eds., (Academic, New York, 1957), p. 278.
13. W. P. Dyke, J. K. Trolan, W. W. Dolan, F. J. Grundhauser, *J. Appl. Phys.* **25**, 106 (1954).

14. F. M. Charbonnier, J. P. Barbour, W. P. Dyke, *Radiology* **117**, 165 (1975).
15. J. E. Turner. *Atoms, Radiation, and Radiation Protection*. (Wiley, New York, 1995).
16. M. M. Ter-Pogossian. *The Physical Aspects of Diagnostic Radiology*. (Harper and Row, New York, 1969).
17. G. L. Clark. *Applied X rays*. (McGraw Hill, New York, 1955).
18. W. R. Hendee, E. R. Ritenour. *Medical Imaging Physics*. (Mosby, St. Louis, 1992).
19. P. Sprawls. *Physical Principles of Medical Imaging*. (Medical Physics Publishing, Madison, Wisconsin, 1993).
20. D. W. Anderson. *Absorption of Ionizing Radiation*. (University Park Press, Baltimore, 1984).
21. W. Huda, R. Slone. *Review of Radiologic Physics*. (Williams and Wilkins, Baltimore, 1995).
22. V. Delgado, P. Ortiz, *Med. Phys.* **24**, 1089 (1997).
23. J. Rheinlander, L. Gerward, A. Lindegaard-Andersen, J. Larsen, *J. X-ray Sci. Technol.* **3**, 166 (1992).
24. K. Aoki, M. Koyama, *Med. Phys.* **16**, 529 (1989).
25. M. Green, in *X-ray Optics and X-ray Microanalysis*, H. H. Pattee, V. E. Cosslett, A. Engstrom, Eds., (Academic, New York, 1963), p. 185.
26. M. Green, V. E. Cosslett, *Brit. J. Appl. Phys. (J. Phys. D series 2)* **1**, 425 (1968).
27. M. Green, V. E. Cosslett, *Proc. Phys. Soc.* **78**, 1206 (1961).
28. H. Kulenkampff, *Annalen der Physik Leipzig* **69**, 548 (1922).
29. H. A. Kramers, *Phil. Mag.* **46** (series 6), 836 (1923).
30. R. Birch, M. Marshall, *Phys. Med. Biol.* **24**, 505 (1979).
31. D. M. Tucker, G. T. Barnes, D. P. Chakraborty, *Med. Phys.* **18**, 211 (1991).
32. T. Fewell, R. E. Shuping, K. R. Hawkins. *Handbook of Computed Tomography X-ray Spectra. HHS (FDA) Report No. 81-8162*. (U.S. Government Printing Office, Washington, 1981).
33. A. H. Compton, S. K. Allison. *X rays in Theory and Experiment*. (Van Nostrand, Princeton, 1967).
34. R. C. Weast, M. J. Astle, W. H. Beyer, Eds. *CRC Handbook of Chemistry and Physics*. (CRC Press, Boca Raton, Florida, 1983).
35. R. Beccherle, *et al.*, in *Digital Mammography*, A. G. Gale, S. M. Astley, D. R. Dance, A. Y. Cairns, Eds., (Elsevier, Amsterdam, 1994), p. 153.
36. M. Gambaccini, A. Taibi, A. Del Guerra, F. Frontera, M. Marziani, *Nuc. Inst. Meth. Phys. Res.* **A365**, 248 (1995).
37. R. E. Johnston, *et al.*, *Radiology* **200**, 659 (1996).
38. E. Burattini, *et al.*, *Radiology* **195**, 239 (1995).
39. F. E. Carroll, *Lasers in Surgery and Medicine* **11**, 72 (1991).
40. P. A. Tompkins, C. C. Abreu, F. E. Carroll, Q.-F. Xiao, C. A. MacDonald, *Med. Phys.* **21**, 1777 (1994).
41. R. Fahrig, M. J. Yaffe, *Med. Phys.* **21**, 1473 (1994).
42. R. Fahrig, M. J. Yaffe, *Med. Phys.* **21**, 1463 (1994).
43. E. L. Gingold, X. Wu, G. T. Barnes, *Radiology* **195**, 639 (1995).
44. 102nd Congress. *Mammography Quality Standards Act of 1992*. (U.S. Government Printing Office, Washington, 1992).
45. J. Law, *Brit. J. Radiol.* **66**, 44 (1993).
46. M. M. Goodsitt, H.-P. Chan, B. Liu, *Med. Phys.* **24**, 11 (1997).
47. M. J. Yaffe, *et al.*, *Radiology* **197**, 19 (1995).
48. M. Yoshimatsu, S. Kozaki, in *X-ray Optics Applications to Solids*, H. J. Queisser, Ed., (Springer, Berlin, 1977), p. 9.
49. N. Uspenski, *Physik. Zeitschr.* **15**, 717 (1914).
50. M. von Ardenne, *Die Naturwissenschaften* **27**, 485 (1939).
51. V. E. Cosslett, W. C. Nixon, *Nature* **168**, 24 (1951).
52. V. E. Cosslett, W. C. Nixon, *Nature* **170**, 436 (1952).
53. V. E. Cosslett, W. C. Nixon, *J. Appl. Phys.* **24**, 616 (1953).

54. V. E. Cosslett, W. C. Nixon, *X-ray Microscopy*. (Cambridge University Press, London, 1960).
55. V. E. Cosslett, W. C. Nixon, and H. E. Pearson, in *X-ray Microscopy and Microradiography*, V. E. Cosslett, *et al.*, Eds., (Academic, New York, 1957), p. 96.
56. W. C. Nixon, in *X-ray Microscopy and Microradiography*, V. E. Cosslett, *et al.*, Eds., (Academic, New York, 1957), p. 34.
57. W. C. Nixon, *Nature* **175**, 1078 (1955).
58. B. L. Henke, in *The Encyclopedia of Microscopy*, G. L. Clark, Ed., (Reinhold, New York, 1961), p. 675.
59. R. L. D. C. H. Saunders, in *X-ray Microscopy and X-ray Microanalysis*, A. Engstrom, V. Cosslett, H. Pattee, Eds., (Elsevier, Amsterdam, 1960), p. 244.
60. R. L. D. C. H. Saunders and L. Van der Zwan, in *X-ray Microscopy and X-ray Microanalysis*, A. Engstrom, V. Cosslett, H. Pattee, Eds., (Elsevier, Amsterdam, 1960), p. 293.
61. R. L. D. C. H. Saunders, in *Vth International Congress on X-ray Optics and Microanalysis*, G. Mollenstedt, K. H. Gaukler, Eds., (Springer, Berlin, 1969), p. 550.
62. R. L. D. C. H. Saunders, M. A. Bell, V. R. Carvalho, in *Vth International Congress on X-ray Optics and Microanalysis*, G. Mollenstedt, K. H. Gaukler, Eds., (Springer, Berlin, 1969), p. 569.
63. S. Bellman, H. A. Frank, P. B. Lambert, B. Oden, J. A. Williams, in *X-ray Microscopy and X-ray Microanalysis*, A. Engstrom, V. Cosslett, H. Pattee, Eds., (Elsevier, Amsterdam, 1960) p. 259.
64. D. A. Carpenter, M. A. Taylor, *50th Annual Meeting of the Electron Microscopy Society of America* (San Francisco Press, 1992), p. 1758.
65. W. M. Gibson, M. A. Kumakhov, *50th Annual Meeting of the Electron Microscopy Society of America* (San Francisco Press, 1992), p. 1726.
66. B. R. York, *50th Annual Meeting of the Electron Microscopy Society of America* (San Francisco Press, 1992), p. 1764.
67. D. Kruger, C. Abreu, W. Peppler, C. MacDonald, C. Mistretta, *Med. Phys.* **21**, 875 (1994).
68. A. Attaelmanan, S. Larsson, A. Rindby, P. Voglis, A. Kuczumow, *Rev. Sci. Instrum.* **65**, 7 (1994).
69. H. N. Chapman, K. A. Nugent, S. W. Wilkins, A. V. Rode, in *SPIE Volume 1741 Soft X-ray Microscopy*, (SPIE, Bellingham, Washington, 1992), p. 40.
70. K. Furuta, *et al.*, *Rev. Sci. Instrum.* **64**, 135 (1993).
71. N. Yamamoto, Y. Hosokawa, *Jpn. J. Appl. Phys.* **27**, L2203 (1988).
72. H. N. Chapman, *et al.*, in *X-ray Microscopy III*, A. G. Michette, G. R. Morrison, C. J. Buckley, Eds., (Springer, Berlin, 1992), p. 131.
73. K. Lewotsky, *Laser Focus World*, (September, 1994), p. 30.
74. H. N. Chapman, A. Rode, K. A. Nugent, S. W. Wilkins, *Applied Optics* **32**, 6333 (1993).
75. D. J. Thiel, D. H. Bilderback, A. Lewis, *Rev. Sci. Instrum.* **64**, 2872 (1993).
76. S. B. Dabagov, *et al.*, *Nuc. Inst. Meth. Phys. Res.* **B103**, 99 (1995).
77. A. Attaelmanan, P. Voglis, A. Rindby, S. Larsson, P. Engstrom, *Rev. Sci. Instrum.* **66**, 24 (1995).
78. D. J. Pugh, P. D. West, *J. Microsc.* **103**, 227 (1974).
79. G. Fuhrmann, H. Halling, R. Moller, J. Vell, V. Z. Shuang-Ren, in *IEEE Nuclear Science Symposium and Medical Imaging Conference*, (IEEE, New York, 1991), p. 2012.
80. R. H. Johnson, A. C. Nelson, D. H. Burns, in *12th International Congress for Electron Microscopy*, (San Francisco Press, 1990), p. 518.
81. P. C. Cheng, S. P. Newberry, H. G. Kim, I. S. Hwang, in *Modern Microscopies: Techniques and Applications*, P. J. Duke, A. G. Michette, Eds., (Plenum, New York, 1990), p. 87.
82. P. C. Cheng, *et al.*, in *X-ray Microscopy III*, A. G. Michette, G. R. Morrison, C. J. Buckley, Eds., (Springer, Berlin, 1992), p. 184.

83. A. Y. Sasov, *J. Microsc.* **147**, 169 (1987).
84. A. Y. Sasov, *J. Microsc.* **156**, 91 (1989).
85. L. A. Feldkamp, S. A. Goldstein, A. M. Parfitt, G. Jasion, M. Kleerekoper, *J. Bone Min. Research* **4**, 3 (1989).
86. J. L. Kuhn, S. A. Goldstein, L. A. Feldkamp, R. W. Goulet, G. Jasion, *J. Orthop. Res.* **8**, 833 (1990).
87. S. M. Hames, M. J. Flynn, D. A. Reimann, in *IEEE Nuclear Science Symposium and Medical Imaging Conference*, (IEEE, New York, 1992), p. 1331.
88. J. T. De Assis, R. T. Lopes, J. L. Rodrigues, in *IEEE Nuclear Science Symposium and Medical Imaging Conference*, (IEEE, New York, 1993), p. 1731.
89. F. W. Prior, *et al.*, in *Digital Mammography*, A. G. Gale, S. M. Astley, D. R. Dance, A. Y. Cairns, Eds., (Elsevier, Amsterdam, 1994), p. 143.
90. A. V. Clough, J. H. Linehan, C. A. Dawson, *Am. J. Physiol.* **272**, (Heart Circ. Physiol. 41), H1537 (1997).
91. D. R. Harder, M. L. Schulte, A. V. Clough, C. A. Dawson, *Am. J. Physiol.* **263**, H1616 (1992).
92. R. H. Johnson, H. Hu, S. T. Haworth, P. S. Cho, C. A. Dawson, J. H. Linehan, *Phys. Med. Biol.* **43**, 929 (1998).
93. E. Burattini, A. Balerna, Eds. *Biomedical Applications of Synchrotron Radiation*. (IOS Press, Amsterdam, 1996).
94. H. B. Stuhmann, Ed. *Uses of Synchrotron Radiation in Biology*. (Academic, London, 1982).
95. B. Chance, *et al.*, Eds. *Synchrotron Radiation in the Biosciences*. (Oxford University Press, London, 1994).
96. J. C. Giacomini, H. J. Gordon, in *Handbook on Synchrotron Radiation, Volume 4*, S. Ebashi, *et al.*, Eds., (North-Holland, Amsterdam, 1991), p. 349.
97. E. Rubenstein, *Nuc. Inst. Meth. Phys. Res.* **222**, 302 (1984).
98. H. Winick, S. Doniach, Eds. *Synchrotron Radiation Research*. (Plenum, New York, 1980).
99. H. Winick, *Scientific American* **257**, 88 (1987).
100. H. Winick, Ed. *Synchrotron Radiation Sources A Primer Volume 1*. (World Scientific, Singapore, 1994).
101. S. Ebashi, M. Koch, E. Rubenstein, Eds. *Handbook on Synchrotron Radiation Volume 4*. (North-Holland, Amsterdam, 1991).
102. G. Margaritondo. *Introduction to Synchrotron Radiation*. (Oxford University Press, New York, 1988).
103. A. A. Sokolov, I. M. Ternov. *Radiation from Relativistic Electrons*. (American Institute of Physics, New York, 1986).
104. E. Wehreter. *Compact Synchrotron Light Sources*. (World Scientific, Singapore, 1996).
105. A. Craievich, Ed. *Synchrotron Light: Applications and Related Instrumentation*. (World Scientific, Singapore, 1988).
106. E. B. Hughes, *et al.*, *Acta Radiologica* **S365**, 43 (1983).
107. C. Kunz, Ed. *Synchrotron Radiation*. (Springer, Berlin, 1979).
108. F. R. Elder, A. M. Gurewitsch, R. V. Langmuir, H. C. Pollock, *Phys. Rev.* **71**, 829 (1947).
109. F. R. Elder, R. V. Langmuir, H. C. Pollock, *Phys. Rev.* **74**, 52 (1948).
110. C. Archie, *IBM J. Res. Develop.* **37**, 373 (1993).
111. M. N. Wilson, *et al.*, *IBM J. Res. Develop.* **37**, 351 (1993).
112. H. Takada, K. Furukawa, T. Tomimasu, *Opt. Eng.* **27**, 550 (1988).
113. A. I. Erko, V. V. Aristov, B. Vidal. *Diffraction X-ray Optics*. (Institute of Physics, Bristol, 1996).
114. A. G. Michette. *Optical Systems for Soft X rays*. (Plenum, New York, 1986).
115. A. G. Michette, C. J. Buckley, Eds. *X-ray Science and Technology*. (Institute of Physics, Bristol, 1993).

116. H. Winick, in *Synchrotron Radiation Research*, H. Winick, S. Doniach, Eds., (Plenum, New York, 1980), p. 11.
117. E. Burattini, in *Biomedical Applications of Synchrotron Radiation*, E. Burattini, A. Balerna, Eds., (IOS Press, Amsterdam, 1996), p. 3.
118. G. Green, *BNL Report No.50522* (Department of Energy, 1977).
119. H. Winick, G. Brown, K. Halbach, J. Harris, *Physics Today*, (May, 1981), p. 50.
120. G. Brown, K. Halbach, J. Harris, H. Winick, *Nuc. Inst. Meth.* **208**, 65 (1983).
121. J. E. Spencer, H. Winick, in *Synchrotron Radiation Research*, H. Winick, S. Doniach, Eds., (Plenum, New York, 1980), p. 663.
122. W. Thomlinson, D. Chapman, N. Gmur, N. Lazarz, *Nuc. Inst. Meth. Phys. Res.* **A266**, 226 (1988).
123. D. Attwood, *et al.*, *Applied Optics* **32**, 7022 (1993).
124. G. S. Brown, in *Synchrotron Radiation Research Volume 2 Advances in Surface and Interface Science*, R. Z. Bachrach, Ed., (Plenum, New York, 1992), p. 317.
125. C. Capasso, *et al.*, *J. Vac. Sci. Technol.* **A9**, 1248 (1991).
126. H. Maezawa, Y. Suzuki, H. Kitamura, T. Sasaki, *Applied Optics* **25**, 3260 (1986).
127. P. Horowitz, J. A. Howell, *Science* **178**, 608 (1972).
128. P. Horowitz, *Ann. New York Acad. Sci.* **306**, 203 (1978).
129. E. Spiller, *et al.*, *Science* **191**, 1172 (1976).
130. J. Kirz, D. Sayre, in *Synchrotron Radiation Research*, H. Winick, S. Doniach, Eds., (Plenum, New York, 1980), p. 277.
131. M. Howells, J. Kirz, D. Sayre, G. Schmahl, *Physics Today*, (August, 1985), p. 22.
132. R. Feder, *Physics Today* (January, 1986), p. S12.
133. S. Richards, A. D. Rush, D. T. Clarke, W. J. Myring, *J. Microsc.* **142**, 1 (1986).
134. C. Jacobsen, *et al.*, *Phys. Med. Biol.* **32**, 431 (1987).
135. C. Jacobsen, S. Lindaas, S. Williams, X. Zhang, *J. Microsc.* **172**, 121 (1993).
136. K. Shinohara, H. Nakano, Y. Kinjo, M. Watanabe, *J. Microsc.* **158**, 335 (1990).
137. D. L. Shealy, R. B. Hoover, T. W. Barbee, A. B. C. Walker, *Opt. Eng.* **29**, 721 (1990).
138. R. B. Hoover, U. S. Patent No. 5,107,526 (April 21, 1992).
139. B. W. Loo, S. Williams, S. Meizel, S. S. Rothman, *J. Microsc.* **166**, RP5 (1992).
140. G. R. Morrison, *SPIE Volume 1741 Soft X-ray Microscopy*, (SPIE, Bellingham, Washington, 1992), p. 186.
141. G. R. Morrison, M. T. Browne, *Rev. Sci. Instrum.* **63**, 611 (1992).
142. R. E. Burge, C. J. Buckley, G. F. Foster, A. Miller, T. Wess, *J. X-ray Sci. Technol.* **3**, 311 (1992).
143. P. Guttman, *et al.*, in *SPIE Volume 1741 Soft X-ray Microscopy*, (SPIE, Bellingham, Washington, 1992), p. 52.
144. M. Hayashida, *et al.*, U. S. Patent No. 5,204,887 (April 20, 1993).
145. J. Stohr, *et al.*, *Science* **259**, 658 (1993).
146. S. Williams, *et al.*, *J. Microsc.* **170**, 155 (1993).
147. B. La Fontaine, *et al.*, *Appl. Phys. Lett.* **66**, 282 (1995).
148. A. C. Thompson, *et al.*, *Nuc. Inst. Meth. Phys. Res.* **A222**, 319 (1984).
149. U. Bonse, *et al.*, *Nuc. Inst. Meth. Phys. Res.* **A246**, 644 (1986).
150. P. Spanne, M. L. Rivers, *Nuc. Inst. Meth. Phys. Res.* **B24/25**, 1063 (1987).
151. J. H. Kinney, *et al.*, *Rev. Sci. Instrum.* **59**, 196 (1988).
152. K. Engelke, M. Lohmann, W. R. Dix, W. Graeff, *Rev. Sci. Instrum.* **60**, 2486 (1989).
153. J. H. Dunsmuir, H. W. Deckman, B. P. Flannery, K. L. D'Amico, S. R. Ferguson, in *Industrial Computerized Tomography*, (ASNT, Columbus, Ohio, 1989), p. 135.
154. W. Graeff, K. Engelke, in *Handbook on Synchrotron Radiation Volume 4*, S. Ebashi, *et al.*, Eds., (North-Holland, Amsterdam, 1991), p. 361.
155. J. H. Kinney, M. C. Nichols, *Annu. Rev. Mater. Sci.* **22**, 121 (1992).
156. J. V. Smith, in *X-ray Optics and Microanalysis 1992*, B.P. Kenway, *et al.*, Eds., (Institute of Physics, Bristol, 1992), p. 605.
157. M. D. Silver, in *SPIE Volume 2516 X-ray Microbeam Technology and Applications*, (SPIE, Bellingham, Washington, 1995).
158. T. Takeda, *et al.*, *Rev. Sci. Instrum.* **66**, 1471 (1995).

159. T. Takeda, *et al.*, in *SPIE Volume 2708 Physics of Medical Imaging*, (SPIE, Bellingham, Washington, 1996), p. 685.
160. A. Momose, T. Takeda, Y. Itai, K. Hirano, in *SPIE Volume 2708 Physics of Medical Imaging*, (SPIE, Bellingham, Washington, 1996), p. 674.
161. M. Pateyron, *et al.*, in *SPIE Volume 2708 Physics of Medical Imaging*, (SPIE, Bellingham, Washington, 1996), p. 417.
162. A. Momose, T. Takeda, Y. Itai, K. Hirano, *Nature Medicine* **2**, 473 (1996).
163. H. D. Bartunik, R. Fourme, C. Phillips, in *Uses of Synchrotron Radiation in Biology*, H. B. Stuhmann, Ed., (Academic, London, 1982), p. 145.
164. H. D. Bartunik, in *Handbook on Synchrotron Radiation Volume 4*, S. Ebashi, M. Koch, E. Rubenstein, Eds., (North-Holland, Amsterdam, 1991), p. 147.
165. M. G. Strauss, I. Naday, I. S. Sherman, *IEEE Trans. Nuc. Sci.* **NS-34**, 389 (1987).
166. M. G. Strauss, *et al.*, in *SPIE Volume 1447 Charge-Coupled Devices and Solid State Optical Sensors II*, (SPIE, Bellingham, Washington, 1991), p. 12.
167. I. Naday, M. G. Strauss, I. S. Sherman, M. R. Krammer, E. M. Westbrook, *Opt. Eng.* **26**, 788 (1987).
168. D. Cline, A. Garren, J. Kolonko, in *Nuclear Science Symposium and Medical Imaging Conference*, (IEEE, New York, 1993), p. 1799.
169. R. Fourme, in *Biomedical Applications of Synchrotron Radiation*, E. Burattini, Ed., (IOS Press, Amsterdam, 1996), p. 77.
170. R. Fourme, in *Biomedical Applications of Synchrotron Radiation*, E. Burattini, Ed., (IOS Press, Amsterdam, 1996), p. 209.
171. W. A. Eaton, E. R. Henry, J. Hofrichter, *Science* **274**, 1631 (1997).
172. J. Bordas, in *Uses of Synchrotron Radiation in Biology*, H. B. Stuhmann, Ed., (Academic, London, 1982), p. 107.
173. J. C. Solem, G. C. Baldwin, *Science* **218**, 1172 (1982).
174. J. C. Solem, G. F. Chapline, *Opt. Eng.* **23**, 193 (1984).
175. C. Jacobsen, M. Howells, J. Kirz, S. Rothman, *J. Opt. Soc. Am.* **A7**, 1847 (1990).
176. I. McNulty, *et al.*, *Science* **256**, 1009 (1992).
177. I. McNulty, *et al.*, in *SPIE Volume 1741 Soft X-ray Microscopy*, (SPIE, Bellingham, Washington, 1992), p. 78.
178. K. Boyer, J. C. Solem, J. W. Longworth, A. B. Borisov, C. K. Rhodes, *Nature Medicine* **2**, 939 (1996).
179. H. D. Zeman, *et al.*, *IEEE Trans. Nuc. Sci.* **NS-29**, 442 (1982).
180. E. B. Hughes, *et al.*, *Nuc. Inst. Meth.* **208**, 665 (1983).
181. E. B. Hughes, *et al.*, *Acta Radiol.* **S365**, 43 (1983).
182. E. B. Hughes, *et al.*, *Nuc. Inst. Meth. Phys. Res.* **B10/11**, 323 (1985).
183. E. B. Hughes, *et al.*, *Nuc. Inst. Meth. Phys. Res.* **A246**, 719 (1986).
184. J. N. Otis, *et al.*, *IEEE Trans. Nuc. Sci.* **NS-31**, 581 (1984).
185. A. Akisada, *et al.*, *Nuc. Inst. Meth. Phys. Res.* **A246**, 713 (1986).
186. W. R. Dix, *et al.*, *Nuc. Inst. Meth. Phys. Res.* **A246**, 702 (1986).
187. E. Rubenstein, *et al.*, *Proc. Natl. Acad. Sci. USA* **83**, 9724 (1986).
188. E. Rubenstein, *Ann. Rev. Biophys. Biophys. Chem.* **16**, 161 (1987).
189. R. K. Smith, E. M. Westbrook, *Nuc. Inst. Meth. Phys. Res.* **A266**, 260 (1988).
190. A. C. Thompson, *et al.*, *Nuc. Inst. Meth. Phys. Res.* **A266**, 252 (1988).
191. A. C. Thompson, *et al.*, *Rev. Sci. Instrum.* **60**, 1674 (1989).
192. S. A. Audet, *Rev. Sci. Instrum.* **60**, p. 2276 (1989).
193. K. Nishimura, *et al.*, *Rev. Sci. Instrum.* **60**, p. 2260 (1989).
194. K. Ueda, *et al.*, *Rev. Sci. Instrum.* **60**, p. 2272 (1989).
195. J. C. Giacomini, H. J. Gordon, in *Handbook on Synchrotron Radiation Volume 4*, S. Ebashi, M. Koch, E. Rubenstein, Eds., (North-Holland, Amsterdam, 1991), p. 349.
196. K. Hyodo, K. Nishimura, M. Ando, in *Handbook on Synchrotron Radiation Volume 4*, S. Ebashi, M. Koch, E. Rubenstein, Eds., (North-Holland, Amsterdam, 1991), p. 55.
197. T. Takeda, *et al.*, *Med. Biol. Eng. Comput.* **32**, 462 (1994).
198. H. Mori, *et al.*, *Circulation* **89**, 863 (1994).

199. H. Mori, *et al.*, *Circ. Res.* **76**, 1088 (1995).
200. H. Mori, *et al.*, *Radiology* **201**, 173 (1996).
201. F. E. Carroll, *et al.*, *Invest. Radiol.* **29**, 266 (1994).
202. R. Feder, D. Sayre, E. Spiller, J. Topalian, *J. Appl. Phys.* **47**, 1192 (1976).
203. R. Feder, *et al.*, *Science* **197**, 259 (1977).
204. D. Sayre, J. Kirz, R. Feder, D. M. Kim, E. Spiller, *Ultramicroscopy* **2**, 337 (1977).
205. D. Sayre, R. Feder, D. M. Kim, E. Spiller, *Science* **196**, 1330 (1977).
206. D. Sayre, J. Kirz, R. Feder, D. M. Kim, E. Spiller, *Ann. New York Acad. Sci.* **306**, 286 (1978).
207. M. R. Howells, J. Kirz, D. Sayre, *Scientific American*, (February, 1991), p. 88.
208. M. Hatzakis, *J. Electrochem. Soc.* **116**, 1033 (1969).
209. D. L. Spears, H. I. Smith, *Electronic Letters* **8**, 102 (1972).
210. R. Feder, E. Spiller, J. Topalian, *Polymer Engineering and Science* **17**, 385 (1977).
211. R. Feder, *et al.*, in *X-ray Microscopy*, G. Schmahl, D. Rudolph, Eds., (Springer, Berlin, 1984), p. 279.
212. R. Feder, V. Mayne-Banton, in *Examining the Submicron World*, R. Feder, J. W. McGowan, D. M. Shinozaki, Eds., (Plenum, New York, 1986), p. 277.
213. I. Haller, R. Feder, M. Hatzakis, E. Spiller, *J. Electrochem. Soc.* **126**, 154 (1979).
214. W. Meyer-Ilse, in *SPIE Volume 1140 X-ray Instrumentation in Medicine and Biology*, (SPIE, Bellingham, Washington, 1989), p. 226.
215. G. D. Kubiak, R. Q. Hwang, M. T. Schulberg, D. A. Tichenor, K. Early, *Applied Optics* **32**, 7036 (1993).
216. K. Early, *et al.*, *Applied Optics* **32**, 7044 (1993).
217. T. Tomie, *et al.*, *Science* **252**, 691 (1991).
218. Y. I. Borodin, *et al.*, *Nuc. Instrum. Meth. Phys. Res.* **A246**, 649 (1986).
219. F. Cinotti, *et al.*, in *X-ray Microscopy: Instrumentation and Biological Applications*, P. C. Cheng and G.J. Jan, Eds., (Springer, Berlin, 1987), p. 311.
220. H. Rarback, *et al.*, *Rev. Sci. Instrum.* **59**, 52 (1988).
221. C. J. Buckley, H. Rarback, in *Modern Microscopies: Techniques and Applications* P. J. Duke, A. G. Michette, Eds., (Plenum, New York, 1990), p. 69.
222. D. Morris, *et al.*, *Scanning* **13**, 7 (1991).
223. W. Meyer-Ilse, M. Moronne, C. Magowan, P. Selvin, *Scanning* **15**, Suppl.III, 35 (1993).
224. G. Schmahl, D. Rudolph, P. Guttmann, O. Christ, in *X-ray Microscopy*, G. Schmahl, D. Rudolph, Eds., (Springer, Berlin, 1984), p. 63.
225. V. Bogli, *et al.*, *Opt. Eng.* **27**, 143 (1988).
226. B. Lai, *et al.*, *Appl. Phys. Lett.* **61**, 1877 (1992).
227. A. A. Krasnoperova, *et al.*, *J. Vac. Sci. Technol.* **B11**, 2588 (1993).
228. E. Spiller, in *X-ray Microscopy: Instrumentation and Biological Applications*, P. C. Cheng and G.J. Jan, Eds., (Springer, Berlin, 1987), p. 224.
229. M. Howells, *et al.*, *Science* **238**, 514 (1987).
230. D. Joyeux, F. Polack, R. Mercier, in *SPIE Volume 1140 X-ray Instrumentation in Medicine and Biology*, (SPIE, Bellingham, Washington, 1989), p. 399.
231. P. Spanne, *Phys. Med. Biol.* **34**, 679 (1989).
232. J. C. Elliott, D. K. Bowen, S. D. Dover, S. T. Davies, *Biological Trace Element Research* **13**, 219 (1987).
233. W. Graeff, K. Engelke, *Microradiography and Microtomography*, HASYLAB/DESY Report No. F41-9004, July, 1990, p. 1.
234. F. A. Dilmanian, *et al.*, in *IEEE Nuclear Science Symposium and Medical Imaging Conference*, (IEEE, New York, 1991), p. 1831.
235. K. W. Jones, *et al.*, in *X-ray Microscopy III*, A. G. Michette, G. R. Morrison, C. J. Buckley, Eds., (Springer, Berlin, 1992), p. 431.
236. K. Engelke, W. Graeff, L. Meiss, M. Hahn, G. Delling, *Invest. Radiol.* **28**, 341 (1993).
237. W. S. Haddad, *et al.*, *Science* **266**, 1213 (1994).
238. P. Cloetens, R. Barrett, J. Baruchel, J. P. Guigay, M. Schlenker, *J. Phys. D: Appl. Phys.* **29**, 133 (1996).

239. A. Momose, J. Fukuda, *Med. Phys.* **22**, 375 (1996).
240. E. N. Dementiev, *et al.*, *Rev. Sci. Instrum.* **60**, 2264 (1989).
241. R. A. McCorkle, *Ann. New York Acad. Sci.* **342**, 53 (1980).
242. S. Bowyer, *Applied Optics* **32**, 6930 (1993).
243. A. Schulz, R. Burhenn, F. B. Rosmej, H. J. Kunze, *J. Phys. D: Appl. Phys.* **22**, 659 (1989).
244. J. Goldstein, *Science* **277**, 306 (1997).
245. J. H. Dave, *et al.*, *J. Opt. Soc. Am.* **B4**, 635 (1987).
246. M. Sato, *Rev. Sci. Instrum.* **58**, 481 (1987).
247. C. Tillman, A. Persson, C.-G. Wahlstrom, S. Svanberg, K. Herrlin, *Appl. Phys.* **B61**, 333 (1995).
248. K. Herrlin, *et al.*, *Radiology* **189**, 65 (1993).
249. D. Strickland, G. Mourou, *Opt. Commun.* **56**, 219 (1985).
250. M. D. Perry, A. Szoke, O. L. Landen, E. M. Campbell, *Phys. Rev. Lett.* **60**, 1270 (1988).
251. M. D. Perry, G. Mourou, *Science* **264**, 917 (1994).
252. M. M. Murnane, H. C. Kapteyn, R. W. Falcone, *Phys. Rev. Lett.* **62**, 155 (1989).
253. M. M. Murnane, H. C. Kapteyn, M. D. Rosen, R. W. Falcone, *Science* **251**, 531 (1991).
254. J. C. Kieffer, *et al.*, *Phys. Rev. Lett.* **62**, 760 (1989).
255. J. C. Kieffer, *ibid.*, **68**, 480 (1992).
256. J. C. Kieffer, *et al.*, *Phys. Fluids* **B5**, 2676 (1993).
257. J. C. Kieffer, *et al.*, *Applied Optics* **32**, 4247 (1993).
258. S. Augst, D. Strickland, D. D. Meyerhofer, S. L. Chin, J. H. Eberly, *Phys. Rev. Lett.* **63**, 2212 (1989).
259. M. Pessot, J. Squier, G. Mourou, D. J. Harter, *Opt. Lett.* **14**, 797 (1989).
260. H. C. Kapteyn, M. M. Murnane, A. Szoke, A. Hawryluk, R. W. Falcone, in *Ultrafast Phenomena VII*, C. P. Harris, E. P. Ippen, G. A. Mourou, A. H. Zewail, Eds., (Springer, Berlin, 1990), p. 122.
261. M. Chaker, *et al.*, *Phys. Fluids* **B3**, 167 (1991).
262. J. Zhou, C.-P. Huang, C. Shi, M. M. Murnane, H. C. Kapteyn, *Opt. Lett.* **19**, 126 (1994).
263. J. Zhou, C.-P. Huang, M. M. Murnane, H. C. Kapteyn, *Opt. Lett.* **20**, 64 (1995).
264. I. P. Christov, H. C. Kapteyn, M. M. Murnane, C.-P. Huang, J. Zhou, *Opt. Lett.* **20**, 309 (1995).
265. J. Bailey, Y. Ettinger, A. Fisher, R. Feder, *Appl. Phys. Lett.* **40**, 33 (1982).
266. R. Feder, J. S. Pearlman, J. C. Riordan, J. L. Costa, *J. Microsc.* **135**, 347 (1984).
267. R. B. Spielman, *et al.*, *J. Appl. Phys.* **57**, 830 (1985).
268. R. E. Stewart, D. D. Dietrich, R. J. Fortner, R. Dukart, *J. Opt. Soc. Am.* **B4**, 396 (1987).
269. B. Niemann, *et al.*, *Optik* **84**, 35 (1990).
270. W. Neff, R. Holz, R. Lebert, F. Richter, U. S. Patent No. 5,023,897, June 11, 1991.
271. D. Rudolph, B. Niemann, G. Schmahl, J. Thieme, in *X-ray Microscopy II*, D. Sayre, M. Howells, J. Kirz, H. Rarback, Eds., (Springer, Berlin, 1988), p. 216.
272. W. Neff, J. Eberle, R. Holz, R. Richter, R. Lebert, in *X-ray Microscopy II*, D. Sayre, M. Howells, J. Kirz, H. Rarback, Eds., (Springer, Berlin, 1988), p. 22.
273. D. Rothweiler, W. Neff, R. Lebert, F. Richter, M. Diehl, in *X-ray Optics and Microanalysis 1992*, B.P. Kenway, *et al.*, Eds., (Institute of Physics, Bristol, 1992), p. 479.
274. J. L. Krause, K. J. Schafer, K. C. Kulander, *Phys. Rev. Lett.* **68**, 3535 (1992).
275. A. G. Michette, *et al.*, *J. Phys. D: Appl. Phys.* **19**, 363 (1986).
276. G. Zeng, *et al.*, *J. Appl. Phys.* **67**, 3597 (1990).
277. G. Zeng, *et al.*, *J. Appl. Phys.* **69**, 7460 (1991).
278. C. J. Joshi, P. B. Corkum, *Physics Today*, (January, 1995), p. 36.
279. P. T. Rumsby, *J. Microsc.* **138**, 245 (1985).
280. R. W. Eason *et al.*, *Optica Acta* **33**, 501 (1986).
281. A. D. Stead, T. W. Ford, *Annals of Botany* **64**, 713 (1989).

282. R. E. Burge, *et al.*, in *X-ray Optics and Microanalysis 1992*, B.P. Kenway, *et al.*, Eds., (Institute of Physics, Bristol, 1992), p. 487.
283. R. E. Burge, M. T. Browne, P. Charalambous, G. Slark, P. Smith, in *SPIE Volume 1741 Soft X-ray Microscopy*, (SPIE, Bellingham, Washington, 1992), p. 170.
284. H. He, *et al.*, *Rev. Sci. Instrum.* **64**, 26 (1993).
285. R. D. Frankel, J. M. Forsyth, *Science* **204**, 622 (1979).
286. N. M. Ceglio, *Ann. New York Acad. Sci.* **342**, 65 (1978).
287. F. Ze, *et al.*, *J. Appl. Phys.* **66**, 1935 (1989).
288. P. Maine, G. Mourou, *Opt. Lett.* **13**, 467 (1988).
289. Y. Kinjo, *et al.*, *J. Microsc.* **176**, 63 (1994).
290. N. Sarakura, Y. Ishida, H. Nakano, Y. Yamamoto, *Appl. Phys. Lett.* **56**, 814 (1990).
291. J. D. Kmetz, J. J. Macklin, J. F. Young, *Opt. Lett.* **16**, 1001 (1991).
292. D. E. Spence, P. N. Kean, W. Sibbet, *Opt. Lett.* **16**, 42 (1991).
293. J. L. A. Chilla, O. E. Martinez, *J. Opt. Soc. Am.* **B10**, 638 (1993).
294. C. P. J. Barty, C. L. Gordon, B. E. Lemoff, *Opt. Lett.* **19**, 1442 (1994).
295. P. D. Gupta, P. A. Naik, H. C. Pant, *J. Appl. Phys.* **56**, 1371 (1984).
296. L. A. Gizzi, *et al.*, *Phys. Rev. Lett.* **76**, 2278 (1996).
297. D. G. Stearns, O. L. Landen, E. M. Cambell, J. H. Scofield, *Phys. Rev.* **A37**, 1684 (1988).
298. K. A. Tanaka, *et al.*, *J. Appl. Phys.* **63**, 1787 (1988).
299. J. A. Cobble, *et al.*, *J. Appl. Phys.* **69**, 3369 (1991).
300. R. Bobkowski, J. N. Broughton, R. Fedosejevs, R. J. Willis, M. R. Cervenak, *J. Appl. Phys.* **76**, 5047 (1994).
301. A. McPherson, B. D. Thompson, A. B. Borisov, K. Boyer, C. K. Rhodes, *Nature* **370**, 631 (1994).
302. A. B. Borisov, A. McPherson, K. Boyer, C. K. Rhodes, in *X-ray Lasers*, D. C. Eder, D. L. Matthews, Eds., (American Institute of Physics, New York, 1994), p. 134.
303. A. B. Borisov, A. McPherson, B. D. Thompson, K. Boyer, C. K. Rhodes, *J. Phys. B: At. Mol. Opt. Phys.* **B28**, 2143 (1995).
304. R. J. Rosser, *et al.*, *Applied Optics* **26**, 4313 (1987).
305. D. A. Tichenor, *et al.*, *Opt. Lett.* **16**, 1557 (1991).
306. F. Bijkerk, in *X-ray Optics and Microanalysis 1992*, B.P. Kenway, *et al.*, Eds., (Institute of Physics, Bristol, 1992), p. 471.
307. F. Bijkerk, E. Louis, G. E. van Dorssen, A. P. Shevelko, A. A. Vasilyev, *Applied Optics* **33**, 82 (1994).
308. E. Louis, *et al.*, *Microelectronic Engineering* **21**, 67 (1993).
309. R. L. Kauffman, D. W. Phillion, R. C. Spitzer, *Applied Optics* **32**, 6897 (1993).
310. M. Richardson, *et al.*, *Applied Optics* **32**, 6901 (1993).
311. L. A. Hackel, R. J. Beach, C. B. Dane, L. E. Zapata, *Applied Optics* **32**, 6914 (1993).
312. S. J. Haney, K. W. Berger, G. D. Kubiak, P. D. Rockett, J. Hunter, *Applied Optics* **32**, 6934 (1993).
313. G. E. Sommargren, L. G. Seppala, *Applied Optics* **32**, 6938 (1993).
314. C. Cerjan, *Applied Optics* **32**, 6911 (1993).
315. L. Malmqvist, L. Rymell, H. M. Hertz, *Appl. Phys. Lett.* **68**, 2627 (1996).
316. H. Nakano, T. Nishikawa, N. Uesugi, *Appl. Phys. Lett.* **70**, 16 (1997).
317. R. Feder, *et al.*, *Science* **227**, 63 (1985).
318. R. J. Rosser, R. Feder, A. Ng, P. Celliers, *J. Microsc.* **140**, RP1 (1985).
319. A. G. Michette, *et al.*, *Rev. Sci. Instrum.* **64**, 1478 (1993).
320. A. G. Michette, R. Fedosejevs, S. J. Pfauntsch, R. Bobkowski, *Measurement Science and Technology* **5**, 555 (1994).
321. T. Tomie, *et al.*, in *SPIE Volume 1741 Soft X-ray Microscopy*, (SPIE, Bellingham, Washington, 1992), p. 118.
322. M. Richardson, *et al.*, in *SPIE Volume 1741 Soft X-ray Microscopy*, (SPIE, Bellingham, Washington, 1992), p. 133.
323. J. Fletcher, R. Cotton, C. Webb, in *SPIE Volume 1741 Soft X-ray Microscopy*, (SPIE, Bellingham, Washington, 1992), p. 142.

324. R. A. Cotton, M. D. Dooley, J. H. Fletcher, A. D. Stead, T. W. Ford, in *SPIE Volume 1741 Soft X-ray Microscopy*, (SPIE, Bellingham, Washington, 1992), p. 204.
325. H. K. Pew, G. L. Stradling, in *X-ray Microscopy III*, A. G. Michette, G. R. Morrison, C. J. Buckley, Eds., (Springer, Berlin, 1992), p. 206.
326. A. D. Stead, R. A. Cotton, A. M. Page, M. D. Dooley, T. W. Ford, in *SPIE Volume 1741 Soft X-ray Microscopy*, (SPIE, Bellingham, Washington, 1992), p. 351.
327. K. Shinohara, *et al.*, in *SPIE Volume 1741 Soft X-ray Microscopy*, (SPIE, Bellingham, Washington, 1992), p. 386.
328. H. Aritome, *et al.*, in *SPIE Volume 1741 Soft X-ray Microscopy*, (SPIE, Bellingham, Washington, 1992), p. 129.
329. Y. Horikawa, K. Nagai, S. Mochimaru, Y. Iketaki, *J. Microsc.* **172**, 189 (1993).
330. H. Kondo, T. Tomie, *J. Appl. Phys.* **75**, 3798 (1994).
331. I. C. E. Turcu, *et al.*, *J. Appl. Phys.* **73**, 8081 (1993).
332. J. Rosser, *et al.*, *J. Microsc.* **138**, 311 (1985).
333. S. P. Vernon, D. G. Stearns, R. S. Rosen, *Opt. Lett.* **18**, 672 (1993).
334. L. Rymell, H. M. Hertz, *Opt. Commun.* **103**, 105 (1993).
335. K.-D. Song, D. R. Alexander, *J. Appl. Phys.* **76**, 3302 (1994).
336. B. J. Panessa, R. A. McCorkle, P. Hoffman, J. B. Warren, G. Coleman, *Ultramicroscopy* **6**, 139 (1981).
337. B. J. Panessa-Warren, in *X-ray Microscopy*, G. Schmahl, D. Rudolf, Eds., (Springer, Berlin, 1984), p. 268.
338. J. A. Trail, R. L. Byer, J. B. Kortright, in *X-ray Microscopy II*, D. Sayre, M. Howells, J. Kirz, H. Rarback, Eds., (Springer, Berlin, 1988), p. 310.
339. J. A. Trail, R. L. Byer, *Opt. Lett.* **14**, 539 (1989).
340. I. A. Artyukov, A. I. Fedorenko, V. V. Kondratenko, S. A. Yulin, A. V. Vinogradov, *Opt. Commun.* **102**, 401 (1993).
341. M. Yasugaki, Y. Horikawa, U. S. Patent No. 5,131,023, July 14, 1992.
342. J. C. Solem, *J. Opt. Soc. Am.* **B3**, 1551 (1986).
343. E. Spiller, R. Feder, in *X-ray Optics Applications to Solids*, H. J. Queisser, Ed., (Springer, Berlin, 1977), p. 35.
344. K. Shinohara, *et al.*, *Photochemistry and Photobiology* **44**, 401 (1986).
345. K. Shinohara, Y. Kinjo, M. C. Richardson, *et al.*, in *SPIE Volume 1741 Soft X-ray Microscopy*, (SPIE, Bellingham, Washington, 1992), p. 386.
346. K. Shinohara, A. Ito, *J. Microsc.* **161**, 463 (1991).
347. K. Shinohara, *et al.*, in *X-ray Microscopy III*, A. G. Michette, G. R. Morrison, C. J. Buckley, Eds., (Springer, Berlin, 1992), p. 347.
348. A. Ito, K. Shinohara, *Cell Structure and Function* **17**, 209 (1992).
349. A. Ito, K. Shinohara, H. Nakano, T. Matsumura, K. Kinoshita, *J. Microsc.* **181**, 54 (1996).
350. T. W. Ford, A. D. Stead, C. P. B. Hills, R. J. Rosser, N. Rizvi, *J. X-ray Sci. Technol.* **1**, 207 (1989).
351. D. C. O'Shea, W. R. Callen, W. T. Rhodes. *Introduction to Lasers and their Applications*. (Addison-Wesley, Reading, Massachusetts, 1977).
352. R. C. Elton. *X-ray Lasers*. (Academic, Boston, 1990).
353. D. L. Matthews, *et al.*, *Phys. Rev. Lett.* **54**, 110 (1985).
354. S. Suckewer, C. H. Skinner, H. Milchberg, C. Keane, D. Voorhees, *Phys. Rev. Lett.* **55**, 1753 (1985).
355. M. Pessot, P. Maine, G. Mourou, *Opt. Commun.* **62**, 419 (1987).
356. J. J. Rocca, *et al.*, in *X-ray Lasers*, D. C. Eder, D. L. Matthews, Eds., (American Institute of Physics, New York, 1994), p. 359.
357. G. P. Collins, *Physics Today*, (October, 1994), p. 19.
358. C. H. Skinner, *Phys. Fluids* **B3**, 2420 (1991).
359. Y. Nagata, *et al.*, *Phys. Rev. Lett.* **71**, 3774 (1993).
360. L. I. Gudzenko, L. A. Shelepin, *Sov. Phys.-Dok.* **10**, 147 (1965).
361. L. I. Gudzenko, L. A. Shelepin, S. I. Yakovlenko, *Sov. Phys.-Usp.* **17**, 848 (1975).
362. J. Peyraud, N. Peyraud, *J. Appl. Phys.* **43**, 2993 (1972).

363. J. C. Weisheit, *J. Phys. B: Atom. Molec. Phys.* **8**, 1556 (1975).
364. J. C. Weisheit, C. B. Tarter, J. H. Scofield, L. M. Richards, *J. Quant. Spectrosc. Radiat. Transfer* **16**, 659 (1976).
365. J. M. Green, W. T. Silfvast, *Appl. Phys. Lett.* **28**, 253 (1976).
366. W. W. Jones, A. W. Ali, *J. Appl. Phys.* **48**, 3118 (1977).
367. W. W. Jones, A. W. Ali, *J. Phys. B: Atom. Molec. Phys.* **11**, L87 (1978).
368. D. Matthews, *et al.*, *J. Opt. Soc. Am.* **B4**, 575 (1987).
369. A. K. Davé, G. J. Pert, *J. Phys. B: Atom. Mol. Phys.* **18**, 1027 (1985).
370. W. T. Silfvast, O. R. Wood, *J. Opt. Soc. Am.* **B4**, 609 (1987).
371. J. E. Trebes, *et al.*, *Science* **238**, 517 (1987).
372. C. H. Skinner, D. Kim, A. Wouters, D. Voorhees, S. Suckewer, in *X-ray Microscopy II*, D. Sayre, M. Howells, J. Kirz, H. Rarback, Eds., (Springer, Berlin, 1988), p. 36.
373. N. H. Burnett, P. B. Corkum, *J. Opt. Soc. Am.* **B6**, 1195 (1989).
374. N. H. Burnett, G. D. Enright, *IEEE J. Quant. Elect.* **26**, 1797 (1990).
375. D. C. Eder, *Phys. Fluids* **B2**, 3086 (1990).
376. D. C. Eder, D. L. Matthews, Eds. *X-ray Lasers*. (American Institute of Physics, New York, 1994).
377. P. Amendt, D. C. Eder, S. C. Wilks, *Phys. Rev. Lett.* **66**, 2589 (1991).
378. B. J. MacGowan, in *SPIE Volume 1741 Soft X-ray Microscopy*, (SPIE, Bellingham, Washington, 1992), p. 2.
379. L. B. Da Silva, *et al.*, *Science* **258**, 269 (1992).
380. L. B. Da Silva, *Opt. Lett.* **17**, 754 (1992).
381. L. B. Da Silva, in *SPIE Volume 1741 Soft X-ray Microscopy*, (SPIE, Bellingham, Washington, 1992), p. 154.
382. R. Balhorn, *et al.*, in *SPIE Volume 1741 Soft X-ray Microscopy*, (SPIE, Bellingham, Washington, 1992), p. 374.
383. D. I. Chiu, in *X-ray Optics and Microanalysis 1992*, B.P. Kenway, *et al.*, Eds., (Institute of Physics, Bristol, 1992), p. 511.
384. D. Attwood, *Physics Today*, (August, 1992), p. 24.
385. D. S. DiCicco, D. Kim, R. Rosser, S. Suckewer, *Opt. Lett.* **17**, 157 (1992).
386. R. Cauble, *et al.*, *Science* **273**, 1093 (1996).
387. S. Suckewer, C. H. Skinner, R. Rosser, U. S. Patent No. 5,177,774, January 5, 1993.
388. C. H. Skinner, *et al.*, *J. Microsc.* **159**, 51 (1990).
389. D. S. DiCicco, D. Kim, L. Polonsky, C. H. Skinner, S. Suckewer, in *SPIE Volume 1741 Soft X-ray Microscopy*, (SPIE, Bellingham, Washington, 1992), p. 160.
390. S.-S. Han, *et al.*, in *X-ray Lasers*, D. C. Eder, D. L. Matthews, Eds., (American Institute of Physics, New York, 1994), p. 235.
391. R. A. London, M. D. Rosen, J. E. Trebes, *Appl. Opt.* **28**, 3397 (1989).
392. M. H. Key, C. G. Smith, in *X-ray Lasers*, D. C. Eder, D. L. Matthews, Eds., (American Institute of Physics, New York, 1994), p. 423.
393. F. E. Carroll, *et al.*, *Invest. Radiol.* **25**, 465 (1990).
394. C. A. Brau, *Free Electron Lasers* (Academic Press, Cambridge, 1990).
395. C. Pellegrini, *et al.*, *Nuc. Instrum. Meth. Phys. Res.* **A331**, 223 (1993).
396. K. J. Weeks, V. N. Litvinenko, J. M. J. Madey, *Med. Phys.* **24**, 417 (1997).
397. P. Eisenberger, S. Suckewer, *Science* **274**, 201 (1996).
398. R. W. Schoenlein, *et al.*, *Science* **274**, 236 (1996).
399. D. A. Skoog, D. M. West. *Fundamentals of Analytical Chemistry 3rd Edition*. (Holt, Rinehart and Winston, New York, 1976).
400. F. H. Attix. *Introduction to Radiological Physics and Radiation Dosimetry*. (Wiley, New York, 1986).
401. J. D. Jackson. *Classical Electrodynamics 2nd Edition*. (Wiley, New York, 1975).
402. J. H. Hubbell, *et al.*, *J. Phys. Chem. Ref. Data* **4**, 471 (1975).
403. E. F. Plechaty, D. E. Cullen, R. J. Howerton, *Report UCRL-50400* (Lawrence Livermore National Laboratory, University of California, 1975).
404. C. Jacobsen, in *Biomedical Applications of Synchrotron Radiation*, E. Burattini, A. Balerna, Eds., (IOS Press, Amsterdam, 1996), p. 59.

405. B. L. Henke, E. M. Gullikson, J. C. Davis, *At. Data Nucl. Data Tables* **54**, 181 (1993).
406. O. Klein, Y. Nishina, *Zeitschrift Physik* **52**, 853 (1929).
407. R. E. Alvarez, A. Macovski, *Phys. Med. Biol.* **21**, 733 (1976).
408. H. K. Huang, C. K. Wong, F. L. Roder, in *IEEE International Workshop on Physics and Engineering in Medical Imaging*, (IEEE, New York, 1982), p. 122.
409. D. R. White, R. J. Martin, R. Darlison, *Br. J. Radiol.* **50**, 814 (1977).
410. D. R. White, M. Fitzgerald, *Health Physics* **33**, 73 (1977).
411. D. R. White, *Med. Phys.* **5**, 467 (1978).
412. W. J. Hamilton, *et al.*, in *Nuclear Science Symposium and Medical Imaging Conference*, (IEEE, New York, 1993), p. 232.
413. R. C. Schirato, R. M. Polichar, J. H. Reed, S. T. Smith, in *SPIE Volume 2009 X-ray Detector Physics and Applications II*, (SPIE, Bellingham, Washington, 1993), p. 48.
414. W. Zhao, *et al.*, in *SPIE Volume 2708 Physics of Medical Imaging*, (SPIE, Bellingham, Washington, 1996), p. 523.
415. D. L. Lee, L. K. Cheung, E. F. Palecki, L. S. Jeromin, in *SPIE Volume 2708 Physics of Medical Imaging*, (SPIE, Bellingham, Washington, 1996), p. 511.
416. D. M. Korn, A. R. Lubinsky, J. F. Owen, in *SPIE Volume 626 Medicine XIV/PACS IV*, (SPIE, Bellingham, Washington, 1986), p. 108.
417. A. Lubinsky, Owen, JF and Korn, DM, in *SPIE Volume 626 Medicine XIV/PACS IV*, (SPIE, Bellingham, Washington, 1986), p. 120.
418. J. Miyahara, K. Takahashi, Y. Amemiya, N. Kamiya, Y. Satow, *Nuc. Instrum. Meth. Phys. Res.* **A246**, 572 (1986).
419. B. R. Whiting, J. F. Owen, B. H. Rubin, *Nuc. Instrum. Meth. Phys. Res.* **A266**, 628 (1988).
420. Y. Amemiya, *et al.*, *Nuc. Instrum. Meth. Phys. Res.* **A266**, 645 (1988).
421. Y. Amemiya, S. Kishimoto, T. Matsushita, Y. Satow, M. Ando, *Rev. Sci. Instrum.* **60**, 1552 (1989).
422. C. E. Floyd, H. G. Chotas, J. T. Dobbins, C. E. Ravin, *Med. Phys.* **17**, 454 (1990).
423. R. H. Templer, *Nuc. Instrum. Meth. Phys. Res.* **A300**, 357 (1991).
424. F. K. Koschnick, J. M. Spaeth, R. S. Eachus, W. G. McDugle, R. H. D. Nuttall, *Phys. Rev. Lett.* **67**, 3571 (1991).
425. F. K. Koschnick, J. M. Spaeth, R. S. Eachus, *J. Phys.: Condensed Matter* **4**, 8919 (1992).
426. H. von Seggern, *Nuc. Instrum. Meth. Phys. Res.* **A322**, 467 (1992).
427. J. M. Spaeth, F. K. Koschnick, R. S. Eachus, W. G. McDugle, R. H. D. Nuttall, *Nucl. Tracks Radiat. Meas.* **21**, 73 (1993).
428. G. V. Semisotnov, *et al.*, *J. Molec. Biol.* **262**, 559 (1996).
429. L. E. Antonuk, *et al.*, *IEEE Trans. Med. Imaging* **13**, 482 (1994).
430. L. E. Antonuk, *et al.*, *Med. Phys.* **19**, 1455 (1992).
431. L. E. Antonuk, *et al.*, *Med. Phys.* **21**, 942 (1994).
432. J. H. Siewerdsen, *et al.*, *Med. Phys.* **24**, 71 (1997).
433. L. E. Antonuk, *et al.*, *Med. Phys.* **24**, 51 (1997).
434. S. M. Gruner, J. R. Milch, G. T. Reynolds, *Nuc. Instrum. Meth.* **195**, 287 (1982).
435. S. M. Gruner, *Rev. Sci. Instrum.* **60**, 1545 (1989).
436. A. R. Cowen, A. Workman, *Phys. Med. Biol.* **37**, 325 (1992).
437. V. G. M. Althof, *et al.*, *Med. Phys.* **23**, 1845 (1996).
438. J. M. Boone, T. Yu, J. A. Seibert, *Med. Phys.* **23**, 1955 (1996).
439. T. Yu, J. M. Boone, *Med. Phys.* **24**, 565 (1997).
440. S. Hejazi, D. P. Trauernicht, *Med. Phys.* **24**, 287 (1997).
441. P. F. Schmidt, D. V. McCaughan, R. A. Kushner, *Proc. IEEE* **62**, 1220 (1974).
442. V. A. J. van Lint, *Proc. IEEE* **62**, 1190 (1974).
443. J. Janesick, T. Elliott, F. Pool, *IEEE Trans. Nuc. Sci.* **NS-36**, 572 (1989).
444. G. W. Ludwig, J. D. Kingsley, *J. Electrochem. Soc.* **117**, 348 (1970).
445. G. W. Ludwig, J. S. Prener, *IEEE Trans. Nuc. Sci.* **NS-19**, 3 (1972).
446. R. K. Swank, *J. Appl. Phys.* **44**, 4199 (1973).
447. J. H. Chappell, S. S. Murray, *Nuc. Instrum. Meth. Phys. Res.* **221**, 159 (1984).

448. D. M. de Leeuw, T. Kovats, S. Herko, *J. Electrochem. Soc.* **134**, 491 (1987).
449. E. Sluzky, K. Hesse, *J. Electrochem. Soc.* **135**, 2893 (1988).
450. E. Sluzky, K. Hesse, *J. Electrochem. Soc.* **136**, 2724 (1989).
451. D. J. Mickish, J. Beutel, in *SPIE Volume 1231 Image Formation*, (SPIE, Bellingham, Washington, 1990), p. 327.
452. G. Blasse, *IEEE Trans. Nuc. Sci.* **NS-38**, 30 (1991).
453. G. E. Giakoumakis, *et al.*, *Med. Phys.* **20**, 79 (1993).
454. S. M. Gruner, S. L. Barna, M. E. Wall, M. W. Tate, E. F. Eikenberry, in *SPIE Volume 2009 X-ray Detector Physics and Applications II*, (SPIE, Bellingham, Washington, 1993), p. 98.
455. D. Cavouras, I. Kandarakis, G. S. Panayiotakis, E. K. Evangelou, C. D. Nomicos, *Med. Phys.* **23**, 1965 (1996).
456. K. Oba, M. Ito, M. Yamaguchi, M. Tanaka, *Adv. Elect. Electron. Phys.* **74**, 247 (1988).
457. T. S. Curry, J. E. Dowdey, R. C. Murry. *Christensen's Introduction to the Physics of Diagnostic Radiology*. (Lea and Febiger, Philadelphia, 1984).
458. W. C. Rontgen, *Nature* **53**, 274 (1896).
459. W. K. Rontgen, *CA A Cancer Journal for Clinicians* **22**, 153 (1972).
460. O. Glasser. *Dr. W.C. Rontgen*. (Charles C Thomas, Springfield, Illinois, 1945).
461. O. Glasser. *Wilhelm Conrad Rontgen and the Early History of the Roentgen Rays*. (Charles C Thomas, Springfield, Illinois, 1934).
462. M. Yaffe, A. Fenster, H. E. Johns, *J. Comp. Assist. Tomog.* **1**, 419 (1977).
463. A. Fenster, *J. Comp. Assist. Tomog.* **2**, 243 (1978).
464. H. N. Cardinal, A. Fenster, *Med. Phys.* **15**, 167 (1988).
465. D. A. Cusano, C. D. Greskovich, F. A. DiBianca, U. S. Patent No. 4,421,671, December 20, 1983.
466. E. Thomson, *Boston Med. Surg.* **135**, 610 (1896).
467. L. S. Taylor. *Radiation Protection Standards*. (CRC Press, Cleveland, 1971).
468. ICRU Report No. 30. *Quantitative Concepts and Dosimetry in Radiobiology*. (International Commission on Radiation Units and Measurements, Washington, 1979).
469. ICRU Report No. 33. *Radiation Quantities and Units*. (ICRU, Washington, 1980).
470. ICRU Report No. 51. *Quantities and Units in Radiation Protection Dosimetry*. (ICRU, Washington, 1993).
471. ICRU Report No. 10. *Radiation Quantities and Units*. (ICRU, Washington, 1962).
472. NBS. *National Bureau of Standards Handbook 85*. (U.S. Government Printing Office, Washington, 1964).
473. I. A. Cunningham, A. Fenster, *Med. Phys.* **11**, 303 (1984).
474. NCRP. *NCRP Report Number 91*. (National Council on Radiation Protection, Washington, 1987).